

## Durham E-Theses

---

# *SHIMM: A Low-Cost Portable Seeing Monitor for Astronomical Observing Sites*

SAAVIDRA PERERA

### How to cite:

---

PERERA, SAAVIDRA (2018) SHIMM: A Low-Cost Portable Seeing Monitor for Astronomical Observing Sites. Doctoral thesis, Durham University.

### Use policy

---

The full-text may be used and/or reproduced, and given to third parties in any format or medium, without prior permission or charge, for personal research or study, educational, or not-for-profit purposes provided that:

- a full bibliographic reference is made to the original source
- a <https://etheses.durham.ac.uk/id/eprint/12640/> is made to the metadata record in Durham E-Theses
- the full-text is not changed in any way

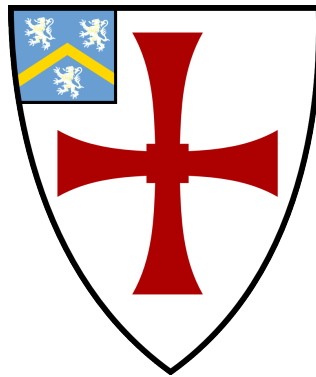
The full-text must not be sold in any format or medium without the formal permission of the copyright holders.

Please consult the [full Durham E-Theses policy](#) for further details.

# SHIMM: A Low-Cost Portable Seeing Monitor for Astronomical Observing Sites

Saavidra Perera

A thesis presented for the degree of  
Doctor of Philosophy



Centre for Advanced Instrumentation  
The University of Durham  
United Kingdom  
June 2018

*For my parents and sister.*

# SHIMM: A Low-Cost Portable Seeing Monitor for Astronomical Observing Sites

Saavidra Perera

## Abstract

Characterisation of atmospheric seeing and optical turbulence is crucial for the design and operation of modern ground-based optical telescopes. With a new generation of extremely large telescopes being proposed and constructed, new obstacles will be faced with regards to imaging through our turbulent atmosphere. The Differential Image Motion Monitor (DIMM) has been a commonly employed seeing monitor at astronomical observing sites across the world. For decades it has inexpensively provided sites with measurements of the Fried parameter ( $r_0$ ). In this thesis a variation on the current DIMM design will be presented. The Shack-Hartmann Image Motion Monitor (SHIMM) employs a low order Shack-Hartman (SH) lenslet array instead of the two hole aperture mask utilised by the DIMM. The SHIMM is a low-cost, portable instrument, comprised of off-the-shelf components, making it easily duplicated and therefore ideal for comparisons of atmospheric conditions at large observing sites.

In this thesis the four key advantages of the SHIMM will be addressed. By utilising a SH lenslet array the SHIMM can employ methods for estimating the value of  $r_0$ , independent of noise; estimate the atmospheric coherence time; correct for the effect of scintillation on the measurement of  $r_0$ ; and produce a low-resolution fixed three layer turbulence profile. On-sky results of each feature will be presented in this thesis.

Supervisors: Dr R. W. Wilson and Prof. R. Myers

---

# Acknowledgements

First and foremost, I would like to thank Richard Wilson who has guided and advised me throughout my PhD. I feel very grateful to have had Richard as my supervisor and without him this PhD would not have been possible. I would like to thank Tim Butterley and James Osborn who have helped me with anything from small questions to keeping me sane when observing. I would like to thank Richard Myers who encouraged me to participate in departmental activities. I am also grateful to the Science and Technology Facilities Council for their financial support.

CfAI has been an amazing group to be a part of, and that is due to all the staff and students who made coming into work fun and engaging. There was always someone to turn to for help and in particular I want to thank Tim, James, Ollie, Matt, Andrew and Dougie.

I would like to thank my original office mates: Dora, Matt, Tom and Scott who were so welcoming when I started, and Daniel who embarked on this PhD journey with me. Also thanks to Penny and Huizhe who joined us in PH117, making it an even more special place to work. To my office mates of OCW011: thank you to Dashwood for putting up with my bombardment of questions, to Mark for the buzzfeed quizzes and cinema trips, to Abi who brought sunshine to our office and to Amrit who always understood. I would like to give special thanks to: David for great movie choices, we will always have Mullholland Drive; Dougie for the strawberry Caipiroskas and the BK; and Nicolas who was always a worthy debate partner.

So many people made my time in Durham memorable. Everyone at Van Mildert MCR in my first year who were like a family. The breakfast club: Andrew, Tim, Helen, Paddy and Sownak who brightened up the very early mornings. Playing

with the Ustinov Women's Basketball Team was always a great way to blow off steam. I would also like to thank the most important establishment in Durham, Fabios, a place I could always rely on.

There are two people in particular that made Durham home for me. Martin, I could not have asked for a better house mate to come home to and I will always remember our time together with Diane. And of course Marisa, who brings laughter, dancing and energy to everyone she meets and has been my partner in crime for the last four years. My life in Durham would not have been the same without her.

Outside of Durham I would like to thank Charlotte, who even at 250 miles away continued to be a shoulder for me to lean on. I am so grateful to Alex who for the last eight years has been my rock, always cheering me on in everything that I do. Finally, I would like to thank the most important people in my life, who have always been my support, my Mum, Dad and sister Dharithri. I feel eternally blessed.

---

# Contents

<b>Declaration</b>	<b>ix</b>
<b>List of Figures</b>	<b>x</b>
<b>List of Tables</b>	<b>xv</b>
<b>Nomenclature</b>	<b>xvi</b>
<b>1 Introduction</b>	<b>1</b>
1.1 Requirements for Astronomy . . . . .	1
1.2 Thesis Synopsis . . . . .	2
<b>2 Theory: Atmospheric Turbulence</b>	<b>4</b>
2.1 Origin of Turbulence . . . . .	5
2.1.1 Kolmogorov Model . . . . .	7
2.2 Atmospheric Effects on Astronomical Imaging . . . . .	9
2.2.1 Seeing Effects on Astronomical Imaging . . . . .	10
2.2.2 Scintillation Effects on Astronomical Imaging . . . . .	14
2.3 Simulations . . . . .	17
2.3.1 Simulating Phase Screens . . . . .	17
2.3.2 Optical Propagation . . . . .	18
2.3.3 Using the Simulations . . . . .	20

2.4	Conclusion	23
<b>3</b>	<b>Theory: Optical Turbulence Profilers</b>	<b>24</b>
3.1	Shack-Hartmann Wavefront Sensor	25
3.2	DIMM	26
3.2.1	Accuracy of the DIMM	29
3.2.2	DIMM Variations	31
3.2.3	Advantages & Disadvantages of the DIMM	31
3.3	MASS	32
3.3.1	Accuracy and Precision	34
3.3.2	MASS-DIMM	35
3.4	SLODAR	36
3.4.1	Obtaining $r_0$	38
3.5	SCIDAR	41
3.6	Conclusion	44
<b>4</b>	<b>SHIMM</b>	<b>46</b>
4.1	System Design & Hardware Configuration	47
4.1.1	Design Considerations	47
4.1.2	Hardware	53
4.1.3	Software Requirements	58
4.2	Observing Procedure	58
4.2.1	Setup & Alignment	58
4.2.2	Target Acquisition	59
4.2.3	Data Acquisition	60
4.3	Data Reduction	60
4.3.1	Data Processing	60
4.3.2	Calculating $r_0$	64
4.4	Noise Analysis	67
4.5	On-Sky Tests	68

4.5.1	SHIMM Data . . . . .	69
4.5.2	Comparison with Other Instruments . . . . .	71
4.6	Conclusions and Futher Work . . . . .	80
<b>5</b>	<b>SHIMM: Measuring the Atmospheric Coherence Timescale</b>	<b>81</b>
5.1	Covariance Map Method . . . . .	83
5.1.1	With Common Motion . . . . .	84
5.1.2	Without Common Motion . . . . .	90
5.1.3	Conclusion . . . . .	93
5.2	Power Spectrum Method . . . . .	95
5.2.1	Single Layer . . . . .	98
5.2.2	Two Layers . . . . .	101
5.3	On-Sky Results . . . . .	102
5.3.1	Data Reduction . . . . .	102
5.3.2	Results . . . . .	103
5.3.3	Limitations & Noise . . . . .	110
5.4	Conclusion & Future Work . . . . .	111
<b>6</b>	<b>SHIMM: Optical Turbulence Profile and Correction of Seeing</b>	
	<b>Measurements for Scintillation</b>	<b>112</b>
6.1	Effects of Scintillation . . . . .	115
6.2	Single Layer Turbulence Profiles . . . . .	119
6.2.1	Interpolation . . . . .	119
6.2.2	Model . . . . .	120
6.3	Two Layer Turbulence Profiles . . . . .	122
6.4	Three Layer Turbulence Profiles . . . . .	123
6.4.1	Correction of $r_0$ . . . . .	127
6.4.2	Profiling . . . . .	127
6.5	On-Sky Results . . . . .	132
6.5.1	Results . . . . .	132

6.5.2	Limitations & Noise . . . . .	143
6.6	Conclusions and Futher Work . . . . .	144
6.7	FASS-SHIMM . . . . .	145
6.7.1	Concept . . . . .	146
6.7.2	Hardware & Software . . . . .	148
6.7.3	On-Sky Results . . . . .	154
6.7.4	Future Work & Conclusions . . . . .	155
<b>7</b>	<b>Summary of Conclusions</b>	<b>158</b>
7.1	Atmospheric Theory . . . . .	158
7.2	Profiler Theory . . . . .	158
7.3	Estimating $r_0$ . . . . .	159
7.4	Estimating $\tau_0$ . . . . .	159
7.5	Estimating a Profile . . . . .	160
7.6	Future Work . . . . .	160
	<b>Appendix A Noise Analysis of SHIMM</b>	<b>161</b>
	<b>Bibliography</b>	<b>164</b>

---

# Declaration

The work in this thesis is based on research carried out at the Centre for Advanced Instrumentation, Department of Physics, University of Durham, England. No part of this thesis has been submitted elsewhere for any other degree or qualification, and it is the sole work of the author unless referenced to the contrary in the text.

Some of the work presented in this thesis has been published in journals and conference proceedings - the relevant publications are listed below.

## Publications

**S. Perera**, R. W. Wilson, J. Osborn & T. Butterley (2016), SHIMM: a seeing and turbulence monitor for astronomy, Proc. SPIE 9909, adaptive Optics Systems V, 9903J

A. Guesalaga, **S. Perera**, J. Osborn, M. Sarazin, B. Neichel (2016), FASS: the full aperture seeing sensor, Proc. SPIE 9909, Adaptive Optics Systems V, 99090H

A. Guesalaga, J. Osbron, M. Sarazin, B. Neichel, **S. Perera**, R. W. Wilson, P. Wizinowich (2015), An Integrated MASS/DIMM Monitor Based on a Low-Noise CCD Detector. Adapt. Opt. Extrem. Large Telesc. 4 - Conf. Proc 1(1).

**Copyright © 2017 by Saavidra Perera.**

*“The copyright of this thesis rests with the author. No quotation from it should be published without the author’s prior written consent and information derived from it should be acknowledged”.*

---

# List of Figures

2.1	Illustration of atmospheric opacity for different wavelengths. . . . .	5
2.2	Illustration of typical atmospheric conditions in terms of altitude and temperature. Taken from Russell (2009). . . . .	7
2.3	Simulated averaged speckle images showing how an increase in exposure time leads to a seeing limited PSF. . . . .	11
2.4	Illustration of the first 15 Zernike Polynomials . . . . .	13
2.5	Illustration oh how scintillation noise occurs. . . . .	15
2.6	Demonstration of how the scintillation pattern changes with propagation distance. . . . .	16
2.7	A simulated optical phase screen with a Kolmogorov spectrum of aberrations. . . . .	19
2.8	Results from testing the Fresnel Propagator in simulation. . . . .	21
2.9	Simulation of a seeing limited PSF. . . . .	22
3.1	Illustration of the SHWFS concept. . . . .	26
3.2	Illustration of the classical DIMM . . . . .	27
3.3	Illustration of how the transverse and longitudinal directions are defined with respect to the vector separations of the subapertures. . . . .	28
3.4	Illustration of the principles of MASS. . . . .	33
3.5	Weighting functions and response of the MASS. . . . .	34

3.6	Illustration of SLODAR geometry. . . . .	37
3.7	Example of a 2-D spatial cross-covariance map generated from SLODAR data. . . . .	39
3.8	Example SLODAR theoretical impulse response functions. . . . .	40
3.9	SLODAR method for estimating noise. . . . .	41
3.10	Illustration of how SCIDAR measures turbulence at different altitudes. .	43
4.1	Image of the SHIMM. . . . .	47
4.2	Schematic of the SHIMM optics. . . . .	49
4.3	Simulated results showing the effects of exposure time on the estimate of $r_0$ . . . . .	51
4.4	Histogram of wind speeds recorded by Stereo-SICDAR . . . . .	52
4.5	Simulated results showing the effects of wind speed on the estimate of $r_0$ . .	53
4.6	Image of the SHIMM WFS optics. . . . .	56
4.7	Illustration of the WFS mapped onto the C9-SHIMM and the resulting spot pattern. . . . .	56
4.8	Retractable windbreaks on the roof of the INT. . . . .	57
4.9	Results comparing the SHIMM and DIMM centroiding method. . . . .	63
4.10	Example of a simulated centroid spatial auto-covariance map. . . . .	64
4.11	Illustration of how $r_0$ is measured from a 1-D slice of an auto-covariance map. . . . .	66
4.12	Simulated results for the estimate of $r_0$ for the C9-SHIMM configuration. .	66
4.13	Illustration of how the SHIMM measures noise. . . . .	68
4.14	On-sky examples of a 1-D slice of an auto-covariance map taken from C9-SHIMM data. . . . .	75
4.15	Histogram of on-sky seeing measurements from the C9-SHIMM in La Palma. . . . .	76
4.16	Comparison on-sky results of two C9-SHIMMs. . . . .	76
4.17	Comparison on-sky noise estimates from two C9-SHIMMs at La Palma. . . .	77
4.18	Simulated results showing the convergence in the measurement of $r_0$ . . . .	78

4.19	Comparison on-sky results with the C9-SHIMM and the Stereo-SCIDAR and RoboDIMM at La Palma. . . . .	79
5.1	Illustration of the illuminated subapertures of the WFS mapped onto the C11-SHIMM telescope aperture, where each subaperture is 4.7 cm. . . . .	82
5.2	Simulated spatio-temporal auto-covariance map for the C11-SHIMM. . . . .	84
5.3	Velocity map associated with each subaperture separation. . . . .	86
5.4	1-D slice of spatio-temporal auto-covariance maps with turbulent layers of different wind velocities. . . . .	87
5.5	1-D slice of spatio-temporal auto-covariance maps with turbulent layers of different wind velocities, with background subtraction. . . . .	87
5.6	Simulated results from estimating the velocity of a single turbulent layer. . . . .	88
5.7	Simulated results from estimating $v_{eff}$ for a two turbulent layer profile. . . . .	89
5.8	Simulated spatio-temporal auto-covariance map, with common motion subtraction. . . . .	90
5.9	Simulated result of the estimation of wind speed of a single turbulent layer, with common motion subtraction. . . . .	91
5.10	Simulated results of the estimate of $v_{eff}$ for a two layer turbulence profile, with common motion subtraction. . . . .	92
5.11	1-D slice of spatio-temporal auto-covariance maps with turbulent layers of different wind velocities, with common motion subtraction. . . . .	93
5.12	Example of an on-sky spatio-temporal auto-covariance map at $\delta t = 0, 5, 10$ ms. . . . .	94
5.13	Example of an on-sky spatio-temporal auto-covariance map at $\delta t = 0, 5, 10$ ms. . . . .	94
5.14	Example of an on-sky spatio-temporal auto-covariance map at $\delta t = 0, 5, 10$ ms. . . . .	95
5.15	Simulated power spectra of centroid datasets for the C11-SHIMM configuration. . . . .	96
5.16	Simulated example of $P_j^{norm}$ for different Zernike modes. . . . .	98

5.17	Method for measuring wind speed from $P_j^{norm}$ . . . . .	99
5.18	Simulated results for estimating the wind speed of a turbulent layer from the Zernike defocus power spectrum. . . . .	100
5.19	Results for estimating $v_{eff}$ from the Zernike power spectra. . . . .	101
5.20	Examples of power spectra from on-sky data. . . . .	105
5.21	Histogram of $v_{eff}$ obtained from on-sky results by the C11-SHIMM in La Palma. . . . .	107
5.22	Histogram of $v_{eff}$ measured by Stereo-SCIDAR. . . . .	108
5.23	Power spectra for diffracted limited spots with shot noise. . . . .	108
5.24	Histogram of $\tau_0$ measurements obtained on-sky by the C11-SHIMM at La Palma. . . . .	109
5.25	Histogram of $\tau_0$ measured by the Stereo-SCIDAR. . . . .	109
6.1	Simulated results showing the effects of scintillation on the measurement of $r_0$ . . . . .	117
6.2	Simulated results showing the effects of scintillation on a 1-D slice taken from an auto-covariance map. . . . .	118
6.3	Simulated results from the interpolation method for correcting scintil- lation effects on $r_0$ , for a single layer turbulence profile. . . . .	120
6.4	Simulated results from the reference look-up table method for correcting scintillation effects on $r_0$ , for a single layer turbulence profile. . . . .	121
6.5	Example of simulated results after correcting scintillation effects on $r_0$ for a two layer turbulence profile, by using the reference look-up table method. . . . .	123
6.6	Reference look-up tables for a three layer turbulence profile. . . . .	126
6.7	Example of simulated results after correcting scintillation effects on $r_0$ for a three layer turbulence profile, by using the reference look-up table method. . . . .	128
6.8	Example simulated results when the reference look-up table method correctly estimate three layer turbulence profiles. . . . .	130

6.9	Example simulated results when the reference look-up table method incorrectly estimate three layer turbulence profiles. . . . .	131
6.10	Scintillation correction of on-sky $r_0$ estimates taken with the C11-SHIMM in La Palma. . . . .	133
6.11	Example of on-sky turbulence profiles sequences recorded with the C11-SHIMM in La Palma. . . . .	136
6.12	An example of on-sky measurements of scintillation information and the resulting turbulence profile, recorded with the C11-SHIMM in La Palma.	137
6.13	Example of on-sky turbulence profiles recorded with the C9-SHIMM and Stereo-SCIDAR in La Palma. . . . .	138
6.14	Examples of on-sky turbulence profiles recorded with Stereo-SCIDAR in La Palma. . . . .	139
6.15	On-sky comparisons of $\theta_0$ estimates from the Stereo-SCIDAR and the C9-SHIMM in La Palma. . . . .	140
6.16	On-sky comparison of binned turbulent layers between the Stereo-SCIDAR mounted on the INT and the C9-SHIMM. . . . .	142
6.17	Illustration of how a single simulated turbulent layer at a range of altitudes is binned in the three layer turbulence model. . . . .	143
6.18	Example of on-sky pupil images taken by the FASS showing different speckle patterns. . . . .	147
6.19	Image illustrating concentric rings used to obtain linear vectors from the FASS pupil image. . . . .	147
6.20	Dichroic spectral response of the beamsplitter used for the FASS-SHIMM.	148
6.21	Image of the FASS-SHIMM optics . . . . .	149
6.22	Schematic of the optical configuration of the FASS-SHIMM . . . . .	149
6.23	Example of non-vignetted and vignetted of FASS pupil images. . . . .	153
6.24	Example turbulence profile sequences of the FASS and Stereo-SCIDAR.	156
6.25	An example spatio-temporal auto-covariance map of the FASS pupil image. . . . .	157

---

# List of Tables

3.1	Comparisons of different turbulence profilers. . . . .	45
4.1	Lists the key components of two SHIMM models C9 and C11. . . . .	55
4.2	List of observations with the SHIMM and corresponding comparison instrument. . . . .	69
4.3	Comparisons with the SHIMM1 and SHIMM2 data . . . . .	77
6.1	FASS Specifications. . . . .	150

---

# Nomenclature

**AO** Adaptive Optics

**AT** Auxillary Telescope

**CCD** Charge-Coupled Device

**DIMM** Differential Image Motion Monitor

**EMCCD** Electron-Multiplying CCD

**ESO** European Southern Observatory

**FASS** Full Aperture Seeing Sensor

**FWHM** Full Width at Half Maximum

**ING** Isaac Newton Group of telescopes

**INT** Isaac Newton Telescope

**MASS** Multi Aperture Scintillation Sensor

**PMT** Photo-Multipler Tube

**PSF** Point Spread Function

**SCIDAR** SCIntillation Detection And Ranging

**SH** Shack Hartmann

**SHIMM** Shack Hartmann Image Motion Monitor

**SNR** Signal to Noise Ratio

**SLODAR** SLOpe Detection and Ranging

**WFS** WaveFront Sensor

**WHT** William Herschel Telescope

**VLT** Very Large Telescope

---

# Introduction

## 1.1 Requirements for Astronomy

The study of the night sky has always been a part of human history. Whether used to tell mythical stories or to act as a map to navigate our way through the dark, the night sky has played a role in many different cultures throughout time. As travel and technology improved, astronomy grew from a study within small communities, to a global area of research. Today, with observatories all over the world, we are able to study neighbouring planets, exotic stars and distant galaxies, all the way to the far reaches of our universe. For the next generation of ground based telescopes, to keep improving on this research, site selection is becoming increasingly crucial to maximise the gains of these instruments.

When selecting the location of an astronomical observing site for optical telescopes, several key factors must be considered: the climate, light pollution, the infrastructure and accessibility of the site, are a few examples. However, one of the most crucial determinants of the quality of astronomical imaging are the atmospheric conditions. The characterisation of atmospheric seeing and optical turbulence is necessary for the design and operation of modern ground-based optical telescopes.

Optical turbulence occurs when layers of air of different temperature mix, resulting in the aberration of starlight propagating through the atmosphere. The atmo-

spheric turbulence induces speckling and movement of the image, called ‘seeing’, as well as intensity fluctuations, called ‘scintillation’. Image quality and signal-to-noise of astronomical images and photometric measurements depends on the prevailing seeing and scintillation conditions during an observation. The long-term statistics of the seeing are critical for the optimal selection of observing sites. It is important to emphasise that the altitude of turbulent layers, as well as their strength, affect observations in different ways. Seeing (i.e. image distortion) results from all turbulent layers in the atmosphere. Scintillation however, predominately results from high altitude turbulence. Therefore, for example, it is possible to have overall bad seeing but low scintillation noise. For this reason, facility turbulence monitors play an important role for astronomical observations, with regards to site characterisation and the optimisation and queue-scheduling of observations.

One of the most commonly used seeing monitors is the Differential Image Motion Monitor (DIMM). As a low-cost instrument it is ideal for characterising the seeing of potential observing sites and for employing multiple instruments for multiple seeing comparisons. The SHIMM instrument is a variation on the traditional DIMM design, giving it not only the advantage of measuring the Fried parameter ( $r_0$ ) independent of noise, but also the ability to measure the coherence time ( $\tau_0$ ), and allow for low-resolution vertical profiling of the turbulence. This thesis will present the SHIMM instrument and will discuss its advantages with on-sky results.

## 1.2 Thesis Synopsis

- Chapter 2 discusses the theory behind atmospheric turbulence and the effects it has on astronomical imaging. Simulations used throughout this thesis are also described in this chapter.
- Chapter 3 presents key turbulence profilers and techniques that are currently employed by astronomical observing sites around the world. These seeing

monitors and profilers include the DIMM, MASS, SLODAR, and SCIDAR. All of these instruments will be mentioned in the proceeding chapters.

- Chapter 4 presents the SHIMM, an alternative instrument to the traditional DIMM. This variation employs a Shack-Hartmann lenslet array to image more focused spots than the traditional DIMM. This allows for utilising the SLODAR method for measuring  $r_0$ . This method, unlike that used by the DIMM, is independent of noise contributions. Comparisons with the SHIMM and other seeing instruments will be presented and discussed.
- Chapter 5 describes how the coherence time of the atmosphere can be estimated from SHIMM data. By employing a fast CCD camera, power spectra of the defocus Zernike term can be utilised to measure the effective velocity of the turbulence present in the atmosphere. From this the value of  $\tau_0$  can be acquired. Results from on-sky observations will be presented and discussed.
- Chapter 6 discusses the effects of scintillation on the measurement of  $r_0$ . This is a problem that also affects the DIMM. By using scintillation information from SHIMM data these effects can be corrected to provide a more accurate value of  $r_0$ . This information can also be used to produce a low-resolution fixed three layer turbulence profile. Examples of on-sky turbulence profiles will be presented. This chapter will also describe the Full Aperture Seeing Sensor (FASS), a novel technique that exploits a low noise EMCCD to image the full aperture pupil in order to measure the atmospheric turbulence profile. Examples of on-sky turbulent profiles acquired by the FASS will be presented. The FASS instrument is a collaborative development between Pontifical Catholic University of Chile, Chile and Durham University, UK. Since the FASS cannot sense turbulent layers close to the ground, the FASS and SHIMM have been combined, as will be discussed in chapter 6.

---

## Theory: Atmospheric Turbulence

The optical wavefront from an astronomical source is considered to be travelling an infinite distance, such that the arrival of this wavefront at the top of the Earth's atmosphere is planar. However, the atmosphere exhibits a number of different effects on this wavefront including absorption, scattering, dispersion and aberrations due to atmospheric turbulence.

The extent of the absorption of observed light is dependent on its wavelength as demonstrated by figure 2.1. It can be seen that wavelengths corresponding to radio, infrared and visible waves are transmitted through the Earth's atmosphere (Hardy, 1998). These are referred to as atmospheric windows. Unlike radio, optical and infrared wavelengths do not have 100% transparency. This is one of the main reasons that optical telescopes are generally located on mountain tops, since there is less atmosphere to absorb the light.

The type and amount of scattering of light is dependent on its wavelength and the size of the particle the light interacts with. For example, particles smaller than the wavelength of the incident light undergo Rayleigh scattering (Barry and Chorley, 1968). Due to the presence of  $NO_2$  and  $O_2$  the shorter blue light is more strongly scattered than red light in the atmosphere, hence the blue colour of the sky.

The refractivity of the atmosphere varies with altitude and wavelength, as will be described in section 2.1. As a result, incoming light at angles away from the

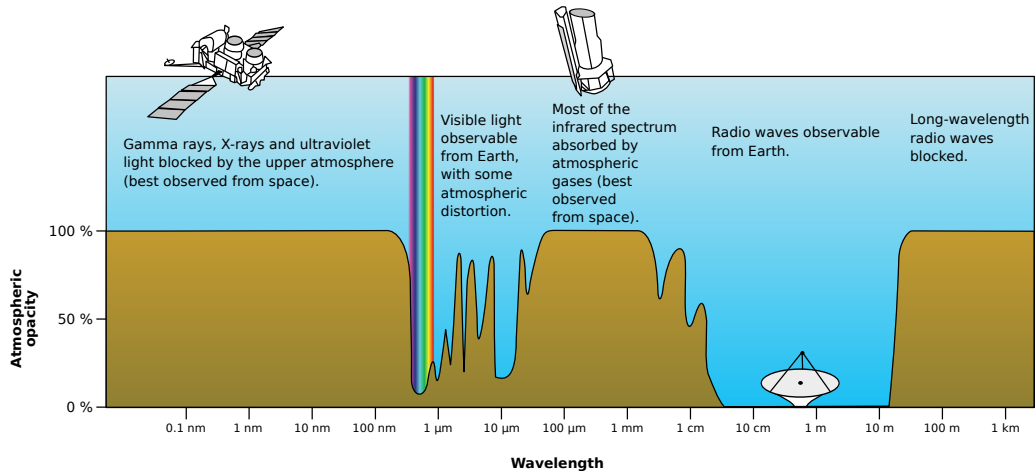


Figure 2.1: Illustration of atmospheric opacity for different wavelengths. Taken from NASA (2008).

zenith follow a curved path through the atmosphere, changing the apparent direction of celestial objects. It also causes dispersion, such that light of different wavelengths traverse different paths through the atmosphere and therefore smears out broadband images (Hardy, 1998).

Atmospheric turbulence is a phenomenon that corrupts astronomical imaging and photometry. Optical turbulence occurs when layers of air of different temperatures, and hence refractive index, mix. This results in the aberration of starlight propagating through the atmosphere. The atmospheric turbulence induces random speckling and movement of the image, called ‘seeing’, as well as intensity fluctuations, called ‘scintillation’.

## 2.1 Origin of Turbulence

In order for optical turbulence to occur, both dynamical turbulence and a refractive index gradient in the fluid must be present (Vernin, 2002). The first criteria, dynamical turbulence, can occur from wind shear at the Earth’s surface, solar heating

or interaction of air masses with atmospheric fronts, to name a few (Roddier, 1981). The second criteria is met when a vertical gradient of potential temperature, i.e the temperature that a parcel of air would attain if brought adiabatically to a reference pressure (Barry and Chorley, 1968), or density is present.

Turbulent flow is defined when the Reynolds number,

$$Re = \frac{vl}{\nu}, \quad (2.1)$$

exceeds a critical value which is dependent on the geometrical structure of the flow. Here  $v$  is the velocity,  $l$  is the length scale and  $\nu$  is the kinematic viscosity. Due to the low viscosity of air ( $\nu = 15 \times 10^{-6} m^2 s^{-1}$ ) the Reynolds number of the airflow in the atmosphere almost always exceeds this critical value, resulting in well developed turbulence (Hardy, 1998).

The typical structure and turbulence profile of the atmosphere is shown in figure 2.2. Generally, the strongest turbulent layers occur at sea level, since they have the highest air density. The mean turbulence strength decreases exponentially with increasing altitude, with the exception of the peak that occurs at the tropopause. This is a reason for locating observatories on mountain peaks (Hardy, 1998). The troposphere is the zone where nearly all weather phenomena occur. This zone contains about 80% of all atmospheric mass and most of the water vapour and aerosols in the atmosphere. In this region the temperature decreases with altitude until it reaches a temperature inversion level (i.e. a layer of relatively warm air above a cold layer) called the tropopause. The altitude of this level is dependent on the latitude and season, generally varying from 8 km at the poles to 16 km at the equator. Above the tropopause the stratosphere extends to about 50 km above sea level. The increasing temperature with altitude in this region is due to the absorption of the sun's ultraviolet radiation by the ozone layer (Barry and Chorley, 1968).

Due to varying temperatures and water vapour content, the atmosphere consists of layers of air with different refractive indices. This refractive index gradient together with dynamical turbulence results in temporal and spatial refractive

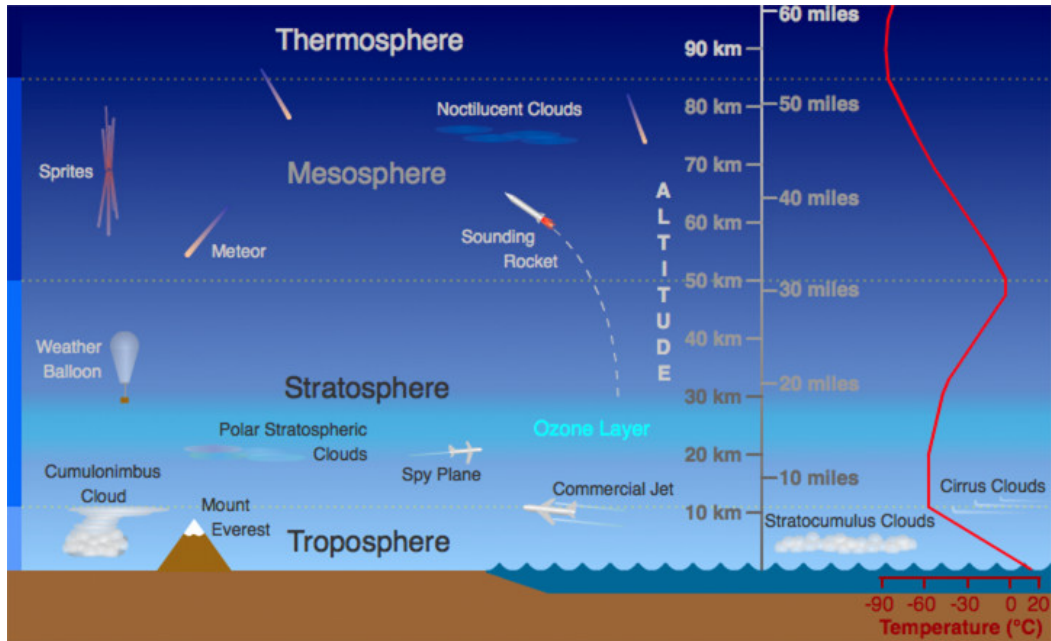


Figure 2.2: Illustration of typical atmospheric conditions in terms of altitude and temperature. Taken from Russell (2009).

index fluctuations. These fluctuations induce phase delays of different parts of the wavefronts, thereby deforming the otherwise plane wavefront.

### 2.1.1 Kolmogorov Model

The Kolmogorov atmospheric turbulence model is the most commonly used model to describe the mechanical structure of turbulence. It assumes that energy is inserted into a fluid medium on a large spatial scale, known as the outer scale ( $L_0$ ), and breaks down to form progressively smaller eddies. This continues until the turbulence energy is dissipated by the viscous properties of the medium at the inner scale ( $l_0$ ), i.e. where  $Re \approx 1$ . An example of observational evidence validating this model can be found in Nightingale and Buscher (1991).

The refractive index spatial fluctuations caused by atmospheric turbulence can be

described by a structure function,

$$D_n(r) = \langle [n(\epsilon) - n(\epsilon + r)]^2 \rangle, \quad (2.2)$$

$$= C_n^2(h) r^{\frac{2}{3}}, \quad (2.3)$$

where  $D_n(r)$  is dependent only on the difference in refractive index,  $n$ , of separation  $r$ , and not the position  $\epsilon$ , and  $\langle \rangle$  denotes an average (Hardy, 1998; Roddier, 1999). The refractive index structure constant,  $C_n^2(h)$ , of units  $m^{-\frac{2}{3}}$ , is a measure of the refractive index fluctuations, and is used to quantify the optical turbulence strength of layers at height,  $h$ . Since turbulent layers have a finite thickness it is more beneficial to look at the integrated refractive index structure constant between two altitude limits i.e.  $\int_{h_2}^{h_1} C_n^2(h) dh$  with units of  $m^{\frac{1}{3}}$  (Osborn, 2010). This gives the total integrated turbulence strength ( $C_n^2$ ) between the defined altitude limits.

The magnitude of modulation of the wavefront propagating through the turbulence is described by a structure function  $D(r) = D_\phi(r) + D_\chi(r)$ , where  $D_\phi(r)$  refers to a phase structure function and  $D_\chi(r)$  refers to an amplitude structure function. Under the condition of the near-field approximation i.e. where the amplitude effects are negligible for apertures greater than the Fresnel radius, the variance of scintillation will be much less than the variance of the phase. The Fresnel radius is defined as,

$$r_F = \sqrt{\lambda h}, \quad (2.4)$$

The phase structure function can be described as

$$D_\phi(r) = \langle [\phi(\epsilon) - \phi(\epsilon + r)]^2 \rangle, \quad (2.5)$$

As according to Hardy (1998), the phase structure function at the output of a thin layer with Kolmogorov turbulence is given by,

$$D_\phi(r) = 2.914k^2 \sec(Z) r^{\frac{5}{3}} \int_0^\infty C_n^2(h) dh, \quad (2.6)$$

where  $Z$  is the zenith angle. For small spatial separation Fried (1965) simplified this to,

$$D_\phi(r \ll L_0) = 6.88 \left( \frac{|\mathbf{r}|}{r_0} \right)^{\frac{5}{3}}, \quad (2.7)$$

where  $r_0$  is the Fried parameter (Hardy, 1998). This parameter is a scale length that quantifies the integrated optical turbulence strength. The Fried parameter relates to  $C_n^2(h)$  by

$$r_0 = \left( 0.423k^2 \sec(Z) \int_0^\infty C_n^2(h) dh \right)^{-\frac{3}{5}}, \quad (2.8)$$

where  $k = 2\pi/\lambda$  is the wavenumber and  $\lambda$  is the wavelength. The Fried parameter ( $r_0$ ) is an important measurement for monitoring atmospheric optical turbulence, it is defined as the diameter of a circular aperture where the residual phase variance is  $1 \text{ rad}^2$ . Other important parameters are the isoplanatic angle ( $\theta_0$ ) and coherence timescale ( $\tau_0$ ). The isoplanatic angle is the angular distance between two points on the sky over which the residual atmospheric wavefront phase variance is  $1 \text{ rad}^2$ , and can be defined as

$$\theta_0 = 0.314 \frac{r_0}{h_{eff}}, \quad (2.9)$$

where  $h_{eff}$  is the effective turbulence altitude

$$h_{eff} = \left[ \frac{\int_0^\infty C_n^2(h) h^{\frac{5}{3}} dh}{\int_0^\infty C_n^2(h) dh} \right]^{\frac{3}{5}}. \quad (2.10)$$

The coherence time is a measure of the timescale of the turbulence variation, and can be defined as

$$\tau_0 = 0.314 \frac{r_0}{v_{eff}}, \quad (2.11)$$

where  $v_{eff}$  is defined as

$$v_{eff} = \left[ \frac{\int_0^\infty C_n^2(h) V(h)^{\frac{5}{3}} dh}{\int_0^\infty C_n^2(h) dh} \right]^{\frac{3}{5}}, \quad (2.12)$$

describing the effective velocity of turbulence where  $V(h)$  denotes the velocity profile with altitude.

## 2.2 Atmospheric Effects on Astronomical Imaging

There are two main effects of atmospheric optical turbulence on astronomical imaging; seeing and scintillation. In this section both effects will be discussed.

### 2.2.1 Seeing Effects on Astronomical Imaging

An image is formed by the interference of the light from every part of the wavefront with the wavefront. When a flat wavefront propagates through a telescope of aperture,  $D$ , it focuses to a diffraction limited point spread function (PSF), where the full width half maximum (FWHM) can be given as

$$FWHM = 0.98 \frac{\lambda}{D}. \quad (2.13)$$

The imaging resolution is defined according to the Rayleigh criterion. This criterion states that the angular resolution is met when the peaks of two point sources, of equal brightness, coincide with the first diffraction ring of the other point source (Hardy, 1998). For a circular aperture this is given as

$$\theta = 1.22 \frac{\lambda}{D}. \quad (2.14)$$

However, in the presence of the atmosphere, the plane wavefront is distorted by refractive index fluctuations, and optical path differences are induced for different parts of the wavefront. The interference of this distorted wavefront with itself results in short exposure images becoming speckled, where each speckle is approximately the same size as the diffraction limited PSF. Following propagation through Kolmogorov turbulence the phase variance across the telescope aperture is given by (Roddier, 1999),

$$\sigma^2 = 1.03 \left( \frac{D}{r_0} \right)^{\frac{5}{3}}. \quad (2.15)$$

If  $D \ll r_0$  the image becomes effectively diffraction limited since the phase variance will be very small. When  $D \gg r_0$ , the image is said to be ‘seeing limited’, and appears speckled since there will be significant phase aberrations in the wavefront. As the phase aberrations evolve with time, so will the speckle patterns. Therefore a long exposure image will be the accumulation of the speckle patterns over time and will converge to the seeing limited PSF. Figure 2.3 demonstrates this through simulation. The FWHM of the image is dependent on  $r_0$ , and independent of the

telescope aperture size. This is known as the atmospheric seeing angle,

$$\theta_{FWHM} = 0.98 \frac{\lambda}{r_0}. \quad (2.16)$$

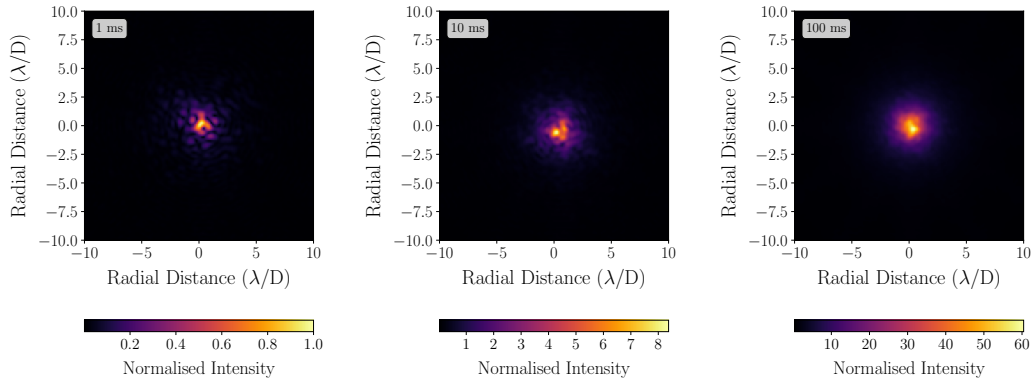


Figure 2.3: Simulated averaged speckle images for 1 ms, 10 ms and 100 ms, where  $D/r_0 = 2$ , as expected for a small telescope in the visible such as the SHIMM. This shows how increasing the exposure time will lead to a seeing limited PSF.

As demonstrated by the effects of optical turbulence on the PSF, in figure 2.3, it is clear that the atmosphere can degrade the performance of telescopes, in particular for large telescopes. As a result, adaptive optics (AO) is employed to correct for the effects of image speckling and motion (Roddier, 1999). The design, operation and optimisation of AO systems requires a detailed knowledge of the optical turbulence profile (Wilson, 2002).

### Zernike Polynomials

Here Zernike expansion is introduced as it will be used for measuring the value of  $\tau_0$ , as discussed in chapter 5.

When correcting for aberrated wavefronts a minimum residual wavefront error is desired. This can be done by expanding the wavefronts in a series of orthogonal

functions (Roddier, 1999). Noll (1976) showed that Zernike polynomials can be used to describe the statistical strength of aberrations produced by atmospheric turbulence entering a telescope aperture. Since Zernike polynomials are an orthogonal expansion over the unit circle, it can be described in polar coordinates  $(r, \rho)$ . Each Zernike mode is comprised of a normalisation factor, a radial component and an azimuthal component, and are defined by

$$Z_n^m(r, \rho) = \sqrt{(n+1)R_n^m} \begin{cases} \sqrt{2} \cos(m\rho) & \text{if } m \neq 0 \text{ and even } j \\ \sqrt{2} \sin(m\rho) & \text{if } m \neq 0 \text{ and odd } j \\ 1 & \text{if } m = 0 \end{cases}, \quad (2.17)$$

where

$$R_n^m = \sum_{s=0}^{(n-m)/2} \frac{(-1)^s (n-s)!}{s! \left[\frac{(n+m)}{2} - s\right]! \left[\frac{(n-m)}{2} - s\right]!} r^{n-2s} \quad (2.18)$$

are the Zernike polynomials. The index  $n$  is the radial degree and  $m$  is the azimuthal degree (Roddier, 1999). An index  $j$  is used as a mode ordering number and is a function of  $n$  and  $m$ . Even values of  $j$  correspond to symmetric modes  $\cos(\rho)$  and odd corresponds to antisymmetric modes  $\sin(\rho)$ .

The Zernike Polynomials are a complete set (Hardy, 1998). Figure 2.4 illustrates the first 15 Zernike Polynomials, which includes aberrations of conventional optical systems such as piston, tip/tilt, defocus and astigmatism.

Wavefront phase distortions  $\phi(\mathbf{r})$ , where  $\mathbf{r}(r, \rho)$  is a vector, over a circular aperture can be expanded as a sum of Zernike modes. If the first  $J$  modes are corrected, the correction can be written as

$$\phi(\mathbf{r}) = \sum_{j=1}^J a_j Z_j(\mathbf{r}), \quad (2.19)$$

where  $a_j$  is the Zernike coefficient for each Zernike mode.

Noll (1976) obtained a Zernike matrix representation of the power spectrum of the phase fluctuations due to Kolmogorov turbulence by evaluating the covariance expansion of the coefficients  $a_j$ . This is often known as the Noll matrix. The

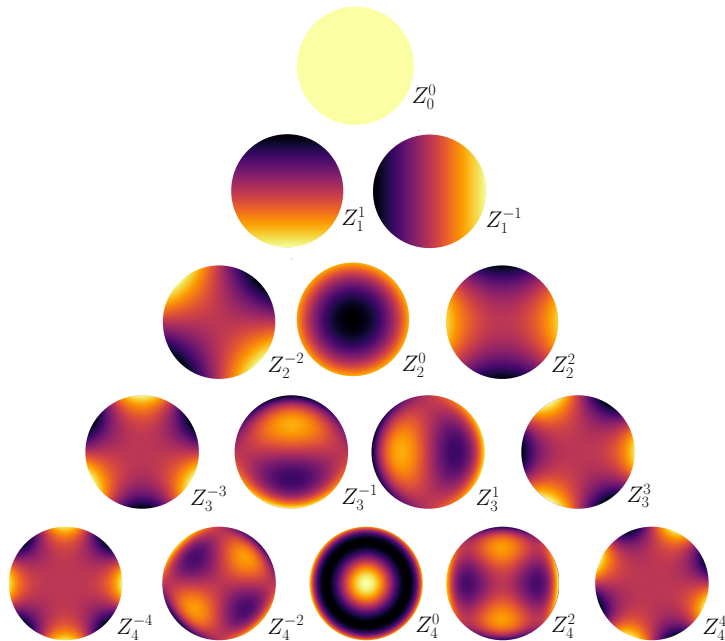


Figure 2.4: Illustration of the first 15 Zernike Polynomials generated using AOtools (Townson et al., 2017).

mean square residual error of this correction described by 2.2.1 under Kolmogorov turbulence is given as

$$\Delta_J = \langle \phi^2 \rangle - \sum_{j=1}^J \langle |a_j|^2 \rangle, \quad (2.20)$$

where  $\langle \phi^2 \rangle$  is the phase variance. For the Kolmogorov power spectrum the phase variance is infinite for the piston mode, and finite for consecutive modes. The numerical values for this residual phase variance can be found in Noll (1976).

### Fitting Zernike Coefficients to WFS Data

Simulation code for obtaining Zernike Coefficients, for a given dataset of measured wavefront slopes, was provided courtesy of Ollie Farley. The Zernike polynomials were calculated using the python module AOtools (Townson et al., 2017). The gamma matrices (which express the gradient of the Zernike functions as sums of the

Zernike terms themselves) from Noll (1976) were used to generate a matrix of the slope of each Zernike term averaged over each wavefront sensor (WFS) subaperture. A dot product of this matrix with the dataset of measured wavefront slopes will produce the Zernike coefficients.

## 2.2.2 Scintillation Effects on Astronomical Imaging

Scintillation is the spatial intensity fluctuation due to propagation of the aberrated wavefront caused by atmospheric turbulence. The interference of the wavefront with itself creates a pattern of ‘flying shadows’ in the pupil plane. Figure 2.5 demonstrates light from one part of the wavefront being redirected to other parts of the pupil producing a flying shadow at the pupil plane. With respect to astronomical photometry, this creates random fluctuations of the measured intensity as light is deviated into or out of the telescope aperture. Since wind moves the turbulence across the field of view of the telescope, this causes temporal fluctuations of the total integrated intensity of the image (Osborn et al., 2011).

The scintillation is directly affected by the propagation distance of turbulent layers, i.e. it is stronger for turbulence at higher altitudes. The characteristic scale of the structures in the flying shadow scintillation patterns is determined by the Fresnel radius, given by equation 2.4. Figure 2.6 demonstrates how increasing the altitude of a turbulent layer changes the spatial scale of the flying shadow patterns, as well as the increasing intensity variations at the pupil plane.

The scintillation index is used to quantify the amount of scintillation that is present, and is expressed as

$$\sigma_I^2 = \frac{\langle I^2 \rangle - \langle I \rangle^2}{\langle I \rangle^2}, \quad (2.21)$$

where  $I$  is the intensity of the image and  $\langle \rangle$  denotes time averaging. The scintillation noise can therefore be found by calculating  $\sqrt{\sigma_I^2}$ . Osborn et al. (2015) describes how scintillation noise can be estimated depending on the exposure time,  $t$ , telescope diameter,  $D$ , and the wind velocity profile,  $V(h)$ . In general, astronomical imaging

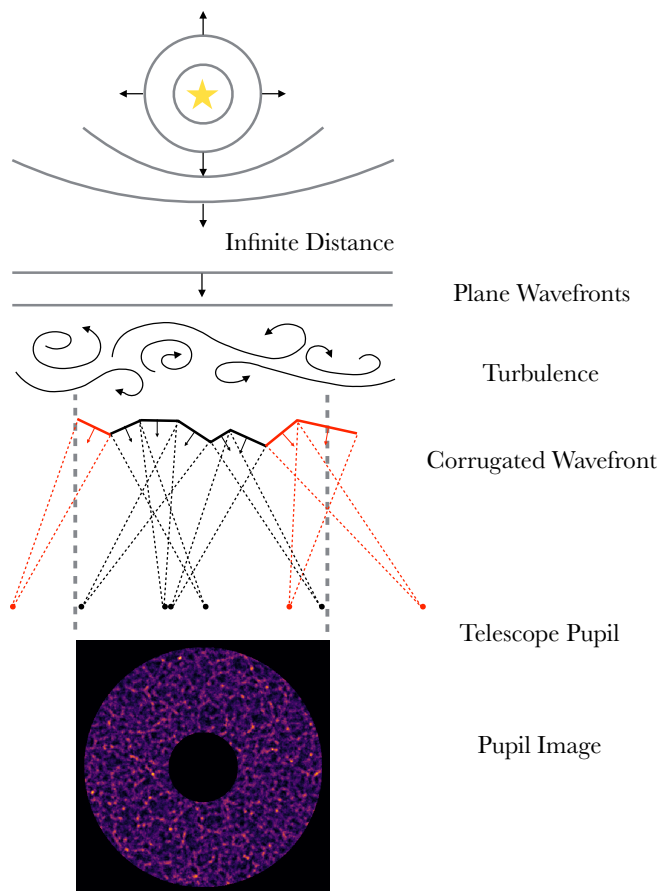


Figure 2.5: A simplified illustration of how scintillation noise occurs when light is focused into the telescope pupil or away from the pupil by a turbulent atmosphere. Adapted from Osborn et al. (2011).

is in the long exposure regime. The scintillation index for long exposures is given by

$$\sigma_{I,le}^2 \propto D^{-\frac{4}{3}} t^{-1} \int_0^\infty \frac{h^2 C_n^2(h)}{V(h)} dh. \quad (2.22)$$

This equation illustrates the importance of estimating the optical turbulence profile in order to quantify the contribution of scintillation noise in photometric observations.

For many observations, such as direct imaging, a small  $\sigma_I^2$  value is unimportant. However, for high fidelity, time resolved photometry, for example the detection and

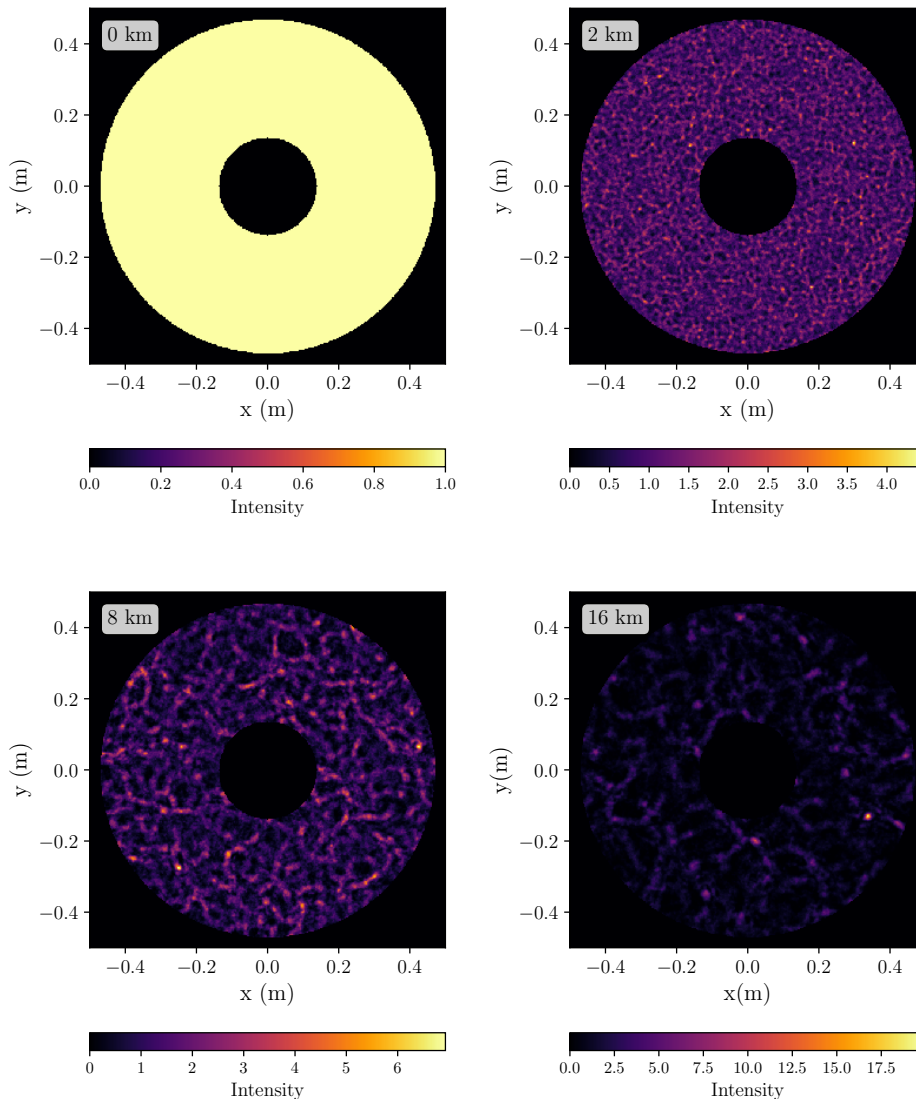


Figure 2.6: Demonstration of how the scintillation pattern changes with propagation distance.

characterisation of transiting exoplanets, small  $\sigma_I^2$  can be crucial. If a planet, or object, is orbiting a star in the line of sight of the telescope, the measured luminosity of that star will have periodic dips. These dips can be very small, typically 0.01% to 0.1%. Whilst this is within the capabilities of modern detectors, scintillation can induce photometric variations of the order of 0.1% to 1.0% (Osborn et al., 2015).

Scintillation therefore can become the limiting noise source for ground based observations. Fohring (2014) demonstrates an example where this is the case for transit observations of target magnitude  $V = 10$  or brighter. This is because for bright targets scintillation noise is much greater than shot noise. As for AO correction, real-time knowledge of turbulence parameters is critical. Methods to correct for the effect of scintillation in photometry are being developed (Osborn et al., 2011).

## 2.3 Simulations

The effects of atmospheric turbulence can be represented by generating simulated phase screens, typically by using several phase screens to represent the turbulence at different altitudes. Generating the complex 2-D aberrated wavefront observed at the telescope pupil involves propagating the aberrated wavefront from the atmospheric phase screen to the ground. This wavefront is then passed to the simulated imaging system. The theoretical methods are outlined in Ellerbroek (1994). The Durham AO simulation framework was developed to simulate adaptive optics systems on current and next generation extremely large telescopes (Basden et al., 2007). The simulations used for obtaining phase screens and the effects of optical propagation have been taken from this framework and are discussed below. All simulations and data plotting were performed using the Python programming language. The NumPy and SciPy libraries (van der Walt et al., 2011) as well as Astropy (Robitaille et al., 2013) and Matplotlib (Hunter, 2007) were employed by these simulations and data analysis throughout this thesis.

### 2.3.1 Simulating Phase Screens

A phase screen, with a Kolmogorov power spectrum of aberrations, is used to model the phase modulations after a wavefront propagates through a turbulent layer. According to Taylor's approximation the evolution of the turbulent structure is much slower than the advection of the turbulence (Higgins et al., 2012). Therefore,

the turbulent layer is considered to be ‘frozen’ as it moves across the telescope pupil.

To simulate phase modulated screens Gaussian white noise is generated and filtered by a spatial power spectrum of the turbulence,  $\Phi(\kappa)$ , to obtain a random field with the correct second order statistics. The Gaussian white noise is a complex variable field of the form  $(r(\kappa) + ir'(\kappa))$ , where  $\kappa$  is the spatial frequency variable and  $r$  and  $r'$  are random with zero mean and unit variance. The spatial power spectrum known as the von Karman power spectrum is defined as,

$$\Phi(\kappa) = \left| \kappa^2 + \left( \frac{W^2}{L_0} \right) \right|^{-\frac{11}{6}}, \quad (2.23)$$

where  $W$  is the width of the phase screen. Kolmogorov statistics hold when  $L_0 = \infty$ . However, in practise it is not possible to simulate for  $L_0 = \infty$ . This is not problematic since in reality  $L_0$  is finite, and typically of the order of 10 - 100 m (Buscher, 2015).

The atmospheric phase screen is the real part of the 2-D Fourier transformed product of  $\Phi(\kappa)$  and Gaussian white noise, and it is given as

$$PS = c. \text{Re} \left( \mathcal{F} \left[ \sqrt{\Phi(\kappa)} (r(\kappa) + ir'(\kappa)) \right] \right), \quad (2.24)$$

where  $\mathcal{F}$  denotes the 2-D Fourier transform,  $\text{Re}$  indicates the real component and  $c$  is a scaling factor

$$c = \frac{0.1517}{\sqrt{2}} \left( \frac{W^2}{r_0} \right)^{\frac{5}{6}}. \quad (2.25)$$

This parameter allows for the scaling of the turbulent strength of the phase screen according to the value of  $r_0$  associated with that layer. Figure 2.7 illustrates an example of a phase screen with a Kolmogorov spectrum of aberrations.

### 2.3.2 Optical Propagation

In order to simulate turbulent layers at different altitudes the optical propagation of the light between these layers also needs to be taken into account. The Fraunhofer

---

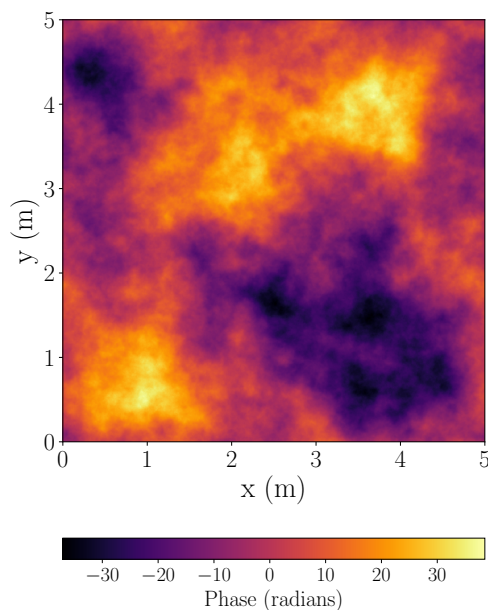


Figure 2.7: A simulated optical phase screen with a Kolmogorov spectrum of aberrations.

(far-field) approximation relies on the following assumption

$$z \gg \frac{k(x'^2 + y'^2)_{max}}{2}, \quad (2.26)$$

where  $z$  is the propagation distance,  $x'$  and  $y'$  are coordinates of the aperture. At optical frequencies, telescope apertures on the scale of meters and turbulent layers generally no higher than 20 km, do not fall under the far-field regime. Therefore, Fresnel (near-field) diffraction is applied (Goodman, 1968).

The Fresnel diffraction integral for an optical field, after passing through the  $n$ th atmospheric turbulent layer is given by,

$$U_n(x', y') = \iint_{-\infty}^{\infty} U_0(x, y) \frac{i}{\lambda z} \exp(ikz) \exp\left(\frac{ik}{2z}[(x - x') + (y - y')]^2\right) dx' dy', \quad (2.27)$$

where the vectors  $(x, y)$  and  $(x', y')$  indicate the coordinates of the initial and final propagation positions. This can be expressed as

$$U_n(x', y') = U_0(x, y) \otimes K(x, y, z), \quad (2.28)$$

where  $\otimes$  denotes a convolution between the incident field (i.e. the complex exponential of the atmospheric phase screen in equation 2.24) and the Fresnel propagation kernel,  $K(x, y, z)$ , defined as

$$K(x, y, z) = \frac{i}{\lambda z} \exp(ikz) \exp\left(\frac{ik}{2z}[(x - x') + (y - y')]^2\right). \quad (2.29)$$

In simulation equation 2.28 can be performed with the following Fourier transformations

$$U_n(x', y') = \mathcal{F}^{-1} [\mathcal{F}(U_n(x', y')) \times \mathcal{F}(K(z))], \quad (2.30)$$

where  $\mathcal{F}^{-1}$  denotes the inverse Fourier transform.

The real atmosphere typically consists of multiple thin layers of different turbulent strengths and heights. To simulate this the complex amplitude of the wave, generated from equation 2.24, is propagated down to the next layer via a convolution with the Fresnel Kernel of that height. This method is repeated for layers of decreasing altitude until the pupil plane.

The validity of the Fresnel propagator was tested by changing the image scale of the phase screen and comparing the input and measured  $r_0$  values. The method of estimating  $r_0$  is discussed in section 4.3.2. Figure 2.8 shows the estimated  $r_0$  against altitude for a range of image scale values when the phase screen had an  $r_0 = 0.1$  m. The increase in  $r_0$  with altitude is an effect of scintillation and is discussed in chapter 6. It can be seen that for an image scale smaller than 0.05 array element per meter (AE/m) the estimated  $r_0$  is the same for the corresponding altitudes, and will provide a fine enough sampling size. As a result, an image scale of 0.0026 AE/m was used since it is desirable to have a larger image scale so as not to require a larger number of phase screens for a single simulation, since this increases the computational time.

### 2.3.3 Using the Simulations

When using these simulations considerations need to be taken when defining parameters, such as the size of the phase screen and sampling.

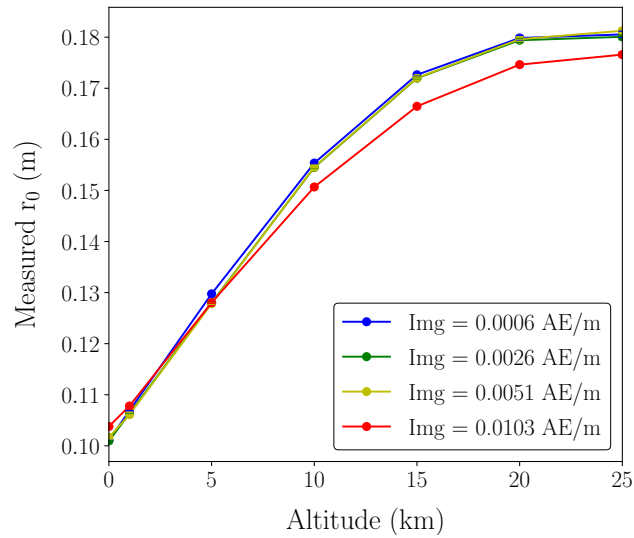


Figure 2.8: Results from testing the Fresnel Propagator used in simulation, for different image scales ( $Img$ ) of unit array element per m ( $AE/m$ ), where the input  $r_0 = 0.1$  m. Error bars, due to statistical uncertainty of the simulation, are too small to be seen on this graph.

When generating a phase screen in simulation a discrete Fourier transform is used, producing a periodic phase screen. As a result, the phase screen size must be significantly larger than the telescope aperture diameter and  $L_0$ .

### Obtaining a PSF

In order to simulate an instantaneous PSF the telescope aperture is ‘sliced’ from the complex field at the ground level, by multiplying the complex amplitude with an aperture mask array. The square of the Fourier transform of this gives the amplitude at the image plane. The pupil mask is made from an array of ones and zeros denoting the aperture and the padding respectively. To avoid aliasing the aperture in the pupil mask array must be padded such that it is at least Nyquist sampled, i.e. the mask needs to be at least double the size of the aperture. Figure 2.9 illustrates the use of a pupil mask with padding.

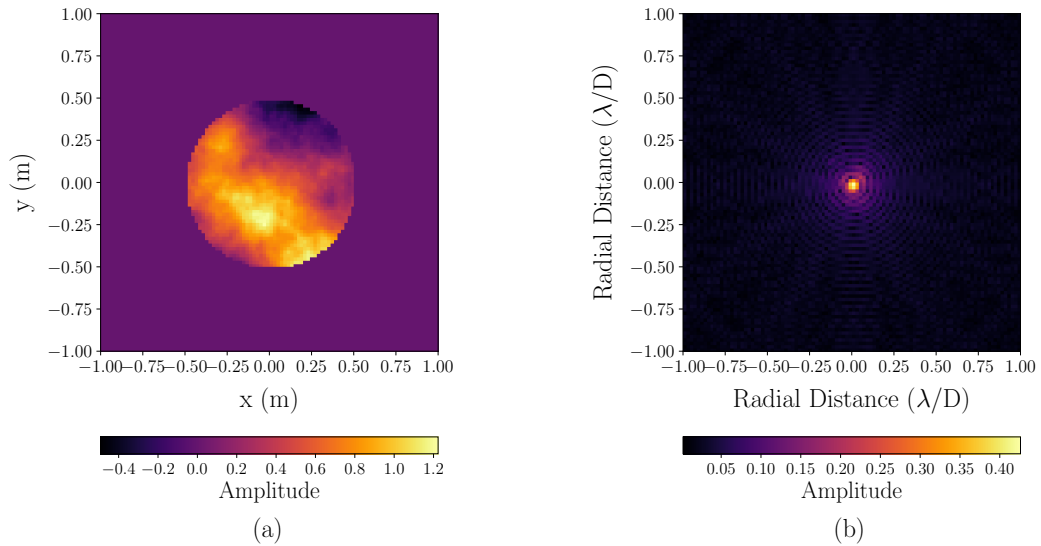


Figure 2.9: Example simulations of (a) the pupil mask multiplied by a phase screen, to indicate what can be seen by an aperture in the pupil plane and (b) the output of the squared Fourier transform of a complex field multiplied by the pupil mask.

### Simulating Wind & Finite Exposures

In order to simulate exposures of finite duration, multiple instantaneous exposures need to be summed. The number of these instantaneous PSF images is determined by the wind blown speed of the turbulent layer traversing the telescope aperture and the finite exposure time. Here a specific example, where the wind speed of a turbulent layer is 15 m/s, the exposure time is 10 ms and the sampling of the image plane is 0.01 m/array elements, is considered. In one exposure the phase screen will have moved 15 cm, i.e. 15 pixels. The phase screen is then shifted by small increments up to 15 array elements and instantaneous PSFs are created for each position. These are then summed to create the final PSF.

## 2.4 Conclusion

In this chapter the key principles and assumptions used in modelling optical atmospheric profiling have been presented. These principles act as the foundation on which the rest of this thesis is based. The Kolmogorov atmospheric turbulence model was discussed and key parameters such as  $C_n^2$ ,  $r_0$ ,  $\tau_0$  and  $\theta_0$ , that are used to characterise the atmosphere were presented. Knowledge of these parameters are required for the optimisation of AO and interferometry, as well as for site selection and queue scheduling for astronomy.

Atmospheric optical turbulence has two degrading effects on astronomical imaging; seeing and scintillation. Seeing manifests itself as image motion and blurring, and is caused by all turbulent layers in the atmosphere. Scintillation however, results in intensity fluctuations and occurs completely from high altitude turbulent layers. It is therefore possible to have bad seeing but low scintillation noise.

Finally fundamental simulations that allow for modelling of the atmospheric turbulence and the effects on astronomical imaging were presented. The key simulation is the generation of phase screens, used to represent the phase modulations after a plane wavefront propagates through a turbulent Kolmogorov atmosphere. In addition, the method of simulating propagation effects was also discussed.

---

# Theory: Optical Turbulence Profilers

This chapter explores key optical turbulence profilers that are currently employed by different observing sites across the world. All instruments outlined in this chapter will be referred to later in this thesis. These are discussed in order of increasing complexity, required telescope aperture size and cost. The most basic instrument, the Differential Image Motion Monitor (DIMM), is not a profiler but a seeing monitor, based on a small telescope, that estimates the total integrated turbulence strength (Sarazin and Roddier, 1989). The Multi Aperture Scintillation Sensor (MASS), like the DIMM, is based on a small telescope. It divides the aperture into four concentric rings, each connected to a Photo-Multiplier Tube (PMT). The photon counts are used to find the correlation between the scintillation patterns on a range of spatial scales to provide the turbulence strength for six bins at fixed altitudes (Kornilov et al., 2003).

The SLOpe Detection and Ranging (SLODAR) and SCIntillation Detection And Ranging (SCIDAR) are techniques that produce much higher resolution turbulence and wind profiles, and both require a telescope aperture  $\gtrsim 0.5$  m. The SLODAR is a crossed-beams technique that utilizes a Shack Hartmann wavefront sensor (SHWFS), described in the next chapter, to retrieve  $C_n^2(h)$  from the wavefront

slope correlations between a pair of target stars i.e. a double star (Wilson, 2002). The SCIDAR estimates the  $C_n^2(h)$  profile by measuring the correlation of the scintillation pattern produced by a double star (Vernin and Roddier, 1973). The SCIDAR instrument is generally the most expensive since it is typically mounted on a 1 – 2 m telescope in order to reach a higher resolution profile.

Many variations and combinations of these instruments have been made to create different profilers for specific profiling requirements or to improve on the current instruments. For example the principles of SCIDAR have been applied to a smaller 40 cm telescope observing wide angle double stars to produce LOw LAYER SCIDAR (LOLAS). This instrument obtains a detailed profile from the ground to 1 km altitude (Avila et al., 2008). Similarly Surface Layer SLODAR (SL-SLODAR) employed the principles of SLODAR to obtain a detailed surface layer profile (Osborn et al., 2010). The theory of SLODAR and SCIDAR have also been combined to create COupled SLodar scIDAR (CO-SLIDAR), by using scintillation and slope information to estimate a turbulence profile (Robert et al., 2008). The Generalized Seeing Monitor (GSM) is a monitor that employs four 10 cm telescopes (Ziad et al., 2000). Two of the telescopes acts like a DIMM, with the combination of all four telescopes aiming to measure  $\theta_0$  and  $L_0$ .

A tabled summary of the features and attributes of each instrument can be found in section 3.6.

### 3.1 Shack-Hartmann Wavefront Sensor

The SHWFS is commonly used for AO systems and is employed by SLODAR and similar turbulence profilers to reconstruct a phase map of the incoming wavefront. It consists of a 2-D array of lenslets of the same focal length and a position-sensing detector, typically a Charge-Coupled Device (CCD) camera. Under perfect conditions, when light arrives as a plane wave, an image is focused at a fixed position by each lenslet. However, as demonstrated by figure 3.1, when the incoming wave

is aberrated the focal spot of a lens will deviate from the expected position by  $\delta x = f\theta_{slope}$ , where  $f$  is the focal length of the lenslets and  $\theta_{slope}$  is the angle of the wavefront slope (Platt and Shack, 2003). The amplitude of this deviation provides information about the local tip and tilt of the wavefront across the subaperture.

Measurements of the centroid positions of the focused spots can be used to reconstruct a phase map of the wavefront, e.g. for AO correction. The SHWFS can also be used for tomographic reconstruction, which is a method employed to estimate the phase aberration in a volume along a different line of sight to a scientific target (Vidal et al., 2010).

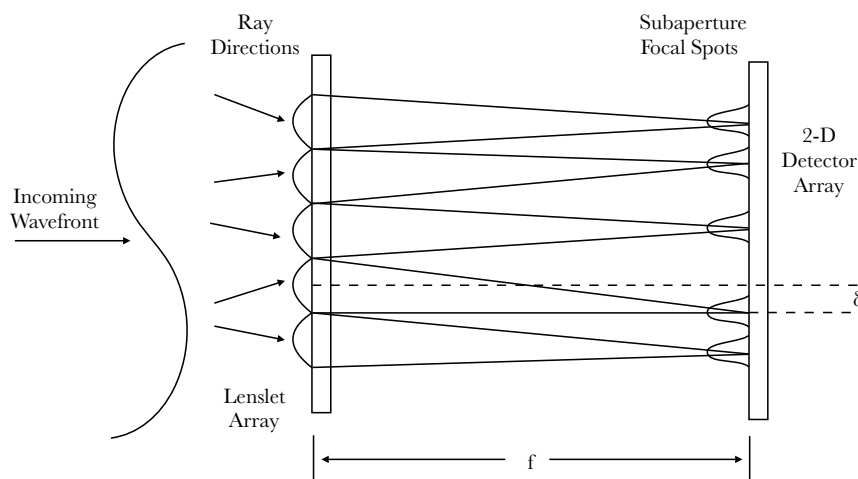


Figure 3.1: Concept of the SHWFS illustrating how displacements of focused spots from the lenslet represent wavefront tilt. Adapted from Platt and Shack (2003).

## 3.2 DIMM

The DIMM is a compact instrument, utilising a small telescope, which measures the differential motion for images of the target star produced by two subapertures within the telescope pupil, as depicted in figure 3.2. The two subapertures are produced by placing a mask over the entrance aperture of the telescope. A wedge prism is placed over one of the subapertures in order to separate the focused images

of the target star. Since it employs a differential method, measurements are insensitive to tracking errors and telescope shake, which have an equal effect on the two images (Sarazin and Roddier, 1989; Wilson et al., 1999). However, the turbulence causes small differential motions (O'Donovan et al., 2003). The variance of the differential motion is found from the centroid values,  $c_1$  and  $c_2$ , of the two spots formed on the detectors. This variance can be described as

$$\begin{aligned}\sigma^2 &= \langle |c_1 - c_2|^2 \rangle - \langle |c_1 - c_2| \rangle^2, \\ &= \sigma_{c_1}^2 + \sigma_{c_2}^2 - 2\text{cov}(c_1 c_2),\end{aligned}\tag{3.1}$$

where cov indicates the covariance of the two centroids.

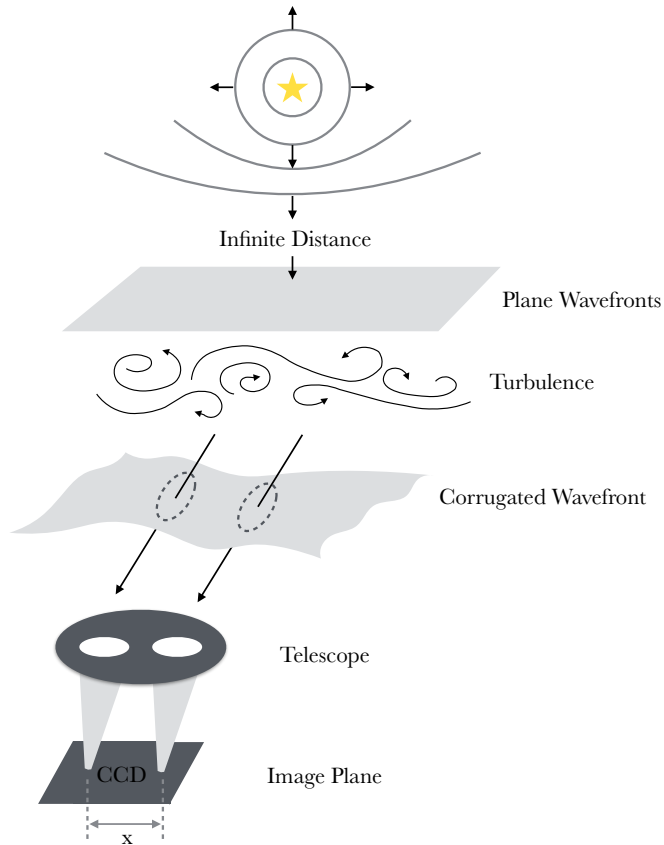


Figure 3.2: Illustration of the classical DIMM. Wavefronts distorted by the atmosphere are detected by a CCD via two subapertures focusing the light onto two spots separated by a distance  $x$ . Adapted from Tokovinin (2002).

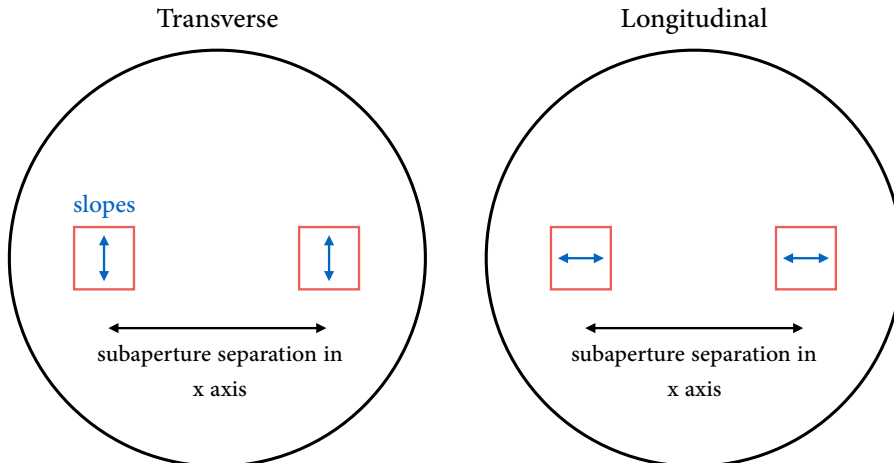


Figure 3.3: Illustration of the difference between transverse and longitudinal directions. When the slope of the wavefront is perpendicular to the spatial separation this is considered transverse. If the slopes are parallel then they are longitudinal.

The variance of this differential motion yields an estimate for  $r_0$ , and is defined as

$$\sigma_{\star}^2 = K_{\star} \left( \frac{\lambda}{D} \right)^2 \left( \frac{D}{r_0} \right)^{\frac{5}{3}}, \quad (3.2)$$

where  $K$  is a constant, known as the response coefficient, and  $D$  is the subaperture diameter. The subscript  $\star$  represents either of the two directions of motion, longitudinal and transverse to the vector separation of the subapertures. Figure 3.3 illustrates how longitudinal and transverse directions are defined. The Fried parameter is related to  $\theta_{FWHM}$  as according to equation 2.16. The seeing angle of a long-exposure image can be computed from differential motion measurements on a star at zenith distance  $Z$  by,

$$\theta_{FWHM} = 0.98 \left( \frac{D}{\lambda} \right)^{\frac{1}{5}} \left( \frac{\sigma_{\star}^2 \cos(Z)}{K_{\star}} \right)^{\frac{3}{5}}. \quad (3.3)$$

It is important to note that since the DIMM utilises a small telescope aperture it is insensitive to the low-frequency part of the turbulence spectrum and is therefore typically unaffected by the outer scale.

### 3.2.1 Accuracy of the DIMM

The accuracy of the seeing measured by the DIMM is affected primarily by exposure time, noise biases and optical propagation (Tokovinin and Kornilov, 2007). These parameters will to some degree also affect the accuracy of all other turbulence profilers.

#### Exposure Time

A very short exposure time is desired in order to freeze the image motion due to seeing, however the minimal usable exposure time is limited by the effects of shot noise. In practise, many DIMMs use an exposure time of 5-20 ms (Tokovinin, 2002). For a wind speed of 40 m/s, an exposure time of 5 ms would result in the turbulent layer moving by 20 cm, which is of comparable size to the aperture of most DIMM instruments. The resulting blurring of the image motion leads to an overestimation of  $r_0$ , i.e. an underestimation of the seeing angle. Short exposure times (e.g. 5 ms) reduce the bias, but does not completely remove it (Tokovinin and Kornilov, 2007).

A method which uses interlaced exposures of different lengths has been implemented in order to estimate and correct for this effect (Tokovinin, 2002). For short exposures ( $t$ ) and long exposures ( $2t$ ) seeing measurements  $\theta_1$  and  $\theta_2$  can be determined. From this the de-biased seeing is estimated as

$$\theta_0 \approx 0.5 \left( c \theta_1 + c^{\frac{7}{3}} \theta_2 \right), \quad (3.4)$$

where  $c = (\theta_1/\theta_2)^{\frac{3}{4}}$ . Whilst much of the effect of long exposures can be compensated, low or high wind speeds can result in small over- and undercorrections respectively (Tokovinin, 2002).

#### Noise Biases

Equation 3.1 demonstrates how the measured variance of the differential motion includes the variance of the individual centroids. These centroid variance values

will be affected by the presence of noise, and will therefore result in random and systematic errors in the measurement of  $r_0$ .

The DIMM is sensitive to two main sources of random error: detector noise and the statistical error associated with the finite number of image samples used for each seeing estimate (Sarazin and Roddier, 1989). The main instrumental noise contributions are shot noise and detector readout noise which result in uncertainty in determining the centroids. The details of estimating these noise contributions can be found in Tokovinin (2002). The limiting magnitude for the target star therefore depends on the subaperture diameter and the readout noise of the detector, normally a CCD (Sarazin and Roddier, 1989).

Statistical errors can be reduced by increasing the number of independent samples used to estimate the variance of the differential motion. For example, doubling the number of samples will reduce the statistical noise by a factor of  $\sqrt{2}$ , according to standard error. However, a too high frame rate can result in non-independent samples, and samples taken over too long a period will measure seeing that can change significantly within the data set.

Shot noise and detector noise increases the variance in the measurement of  $\sigma^2$ . Therefore, as shown in equation 3.1 they will also be biased. The noise level can not be measured directly by the DIMM and must be estimated from the magnitude of the target star and the exposure time, gain and specifications of the CCD. Any error in the noise estimation will introduce a bias into the estimation of  $r_0$ .

### **Optical Propagation**

Classical DIMM theory neglects propagation effects and considers only near-field turbulence. It was found that the value of the response coefficients (see equation 3.2) reduce with increasing propagation distance and reduce substantially for strong higher altitude layers (Tokovinin and Kornilov, 2007). A turbulence profile is therefore needed to determine what response coefficients should be used. Since this is

not possible with the DIMM, the instrument tends to underestimate the seeing and therefore overestimate the value of  $r_0$ .

Another important effect is due to optical aberrations of the DIMM. When there are optical aberrations, the variance of the differential image motion produced by high layer turbulence depends on factors such as the type of aberration and propagation distance. For example, defocus does not appear to bias the seeing measurement for a turbulent layer at the ground. However, a higher turbulent layer can result in a large bias which is also dependent on the sign of the defocus. These optical propagation effects are described in detail by Tokovinin and Kornilov (2007).

### 3.2.2 DIMM Variations

Many variations of the DIMM have been made including the DIMM Which Is Transportable (DIMMWIT) (O'Donovan et al., 2003), Generalized DIMM (GDIMM) (Aristidi et al., 2014) and Hartmann DIMM (H-DIMM) (Bally et al., 1996). The DIMMWIT uses the exact same principle as the DIMM but has the benefit of being portable. The GDIMM employs a 3-hole aperture mask and measures seeing in the same way. Another technique to note is the H-DIMM (Bally et al., 1996). The H-DIMM employs a Hartmann mask to utilise more of the telescope aperture with  $n$  subapertures, resulting in  $n(n - 1)$  baselines. As a result, instead of one measurement of the differential image motion, multiple measurements can be made, according to equation 3.2, for different baselines and combined to reduce the overall statistical uncertainty.

### 3.2.3 Advantages & Disadvantages of the DIMM

The main advantages of using the DIMM is that it is a low-cost small instrument that can provide a seeing measurement that is not biased by the effects of telescope shake, defocus and aberrations. However, strong scintillation will cause the DIMM to underestimate the seeing. The classical DIMM is not able to correct for this

given that it has no profiling capabilities. In addition, the DIMM is not able to directly estimate the noise present in each measurement of  $r_0$ , this means it is unable to make a measurement of  $r_0$  independent of those noise contributions. An instrument capable of this is SLODAR which will be described in section 3.4.

### 3.3 MASS

The MASS instrument is a turbulence profiler that measures the atmosphere in six layers by analysing the spatial intensity fluctuations measured at the ground (Tokovinin, 2007). The Fresnel radius (see equation 2.4) describes the spatial scale of the scintillation produced by turbulence at different altitudes. Figure 2.6 in section 2.2.2 provides a graphical demonstration of this. The MASS instrument employs a four ring aperture system to act as a spatial filter in order to establish scintillation originating from different altitudes. Each aperture is connected to a photomultiplier tube to detect the light of a single bright star (Tokovinin, 2007), as illustrated in figure 3.4. The scintillation index of each aperture,  $s_k^2$ , is defined as

$$\begin{aligned} s_k^2 &= \frac{\langle [I_k - \langle I_k \rangle]^2 \rangle}{\langle I_k \rangle^2}, \\ &= \frac{\langle \Delta I_k^2 \rangle}{\langle I_k \rangle^2}, \end{aligned} \quad (3.5)$$

where  $I_k$  is the light intensity received by one of the apertures  $k$ . Likewise, the differential scintillation index between two apertures can be found

$$s_{k_1 k_2}^2 = \left\langle \left( \frac{\Delta I_{k_1}}{\langle I_{k_1} \rangle} - \frac{\Delta I_{k_2}}{\langle I_{k_2} \rangle} \right)^2 \right\rangle. \quad (3.6)$$

This gives a total of ten scintillation indices (Tokovinin, 2007).

Turbulence profiles can be represented as a collection of independent layers. The ten scintillation indices measured by MASS are modelled as

$$s_k^2 = \int W_k(h) C_n^2(h) dh, \quad (3.7)$$

where  $W_k(h)$  is the weighting function for individual scintillation indices as a function of height,  $h$  (Tokovinin, 2007). Figure 3.5(a) illustrates a set of MASS weighting functions, i.e. the ratio of each index to the layer strength. Knowledge of the aperture geometry and spectral response is required to define the weighting functions. MASS models the atmosphere as a collection of six pre-defined heights, 0.5, 1, 2, 4, 8 and 16 km. The data analysis uses a least squares regression to find the strength of each layer from the measured indices. The MASS is not capable of sensing turbulence below 0.5 km. This is because it is difficult to distinguish weak scintillation in the presence of much stronger scintillation originating at high altitudes (Tokovinin, 2007).

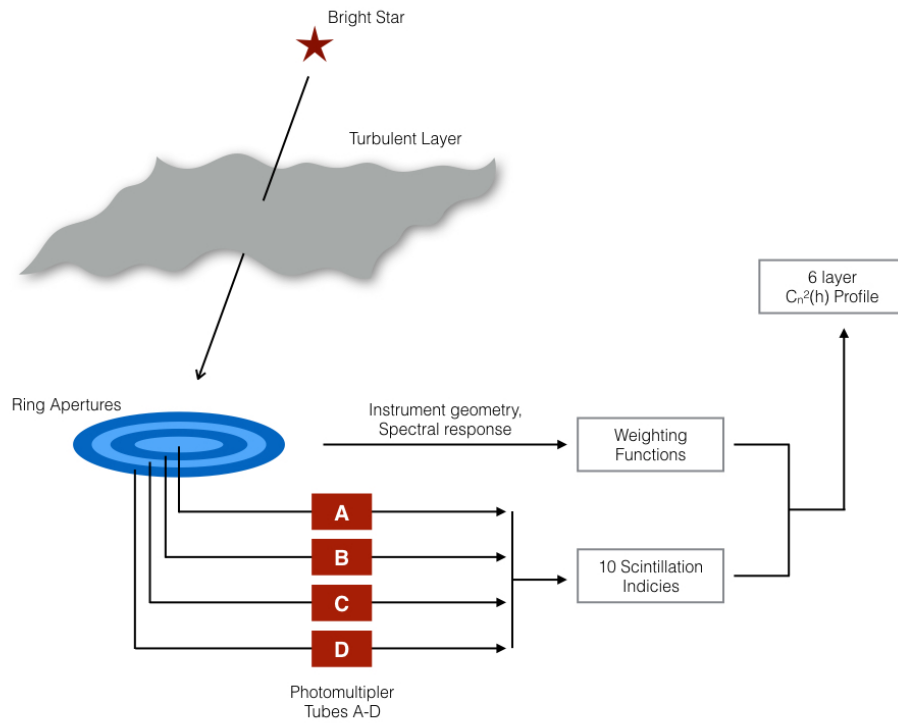


Figure 3.4: Illustration of the principles of MASS. Adapted from Tokovinin (2007).

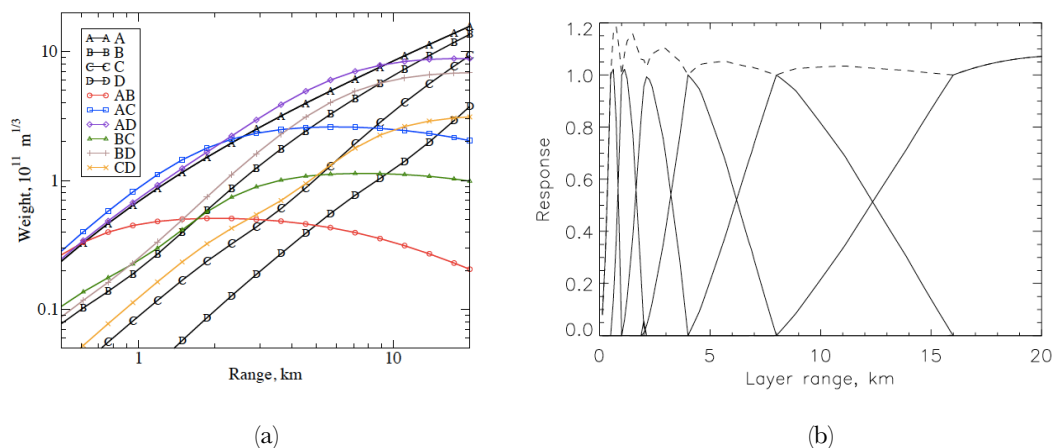


Figure 3.5: (a) Weighting functions for the ten scintillation indices of MASS. (b) Response of the fixed-layer restoration procedure to a single turbulence layer. The dashed line is the sum of the 6 fixed layers (block line). Taken from (Kornilov et al., 2003).

### 3.3.1 Accuracy and Precision

The accuracy of the MASS is described in detail in Tokovinin and Kornilov (2007) and Tokovinin (2007). Here they are described for completeness. The MASS does not rely on the absolute photon count but the fluctuations in the count. These measurements are integrated over timescales from  $T = 1$  minute. The relative error of the scintillation indices is determined by the statistics of the signal and is on the order of  $\sqrt{\tau/T}$ , where  $\tau$  is the characteristic time of signal fluctuations. In practice this error is  $\sim 2 - 3\%$

Since the MASS is not sensitive to turbulence below altitudes of 0.5 km it is expected that the measured seeing of the free atmosphere will always be better than the total integrated turbulence. However, this is not always the case. The MASS relies on weak-perturbation theory, and assumes weak scintillation. As a result, under strong scintillation the power at high frequencies increase and the MASS profile restoration software leads to an overestimation of the free atmosphere seeing as higher altitude turbulence is shifted to lower altitudes (Tokovinin and Kornilov,

2007). Overall this can result in a 10% error (Tokovinin, 2007). A correction is applied for the cases where the scintillation is between 0.1 – 0.7. Values greater than 0.7 means the scintillation is too strong to provide a good enough correction. For a fixed layer model the errors in layer strength are dependent on altitude, with smaller errors for higher altitudes. One reason, described above, is that lower altitude turbulence will produce weak scintillation. Another reason is displayed by the response functions in figure 3.5(b). These responses are for the fixed layer restoration procedure to a single turbulent layer. The dashed line is the sum of the six fixed layers. Ideally it should be at a constant value of one. However, at lower altitudes the sum between altitude bins are greater than one, meaning the instrument is likely to overestimate the turbulence strength at those altitudes.

It is worth noting that all MASS instruments vary slightly in performance, this can be due to individual detector characteristics. Comparisons between two MASS instruments can be found in Tokovinin (2007). They show a systematic difference in the profiles they obtain at the lower altitudes. For example, one MASS placed turbulence at 2 km where as the other MASS distributed the same amount of turbulence over 1 and 2 km.

### **3.3.2 MASS-DIMM**

The MASS and DIMM have been combined to create the MASS-DIMM instrument. Since the MASS permits measurements of the seeing above 0.5 km, and the DIMM measures the total integrated turbulence strength for the whole free atmosphere, the ground layer turbulence can be estimated by subtracting the turbulence integrals measured by the two instruments (Tokovinin and Kornilov, 2007).

As described in sections 3.2.1 and 3.3.1 there are a number of contributing sources for some of the inaccuracies present in the turbulence estimates generated by the DIMM and MASS. As a result, the combination of these two instruments will introduce errors regarding ground layer turbulence estimates. Under strong scin-

tillation the subtraction method used to estimate the ground layer turbulence will not work, since the DIMM and MASS over- and underestimate seeing in this regime. However, if a high proportion of the turbulence is located at the ground layer than this method can be used to reliably estimate the ground layer turbulence. In addition, the DIMM can over- or underestimate the seeing in the presence of turbulent layers with low and high wind speeds. This will also result in an over- or underestimation of the turbulence strength at the ground layer.

### 3.4 SLODAR

SLODAR is a vertical profiling technique that utilises a SHWFS to image a pair of stars of known angular separation. The altitude, strength and velocity of each turbulent layer can be estimated by employing the triangulation method. The maximum altitude ( $h_{max}$ ) and vertical resolution ( $\delta h$ ) are determined by the geometry of the system as depicted in figure 3.6. The value of  $h_{max}$  is given by,

$$h_{max} = \frac{D}{\theta}, \quad (3.8)$$

where  $D$  is the telescope aperture and  $\theta$  is the angular separation of the target stars. The vertical resolution is given by,

$$\delta h = \frac{D}{n\theta} \times \cos(Z), \quad (3.9)$$

where  $n$  is the number of subapertures subtended across the pupil and  $Z$  is the zenith angle of the observed target (Osborn et al., 2010; Osborn, 2010). Increasing the value of  $n$  will decrease  $\delta h$ . This is preferable since it would result in an increase in the resolution. However, a limiting factor to the value of  $n$  is the minimum subaperture size. The subaperture size needs to be sufficiently large to provide enough signal as well as to produce a diffraction limited spot width small enough to allow measurements of motions due to seeing.

The SLODAR technique has been based on a number of different telescopes aperture sizes. For example the SL-SLODAR can observe the atmosphere up to  $\sim 100$  m

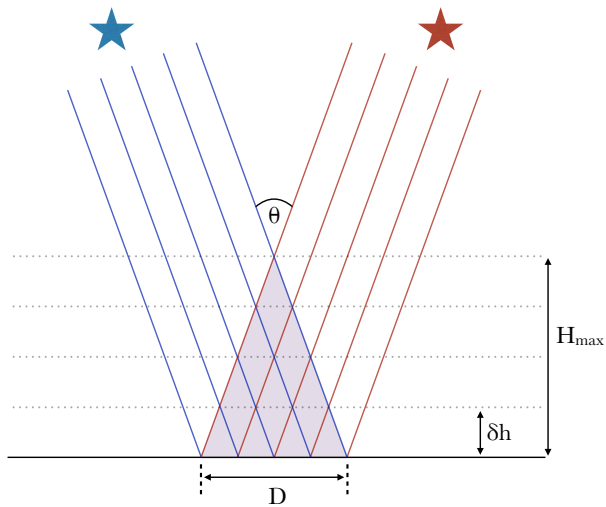


Figure 3.6: Illustration of SLODAR geometry, where  $\theta$  is the angular separation of the two target stars,  $h_{max}$  is the maximum altitude,  $\delta h$  is the altitude resolution and  $D$  is the diameter of the telescope aperture. Adapted from Osborn (2010).

altitude and  $\sim \delta h < 10$  m by employing a telescope aperture size of  $D = 0.5$  m and widely separated target stars (Osborn et al., 2010). The Generalised SLODAR was mounted on a 2.54 m telescope as part of a site-testing campaign for the Giant Magellan Telescope (GMT) (Goodwin et al., 2016). In addition, the SLODAR has been based on the 4.2 m William Herschel Telescope (WHT), La Palma, observing altitudes up to 17 km (Wilson, 2002).

SLODAR measures the spatial covariance of the gradient of the optical phase aberration observed at the ground for each target star path (Butterley et al., 2006). The turbulence profile can be recovered by fitting the measured cross-covariance functions with a set of impulse response functions for the system. These response functions describe the shape of the covariance for a thin layer at a given altitude under a von Karman turbulence model. This fit returns an estimate of the integrated turbulence strength of that altitude bin, of width according to equation 3.9.

### 3.4.1 Obtaining $r_0$

In this section, estimating  $r_0$  from SLODAR data will be discussed, since this method will be adopted by the Shack Hartmann Image Motion Monitor (SHIMM), as described in section 4.3. A detailed description of this technique can be found in Butterley et al. (2006). The SLODAR detector acquires images with an exposure time of  $\sim 2$  ms exposures, for a total time of approximately 30 seconds. The rough position of the focused spots in the images are found by Gaussian fitting to the mean of the data packet. The centroids of the spots, for individual frames, are then found by using a standard centre-of-mass algorithm. Telescope guiding errors and wind shake errors are removed by subtracting the mean of the centroids for each frame. As a result, common tip and tilt motions induced by the atmosphere are also removed. The response functions must be modified to take this into account (Butterley et al., 2006).

A 2-D spatial cross-covariance map is generated from the centroids for the two target stars, as shown by the example map in figure 3.7. A 1-D slice of the map is extracted, in the direction of the orientation of the stars on the focal plane (Osborn, 2010). The amplitude and position of peaks in this slice correspond to the strength and altitude of turbulent layers. For the example of a single layer at altitude  $h$ , a peak in the cross-covariance function will occur at a spatial offset of  $h\theta$ , as shown in figure 3.10 in section 3.5. However, the shape of this function does not give the turbulent profiles directly. Theoretical impulse response functions are fitted to the cross-covariance map to obtain the optical turbulence profile. This is done for both longitudinal and transverse centroid directions (Butterley et al., 2006). Figure 3.3 in section 3.2 illustrates how longitudinal and transverse directions are defined. Figure 3.8 shows example impulse response functions for longitudinal and transverse covariances. This fit can be applied to the whole 2-D map, however, most of the useful information is found in the 1-D slice.

The profile obtained via this method will extend only to altitude  $h_{max}$ . The total

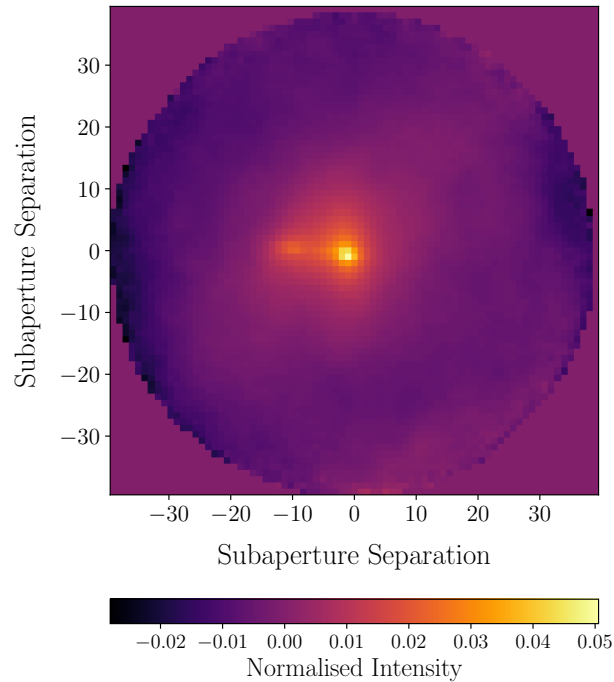


Figure 3.7: Example of a 2-D spatial cross-covariance map generated from the centroids of each target star observed by the SLODAR instrument. This data was obtained for the multi-wavefront sensor experiment on the Canadian France Hawaii Telescope, in December 2012. The map was provided courtesy of Timothy Butterley (Butterley et al., 2006).

turbulence strength in the ‘unsensed’ region above  $h_{max}$  can be found by subtracting the integrated turbulence strength of all the layers, of the measured turbulence profile, from the total integrated turbulence strength.

Accurate estimations of  $r_0$  for the whole atmosphere can be made by applying a fit to the auto-covariance of the centroids measured from the imaged spots for one WFS. This is done for both x and y centroids. The auto-covariance function used is a 1-D slice along the centre of the map. The effects of centroid measurement noise on the estimate of  $r_0$  can almost entirely be removed by excluding the central point of the auto-covariance function (i.e. the zero spatial offset, corresponding to the centroid variance). By applying this fit the zero offset value can be estimated

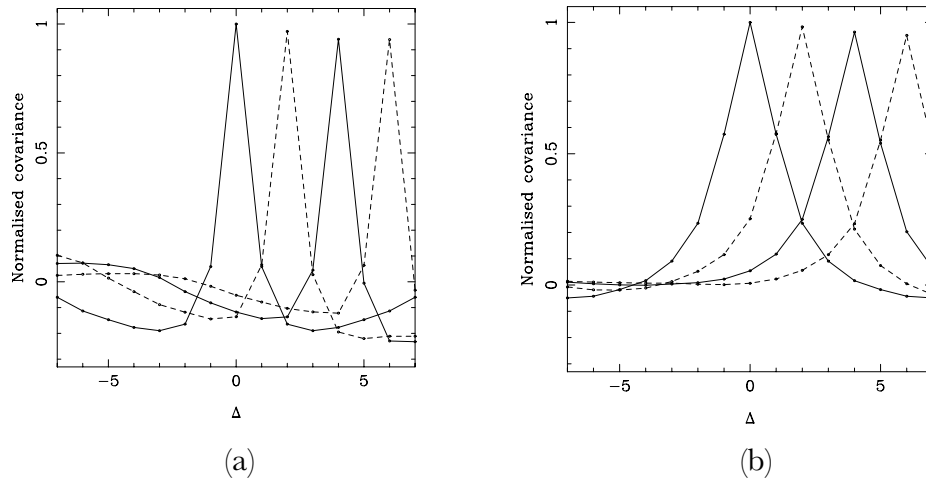


Figure 3.8: Example normalised SLODAR theoretical impulse response functions for longitudinal (a) and transverse (b) covariance, where  $\Delta$  is the subaperture separation of the 1-D slice. Taken from Butterley et al. (2006).

for when there is no noise contribution. The difference between this estimate of the zero offset value and the measured value provides an estimate of the overall centroid noise level. Figure 3.9 demonstrates this method for simulated results from Butterley et al. (2006). The broken line is the theoretical auto-covariance fit when the central point (zero spatial offset) is excluded. This indicates a fit for the zero noise case. The specifics of this method will be discussed in more detail in chapter 4.

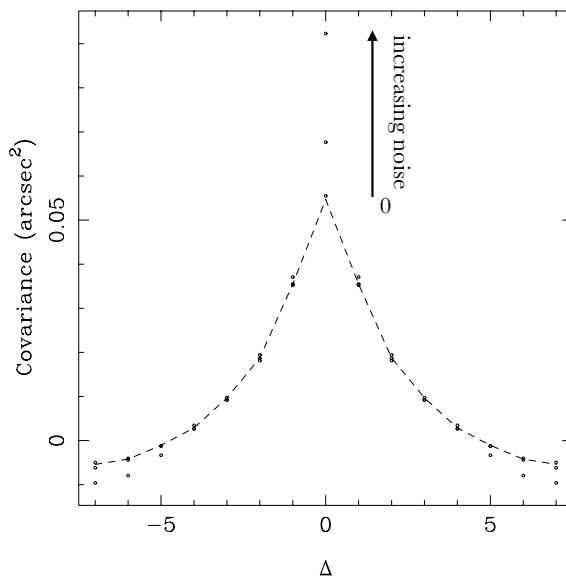


Figure 3.9: Example of simulated data, demonstrating the method for estimating noise contributions to the centroid variance, where  $\Delta$  is the subaperture separation of the 1-D slice. Edited from Butterley et al. (2006).

### 3.5 SCIDAR

SCIDAR, like SLODAR, utilises an optical triangulation technique. A telescope pupil image resulting from observing two stars is formed onto a detector. The turbulence profile is estimated from the correlation of the scintillation pattern produced by each star (Vernin and Roddier, 1973) as illustrated by figure 3.10(a). For a turbulent layer at altitude  $h$ , two copies of the same wavefront aberration will be detected on the ground separated by a distance,  $h\theta$ , where  $\theta$  is the angular separation of the two target stars. This results in a peak in the time averaged spatial covariance of the image, at a separation corresponding to this distance. The amplitude of the correlation peak relates to the turbulence strength at  $h$ . Wind velocity can be found from the temporal cross-covariance map. When there is no temporal offset, peaks corresponding to turbulent layers at different altitudes are

formed on the cross-covariance map. As the temporal offset increases these peaks move across the map. This movement indicates the speed and direction that the turbulent layer is traversing the telescope aperture.

Telescope pupil images for each target star are projected onto the same CCD, and overlap with an offset which is dependent on the angular separation of the targets. Each turbulent layer will then contribute three peaks to the auto-covariance function. This is due to the intensity pattern from each star correlating with the intensity pattern of itself and the other star (Shepherd et al., 2013), as shown in figure 3.10(b).

The theoretical vertical resolution for SCIDAR is dependent on the Fresnel radius size (equation 2.4) for a given altitude

$$\delta h(z) = 0.78 \frac{\sqrt{\lambda z}}{\theta}, \quad (3.10)$$

where  $z = |h - h_{conj}|$  and  $h_{conj}$  is the conjugate altitude of the detector (Prieur, J.-L. et al., 2001; Shepherd et al., 2013). The resolution that can be obtained by the SCIDAR instrument is higher than that of SLODAR. This is because the spatial scale of the scintillation is smaller than the minimum subaperture separation, allowing for higher altitude resolution (Shepherd et al., 2013). Increasing  $\theta$  will increase the altitude resolution, however it will reduce the maximum profiling altitude. This maximum altitude, at the zenith, is defined as

$$h_{max} = \frac{(D - \sqrt{\lambda h_{conj}})}{\theta}. \quad (3.11)$$

For a target that is not at the zenith, this equation must be modified to calculate the correct altitude. As described in section 2.1 the tropopause contains 80% of the atmospheric mass. Therefore,  $h_{max}$  is selected to be approximately 20 km, since it is higher than the maximum altitude of the tropopause. This dictates the minimum telescope aperture size required for a given value of  $\theta$ . This means, for example, if the conjugate altitude of the detector is zero,  $\theta$  is  $\sim 10$  arcsec and  $h_{max} = 20$  km, a minimum telescope aperture of approximately 1 m is required.

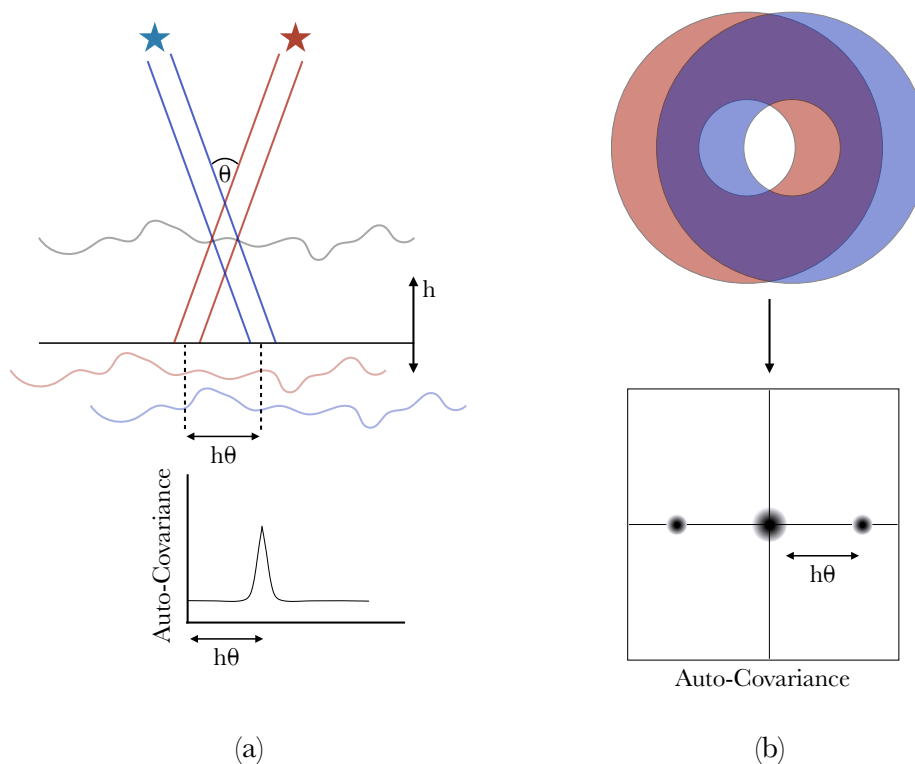


Figure 3.10: (a) Illustration of how two copies of the same wavefront aberration at altitude,  $h$ , will be detected on the ground at a distance  $h\theta$ , where  $\theta$  is the angular separation. (b) The auto-covariance function generated from an overlapped pupil pattern image. Adapted from Shepherd et al. (2013).

When the pupil patterns for the two target stars superpose, it results in a lack of contrast in the combined pupil image. This leads to a loss of information. Variations on the SCIDAR have been made to avoid this. One is LOLAS. This method was based on a 40 cm telescope, designed for widely separated double star targets. As a result, the pupil patterns of each star are completely separated on the detector. However, this limits  $h_{max}$  to low layers of up to approximately 1 km (Avila et al., 2008). Another variation is the Stereo-SCIntillation Detection And Ranging (Stereo-SCIDAR). Stereo-SCIDAR employs separate EMCCD detectors for each star, instead of a single detector (Shepherd et al., 2013). In the cross-covariance of two separated scintillation patterns, each turbulent layer produces

only one peak, as opposed to the three peaks shown in figure 3.10. The signal-to-noise ratio (SNR) is improved by a factor of at least 2, and the measurement of wind velocities by peak tracking is greatly simplified.

The Stereo-SCIDAR technique provides the most detailed optical turbulence profile of the full atmosphere to date, with information on the strength and wind velocity of each turbulent layer. However, as described above, it requires a telescope size greater than 1 m, which makes it the most expensive of the commonly used optical turbulence profiling techniques.

### 3.6 Conclusion

In this chapter four key optical turbulence profilers and seeing monitors, the DIMM, MASS, SLODAR and SCIDAR, were discussed. Some of these instruments have been modified and combined to create different profilers for specific profiling requirements. These particular four profilers have been discussed since they will all be referred to in the proceeding chapters of this thesis.

The pros and cons of each instrument were described. It is clear that there is an overall compromise between cost, precision and accuracy. For example the DIMM is a small economical instrument, however it can only provide a value for the total integrated seeing. In addition, the accuracy of the measurement diminishes under strong scintillation and is biased by noise. The MASS is also a small economical instrument that can provide a coarse six layer turbulence and wind profile, but is insensitive to the ground and also suffers under strong scintillation conditions. Whereas the SLODAR and SCIDAR instruments can produce detailed turbulence and wind profiles. However due to the size requirements of the telescopes to produce a full turbulence profile, they are the most expensive of the profilers.

Table 3.1 summarises the key optical turbulence profilers detailed in this chapter, as well as the SHIMM and FASS that will be described in Chapters 4 and 6.

Features	Profiling Instruments					
	DIMM	SHIMM <sup>a</sup>	MASS	FASS <sup>b</sup>	SLODAR	SCIDAR
Parameters Measured	$r_0$	$r_0, \tau_0, \text{Cn}^2(\text{h})$ profile	$\text{Cn}^2(\text{h})$ & Velocity profile	$\text{Cn}^2(\text{h})$ & Velocity profile (TBC)	$r_0, \tau_0, \theta_0, \text{Cn}^2(\text{h})$ & Velocity profile	$r_0, \tau_0, \theta_0, \text{Cn}^2(\text{h})$ & Velocity profile
Profile Resolution	N/A	3 layers	6 layers (log)	$\sim 11$ layers	$\frac{D}{\pi \theta}$ $\times \cos(\theta_z)$	$0.78 \frac{\sqrt{\lambda z}}{\theta}$
Target Star	Single	Single	Single	Single	Double	Double
Telescope Diameter	$\sim 12\text{-}14$ inches	$> 9$ inches	$\sim 3\text{-}5$ inches	$\geq 9$ inches	$\geq 0.5$ m	$> 1$ m
Typical Detector	CCD	CCD	Four PMTs	EMCCD	EMCCD	EMCCD
Portable	Yes	Yes	Yes	Yes	Possible	No
Approx. Cost (£) <sup>c</sup>	10 k	$< 10$ k	10 k	10 k	100 k	200 k

Table 3.1: Comparisons of different turbulence profilers.

<sup>a</sup>Described in Chapter 4.<sup>b</sup>Described in Chapter 6.<sup>c</sup>This cost estimation does not include the cost of the dome and the infrastructure to operate the instruments.

---

# SHIMM

In this chapter the development and testing of the SHIMM instrument, pictured in figure 4.1, will be discussed. This instrument was developed to serve as a low-cost, compact, portable seeing monitor, that could be easily and inexpensively duplicated, making it ideal for comparisons of atmospheric conditions around a large observing site. In addition, the SHIMM has the capability to estimate the value of  $\tau_0$ , as well as a low resolution (three fitted turbulent layers) estimate of the optical turbulence profile. The effects of scintillation on the estimate of  $r_0$  can then also be corrected. These additional capabilities will be discussed in chapters 5 and 6.

The SHIMM is a variation on the DIMM design, made by employing a SHWFS instead of an aperture mask. Compared to the traditional DIMM the SHIMM utilises more of the telescope aperture, resulting in more focused spots. Exploiting more of the telescope aperture reduces both the shot noise and the statistical noise for seeing measurements, since a larger number of subapertures are used.

As mentioned in section 3.2, the H-DIMM also utilises more of the aperture by employing a Hartmann mask. However, unlike the SHIMM the H-DIMM and DIMM estimate seeing by relating the variance of the differential image motion, obtained from pairs of subapertures, to  $r_0$  (Bally et al., 1996). The SHIMM adopts the SLODAR method of analysis, which provides an estimate of  $r_0$  independent of noise.

In this chapter the SHIMM instrument and the seeing estimation method will be described. Results from two identical SHIMM seeing monitors will be presented, as well as a comparison with simultaneous optical turbulence profiles recorded with Stereo-SCIDAR on the Isaac Newton Telescope (INT) in La Palma.



Figure 4.1: The SHIMM (with additional FASS optics) at Cerro Paranal, Chile, at the site of the VLT.

## 4.1 System Design & Hardware Configuration

### 4.1.1 Design Considerations

The SHIMM instrument as a whole, shown in figure 4.1, is comprised of a telescope, WFS optics, a detector and a control computer running custom software for real time analysis and autoguiding of the telescope. Since the instrument was built with the intention of being low-cost, compact and portable, there were a number

of limiting factors to be considered for the design. In order to remain low-cost the design of the SHIMM was limited to the use of off-the-shelf components, as listed in table 4.1.2. Here, the main hardware components will be discussed.

### **Telescope**

In order to be a portable instrument the SHIMM needed to be easily disassembled and relocated. This limited the maximum weight of the telescope and hence the telescope aperture size that could be used. However, the telescope aperture must be sufficiently large to permit WFS measurements. Two different telescope aperture sizes of 9.25 and 11 inches have been used in this investigation, and are referred to as the C9-SHIMM and C11-SHIMM respectively.

### **WFS optics**

The SHIMM employs a lenslet array in order to map square subapertures onto the aperture of the telescope. It is preferable to have as many subapertures as possible to make full use of the telescope aperture and to reduce statistical noise. However, large enough subapertures are required to provide a sufficient signal as well as a diffraction limited spot width which is sufficiently small to permit the measurement of motions due to seeing. The spots must be at least Nyquist sampled by the detector, i.e. there must be at least 2 detected pixels across the FWHM of the spot. The parameters of the WFS were determined by this required sampling of the telescope aperture.

Figure 4.2 illustrates a schematic of the WFS optical design. The following illustrates the optical design considerations required for determining the specifications of the WFS optics.

The pre-defined parameters are: the format of the CCD; the CCD pixel size  $d_{pix}$ ; the telescope aperture  $D$  and f-number  $f/\#$ ; and the desired number of a subapertures  $n$ , to span the length of the telescope aperture.

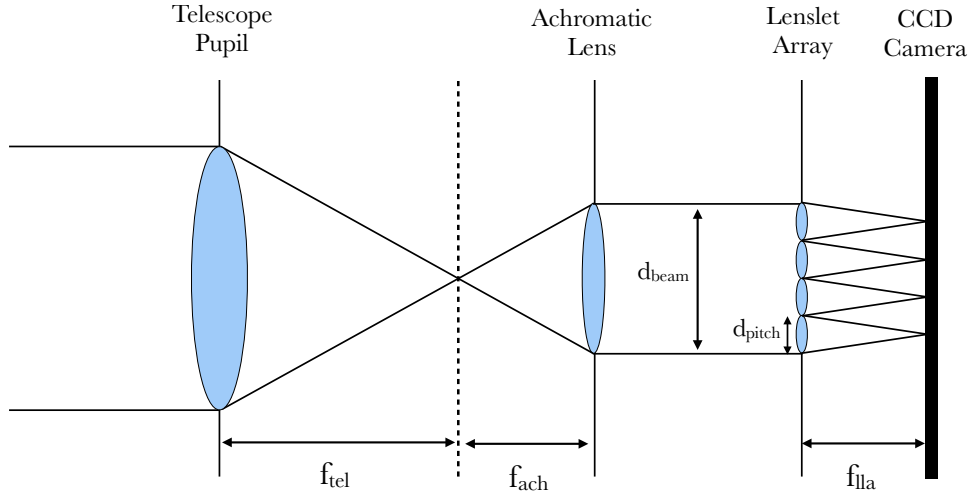


Figure 4.2: Schematic of the SHIMM optics. Light from the telescope is focused at  $f_{telescope}$ . The achromatic lens collimates the light into the lenslet array which focuses the light on to the CCD at  $f_{lenslet}$ .

In order to obtain the right image scale and number of projected subapertures, the correct combination of the collimating achromat focal length  $f_{ach}$ , and the Shack Hartmann (SH) lenslet array focal length  $f_{lla}$ , and pitch width  $d_{pitch}$ , must be determined. Since these components are off-the-shelf there are limited options available.

**Lenslet Array Focal length ( $f_{lla}$ ):** The ratio of the focal lengths of the achromatic lens and the lenslet array determine the magnification of the pixel scale depending on the telescope specifications.

**Collimating Achromat Focal length ( $f_{ach}$ ):** The required focal length of the collimating lens is dependent on  $f/\#$  and the width of the collimated beam  $d_{beam}$ ,

$$f_{ach} = f/\# \times d_{beam}, \quad (4.1)$$

where  $d_{beam}$  is defined as

$$d_{beam} = n \times d_{pitch}. \quad (4.2)$$

Given that there are limited combinations for  $f_{ach}$ ,  $f_{lla}$  and  $d_{pitch}$ , the combination is optimised to acquire the desired value of  $n$  and largest sampling of the CCD. For example, if  $n = 6$ ,  $d_{pitch} = 0.5$  mm and the telescope used had an f-number  $f/\# = 10$ , then the value of  $f_{ach}$  will be 30 mm.

### CCD Considerations

**Frame Rate:** The frame rate for image acquisition was limited by the CCD's maximum frame rate capabilities. A fast frame rate (a minimum of a few tens of Hz) is required in order to obtain a useful number of atmospheric samples, typically 1000, over 1 - 5 minutes. This provides a large number of independent samples, which reduces the statistical noise. Figure 4.18 in section 4.5 illustrates, in simulation, how the measurement of  $r_0$  converges on the timescale of 3 - 5 minutes. Timescales longer than this can not be used since the seeing conditions will evolve during a single dataset.

**Exposure Time:** When acquiring data by the SHIMM instantaneous imaging, i.e. zero exposure time, would be the ideal case, so that the motion of the spot is frozen in each exposure. Finite exposure times result in an overestimation of  $r_0$  since it reduces the measured differential image motion. This is described in 3.2.1 and graphically demonstrated by figure 2.3 which illustrates the effects that increasing exposure time has on an imaged spot. Figure 4.3(a) shows these effects on the measurement of  $r_0$ , of different values, for a typical wind speed of 10 m/s (see section 4.2.1 for a discussion of the typical wind speed value). The method for estimating  $r_0$  is demonstrated in section 4.3.1. Figure 4.3(b) illustrates that whilst the percentage difference between the expected and measured  $r_0$  increases for smaller  $r_0$  values, this effect is only slight. The error bars represent statistical errors of  $1/\sqrt{N}$ , where  $N$  is the number of iterations of the simulation, i.e. the number of independent samples contributing to the measurement of  $r_0$ .

Under these conditions it is clear that a shorter exposure time is preferable, how-

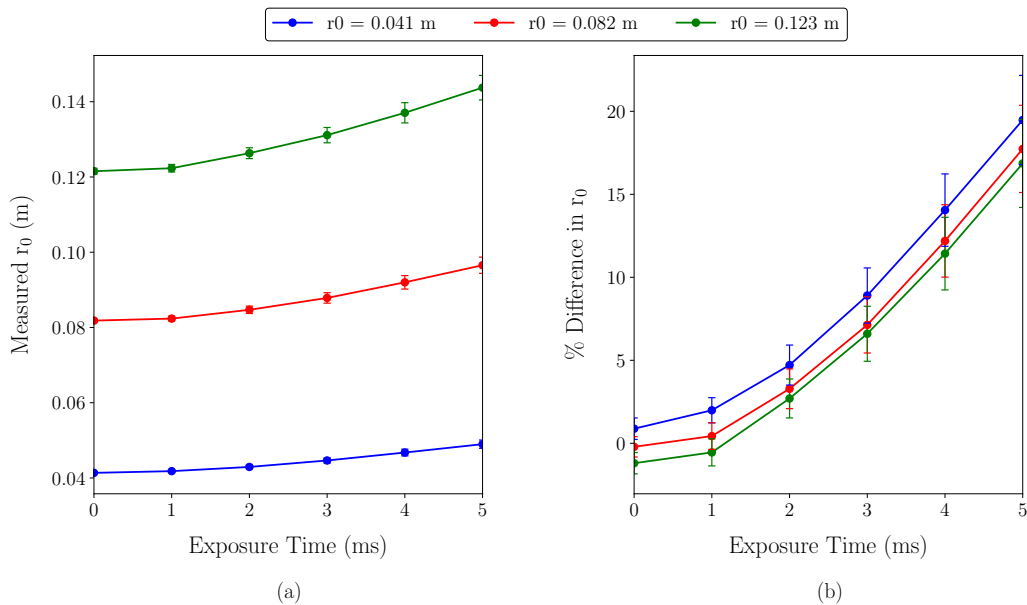


Figure 4.3: Simulated results showing the measured  $r_0$  value versus exposure time for a set wind speed of 10 m/s where (a) shows the increase in exposure time results in an increase in measured  $r_0$  and (b) shows that percentage difference in the measured and expected  $r_0$ . It appears that whilst the percentage difference increases with smaller  $r_0$ , this effect is only slight.

ever practically there is a trade off between short exposure times and collecting sufficient light on the detector. In traditional DIMM instruments, exposure times of 5 - 20 ms have been used (Tokovinin and Kornilov, 2007). An exposure time of 2 ms was chosen for the SHIMM since simulations showed that there is less than 5% error in the measured  $r_0$  value, due to the effects of wind smearing, for typical atmospheric wind speeds of 10 m/s. Using this exposure time, as opposed to a shorter time, allows for an increase in the number of target stars that can be used. Each turbulent layer in the atmosphere will have an associated wind speed. Data taken by the Stereo-SCIDAR instrument (Shepherd et al., 2013) mounted on the INT in La Palma and on the Auxillary Telescope (AT) in Paranal observing sites indicate that the median wind speed of layers (over all altitudes) is approximately 10.7 m/s and 13.1 m/s respectively.

It is important to note that as the wind speed increases so does the overestimation

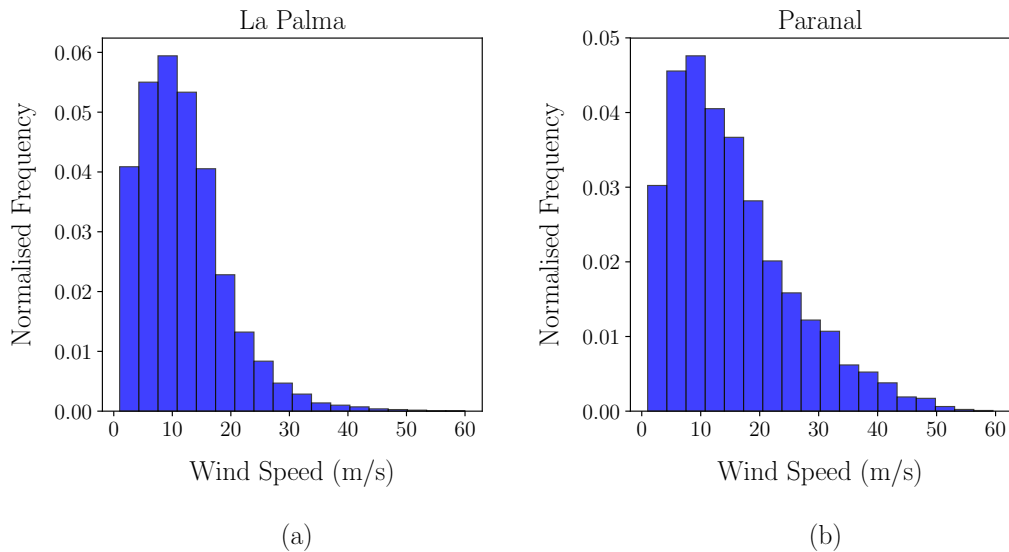


Figure 4.4: Histogram of all wind speeds measured by Stereo-SCIDAR at two different observing sites mounted on the INT in La Palma (a) and onto AT at Paranal (b), over a range of nights.

of the  $r_0$  value, as illustrated in figure 4.5. The figure displays results for a range of wind speeds of increasing exposure time, for an expected  $r_0$  of 0.041 m. Although this is under very strong turbulent conditions the conclusion does not change with  $r_0$ . This figure also illustrates the need for a short exposure time. The error bars represent statistical errors of a factor of  $1/\sqrt{N}$ , where  $N$  is the number of repetitions of the simulation. Through further simulation it was found that for a measurement with 2 ms exposure time,  $r_0 \gtrsim 0.05$  m can be measured within 10% accuracy for wind speeds up to  $20 \text{ ms}^{-1}$ .

**Region of interest:** For the prototype it was desirable to save all raw images for later reprocessing, therefore memory size was an important factor. In order to reduce the memory size of the data packets, it was important not to save images with ‘unused’ regions. Therefore, a region of interest was set to reduce the size of a single data packet. During data acquisition, of a timescale of a few minutes, it is possible for the spot pattern to drift along the CCD. This is a result of the inaccuracies of the tracking of the telescope mount. Therefore, it is important

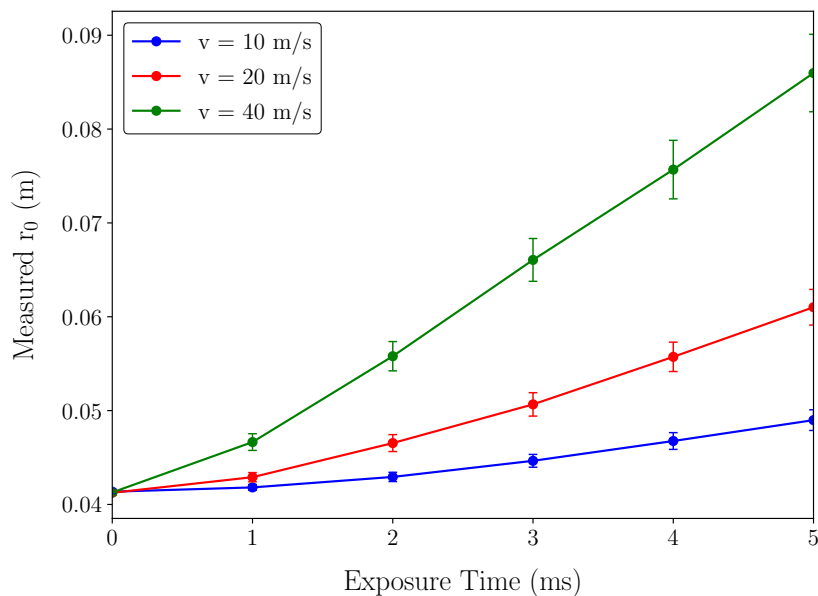


Figure 4.5: Simulated results for turbulent layer of  $r_0 = 0.041$  m with 0 – 5 ms exposure time for wind speeds of 10 m/s (blue), 20 m/s (red) and 40 m/s (green).

that the region of interest is large enough to allow for these small drifts between autoguiding checks.

**Data Acquisition Duration:** Approximately 1 to 5 minutes of data acquisition is desired. Data acquisition for two minutes would provide 3600 independent samples, for a CCD frame rate of 30 Hz. This provides a sufficient number of independent samples to reduce the statistical error to less than 2%. However, on longer times scales the value of  $r_0$  will change substantially, as the seeing conditions evolve. In addition, the frequency of the autoguiding updates would not allow data acquisition for longer than a few minutes.

#### 4.1.2 Hardware

Two hardware configurations, based on a 9.25 inch and 11 inch Celestron telescope, here named C9-SHIMM and C11-SHIMM respectively have been used in this investigation. As well as employing a larger telescope aperture, the C11-SHIMM

utilises a camera with a faster frame rate, to permit measurement of  $\tau_0$ . The composition and differences of these prototypes are described in table 4.1.2. The principle of both instruments are the same, however only the C9-SHIMM will be the focus of this chapter. The C11-SHIMM will be discussed further in chapter 5.

Both SHIMM models employ the same WFS optics, shown in figure 4.6. Light gathered from the telescope is collimated by an achromatic lens and then focused onto the CCD detector by a lenslet array. In order to orient the focused spot pattern with respect to the CCD, a rotation stage was used. To ensure the light fell across the correct subapertures to produce the desired spot pattern, a translation stage was employed to allow the lenslet array to be moved in the x and y direction relative to the beam. In the correct alignment the aperture of the telescope is mapped onto the lenslet array producing a pattern of fully illuminated subapertures depicted in figure 4.7(a). Figure 4.7(a) shows that there are additional partially illuminated subapertures. Partial illumination causes vignetting of the spots, this reduces the amount of light that is collected and causes an extended image instead of a focused spot. As a result, these spots were not used in the data analysis procedure.

Each subaperture has a projected subaperture width of  $d = 4.1$  cm. This is much smaller than the typical DIMM subaperture size of 10 cm (Tokovinin, 2002). This small aperture size can be problematic since it reduces the amount of light that can be collected, and therefore reduces the number of target stars that can be observed. In addition, this subaperture size is smaller than the typical value of  $r_0$  which tends to vary between 5 – 20 cm. However, simulations for this configuration, observing a bright target star, show that  $r_0$  can be measured accurately, as will be shown in section 4.2. The effects of scintillation on the measurement of  $r_0$  will be greater for smaller subapertures, however this will be corrected for, as will be described in chapter 6. Figure 4.7(b) shows the WFS image, from an on-sky target star, formed on the CCD.

Features	C9-SHIMM	C11-SHIMM
<b>Telescope</b>		
Model:	Celestron CGEM 9.25 inch f/10 Schmidt Cassagrain	Celestron CGEM 11 inch f/10 Schmidt Cassagrain
Mount:	VX Mount	VX Mount
<b>WFS Optics</b>	Pictured in figure 4.6	
Collimator:	Edmund Optics achromat lens with focal length of 30 mm	
Lenslet Array:	Edmund Optics lenslet array with pitch of 0.5 mm and focal length of 15.3 mm	
Lens Cage:	Thor Labs lens mounts and translation and rotation stages	
<b>Detector</b>		
Model:	1288 x 728 Mono Point Grey 092SM-CS Blackfly GigE camera	640 x 480 Mono Prosillica GE 680
Lens Mount:	CS-Mount	CS-Mount
Pixel Size:	4.08 $\mu\text{m}$	7.40 $\mu\text{m}$
Frame Rate:	30 Hz	200 Hz
ROI:	728 x 728	480 x 480
Exposure Time:	2 ms	2 ms
Image Scale:	0.71 arcsec/pixel	1.07 arcsec/pixel
<b>PC:</b>		
Hardware:	ITX mini PC	Mini PC Intel Nuc
OS:	Ubuntu 12.0	Ubuntu 12.0
<b>Subapertures</b>		
Size:	4.1 $\text{cm}^2$	4.7 $\text{cm}^2$
# used:	12	20
Autoguiding	RS232 controlled relay board	

Table 4.1: Lists the key components of two SHIMM models C9 and C11.

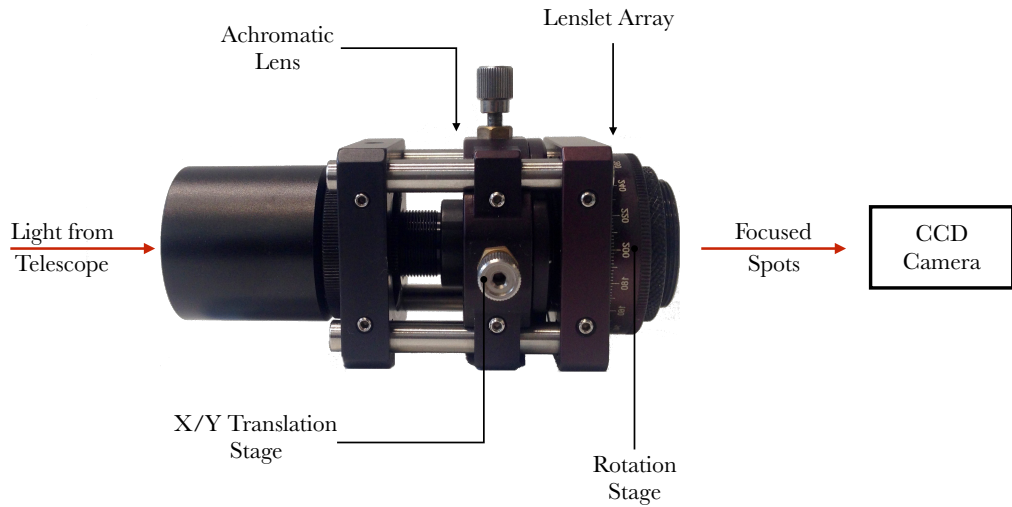


Figure 4.6: Image of the SHIMM WFS optics, comprised of an achromatic lens and lenslet array. The orientation of the spot pattern imaged onto the CCD can be altered with the rotation mount. To ensure the correct spot pattern is illuminated there are x/y translation stages to adjust the position of the lenslet array.

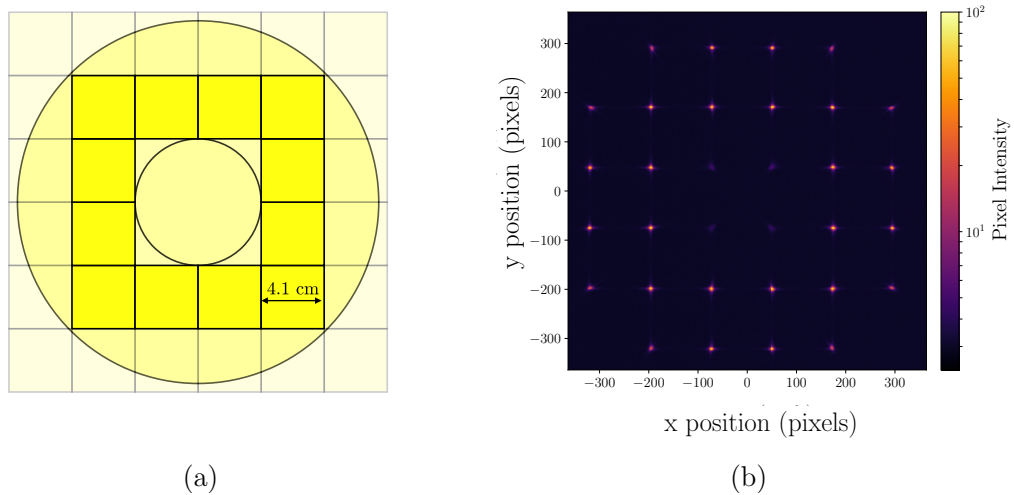


Figure 4.7: (a) Illustrates 12 fully illuminated square subapertures of the WFS mapped onto the C9-SHIMM telescope aperture. The outer and inner circle indicates the primary and secondary mirror. (b) Shows the resulting spot pattern formed on the CCD. A log scale has been used to present the image, in order to highlight the contrast between the background and the spot pattern.

For small telescopes wind shake can be a problem. Although small telescope guiding and wind shake errors are subtracted in the analysis, high wind speeds can result in smearing of the spots in a single exposure and in some cases cause the spots to move off the CCD in one or more frames. This renders the data unusable. To reduce the effects of high speed local winds a wind break was used. The portable wind break enclosure was designed and used to protect the telescope without obstructing its field of view. This was comprised of retractable tarpaulin curtains on a metal frame, as shown in figure 4.8. This was set up at the beginning of the observing run, and could be left assembled during the day.



Figure 4.8: Retractable windbreaks on the roof of the INT.

### 4.1.3 Software Requirements

Software for data acquisition, telescope autoguiding and real time on-sky data analysis was developed and operated on a compact ITX mini PC running Ubuntu 12.0 linux OS.

For data acquisition from the CCD a python wrapper was used around C++ software developed from the FlyCapture SDK, provided by the CCD manufactures. Software was developed to check the telescope focus, as will be discussed in detail, in section 4.2.1.

The tracking of the telescope mount was not accurate enough to ensure the target remained centred on the CCD for more than a few minutes. Therefore, autoguiding offsets were calculated from the position of the spot array and corrections were applied via the autoguider port of the telescope mount, see section 4.2.3.

Real time on-sky data required software to be developed to check the quality of the data and then to calculate  $r_0$ . This will be described in detail in section 4.3.

## 4.2 Observing Procedure

The observing procedure can be broken down into three main stages; setup and alignment, target acquisition and data acquisition.

### 4.2.1 Setup & Alignment

**Polar Alignment:** Since the SHIMM is portable, and therefore does not have a permanent dome to protect it from daylight and possible rain, it was assembled at the beginning of every night before sunset and stored in doors at the end of the night. As a result, the instrument needed to be polar aligned at the beginning of each night.

**Telescope Focus:** Accurate focusing of the telescope was required in order to minimise the FWHM of the spots, and therefore maximise the SNR of centroid measurements. The separation of the spots is sensitive to the telescope focus. Therefore, software was written to measure the spot separation. For the correct telescope focus the collimated lens produces a parallel beam. The required spot separation in pixels is then derived by dividing the pitch width of the lenslet by the CCD pixel size. The on-sky spot separation was measured by acquiring a dataset and finding the mean spot positions. The telescope focus was adjusted until the spot separation was close to the nominal value.

**Image Scale:** To allow for uncertainties in the nominal focal lengths of the optical components the image scale was confirmed by imaging a double star with known separation. The percentage error of the on-sky image scale was estimated to be 0.6%. Since long exposure images were taken the imaged spots were considered to be a Gaussian, therefore the location of the maximum could be found to precision +/- 0.5 pixel. A 0.6% error in image scale will lead to  $\sim 0.5\%$  error in the measurement of  $r_0$ . The measurement of the image scale was not done every night, but only if the hardware configuration was changed.

## 4.2.2 Target Acquisition

When using the C9-SHIMM, targets of second magnitude and brighter were required. An investigation of the limiting magnitude of the target star will be described in section 4.5.1. During observations a suitable target star was always available at a zenith less than  $30^\circ$ . To roughly estimate the availability of second magnitude, or brighter, stars at La Palma and Paranal, second magnitude stars at zenith angles less than  $30^\circ$  were cross-checked between 20:00h to 06:00h UTC for the whole year. It was found that there was approximately 85% and 95% observing time coverage for La Palma and Paranal respectively. By increasing the zenith angle to  $35^\circ$  and extending the target star magnitude to  $V = 2.05$  this would allow for 100% observing time coverage.

### 4.2.3 Data Acquisition

Software was developed to acquire datasets of defined frame rate, exposure time, acquisition duration, gain and region of interest. Image data packets of duration ten seconds were recorded at the maximum camera frame rate of 30 Hz with 2 ms exposure time, producing data cubes of 300 frames.

Autoguiding was implemented by interspersing image checks between multiple data acquisition packets, every two minutes. Autoguiding offsets to the telescope were calculated from the measured position of the WFS images and communicated to the autoguider port of the telescope via an RS232 controlled relay board. The position of the centre of the spot pattern was found by cross-correlating the image with a theoretical spot pattern mask. The position was required to be in a pre-defined region, such that the full spot pattern would remain on the CCD whilst acquiring data, i.e. before the next autoguiding image check.

Software for real time estimations of  $r_0$  was developed to monitor the atmospheric changes whilst on-sky. The software would acquire datasets every two minutes, run the analysis (described in the next section) and display the results.

## 4.3 Data Reduction

Here the post data acquisition process will be described, as well as the method for estimating  $r_0$ .

### 4.3.1 Data Processing

**Data quality control:** Once the image data was acquired a sequence of software checks were performed to validate the images before analysis.

- First the data was checked for saturated pixels. Strong scintillation can cause spots to be briefly saturated, even though the mean flux level is satisfactory.

If only small number of frames had saturated pixels, then these frames were discarded from the dataset. However, if more than 10% of frames had saturated pixels the packet was not used. This removed  $< 0.5\%$  of data, this will therefore not bias the results. This situation also occurred if the gain level was set to too high a value.

- The next stage was to locate the spot pattern on the CCD image. The location of the centre of the spot pattern was found by cross-correlating the image with a theoretical spot pattern mask. Due to telescope shake and small telescope drifts the spot pattern may not remain in the same place for each frame in a data packet. Therefore, the frames were averaged over the data packet to acquire the mean position. This mean position must be in a predefined region to ensure the full spot pattern is on the CCD region of interest.

**Centroiding:** Once the checks were passed and the data was considered usable, the CCD bias level was subtracted from the images. The CCD bias level was determined by acquiring a series of images with the minimum exposure time and no flux. These images are averaged to find the average bias of each individual pixel. This was then subtracted from each data image. Following this the centroids were determined for each spot in each frame of the dataset. A sub-region of pixels was defined for each spot to reduce analysis time. An intensity threshold was applied so that values below a threshold constant multiplied by the peak intensity was set to zero. This was done to reduce the influence of readout noise. After applying a threshold the centroid position was found by using the standard centre-of-mass equation. Another reason for thresholding is addressed in Tokovinin (2002). Centre-of-mass equations work well for diffraction limited images. However, for an aberrated image the central position corresponds to the location where the root mean squared residual aberration is minimal. It was found that thresholding better locates this position than centroiding alone (Tokovinin, 2002).

Another method for centroiding which is employed by the DIMM is to apply an intensity threshold and subtract this value from the entire sub-region of the subaperture image (Tokovinin, 2002). Everything below zero is then set to zero. These two methods were compared. Figure 4.9 illustrates these results for the SHIMM and DIMM method, for a range of threshold constants and  $r_0$  values, specific to the C9-SHIMM configuration. It can be seen that both methods will correctly estimate  $r_0$  but for different threshold constants. These results were obtained from noise free simulations. Alternative centroiding methods, such as the (iterative) weighted centre-of-gravity (Baker and Moallem, 2007) or the brightest pixel selection algorithm (Basden et al., 2012), could be explored to overcome the limitations of noise, thereby increasing the accuracy of centroiding for fainter stars.

**Subtracting Common Motion:** Common spot motions due to wind shake and telescope guiding errors were removed by subtracting the mean of the centroids for each frame. As a result, common tip-tilt motions induced by the atmosphere are also removed. This must be taken into account in the analysis to derive  $r_0$  and is discussed in section 4.4.

The mean centroid for each subaperture over the length of the dataset was then subtracted for the respective subaperture, in order to remove any static aberrations caused by the optics. The mean centroid averaged over many seconds is expected to be zero for spot motions due to atmospheric turbulence.

**Calculate Auto-Covariance:** Finally the spatial auto-covariance of the x and y centroids were calculated separately as

$$A_{\delta i, \delta j} = \langle C_{i,j} C'_{i',j'} \rangle, \quad (4.3)$$

where  $C$  and  $C'$  are the centroids at subaperture position  $[i, j]$  and  $[i', j']$  respectively. The spatial offset between the subapertures, in units of the subaperture diameter, are given as  $\delta i$  and  $\delta j$ . By calculating this for every possible separation a covariance map can be created. Figure 4.10 illustrates example covariance maps

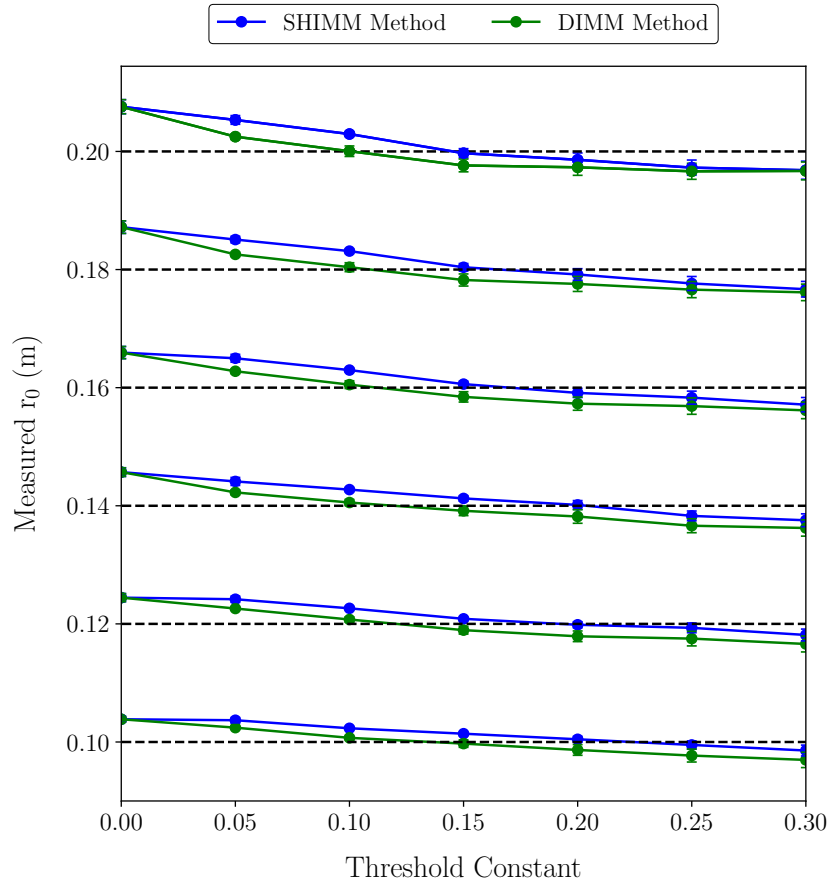


Figure 4.9: Results comparing the SHIMM (blue) and DIMM (green) centroiding method, for a range of  $r_0$  values and threshold constants. The dashed black line indicates the input  $r_0$  value for each pair of results.

for x and y centroids for a simulated dataset, in units of  $\text{pixel}^2$ . It was expected that the covariance map generated from the x centroids will be the same as the y centroids covariance map but rotated by  $90^\circ$ . The covariance maps are multiplied by the square of the image scale to be in units of  $\text{arcsec}^2$ .

### 4.3.2 Calculating $r_0$

In order to determine the value of  $r_0$ , the theoretical spatial auto-covariance ( $A_{\delta i, \delta j}^t$ ) model, based on Kolmogorov's theory of turbulence was fitted to the measured spatial auto-covariances ( $A_{\delta i, \delta j}^m$ ). The theoretical auto-covariance map can be generated via numerical integration as described in Butterley et al. (2006) for a given WFS geometry and subaperture width. Code was supplied, courtesy of Timothy Butterley, for fast generation of theoretical auto-covariance maps. This method was verified by simulating auto-covariance maps for a large number of iterations and averaging them, such that the statistical uncertainty was small.

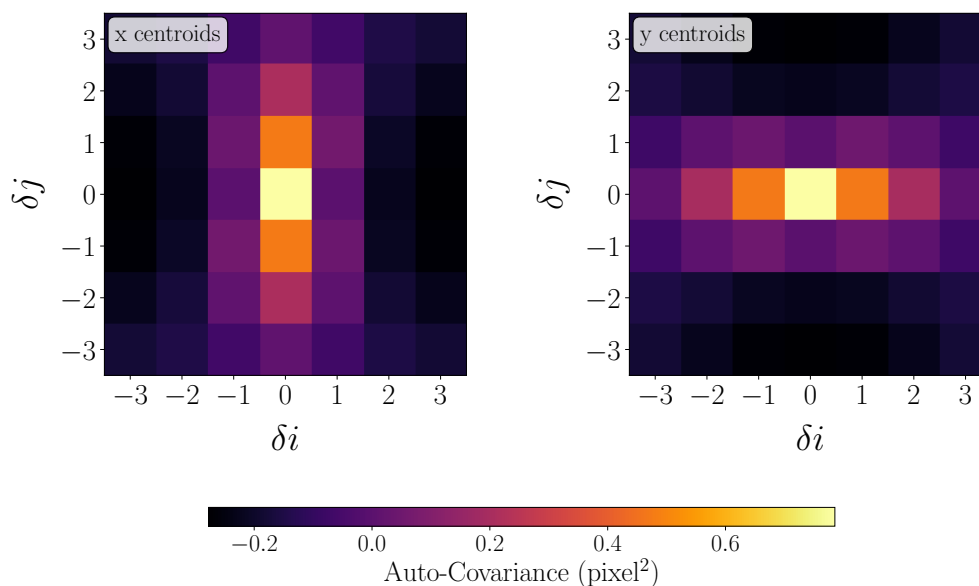


Figure 4.10: Example of a centroid spatial auto-covariance map, with units pixel<sup>2</sup>, produced from a simulated data packet with the spot pattern shown in figure 4.7.

Here the procedure to determine  $r_0$  from simulated data will be demonstrated. A 1-D slice is taken from the covariance map across  $\delta i = 0$  or  $\delta j = 0$  for x and y centroids respectively. This 1-D slice is used for the fit. By only fitting this 1-D slice some information is lost. However, the SNR in other parts of the covariance map is

low. Figure 4.11(a) shows examples of 1-D slices taken from y centroid covariance maps for different values of  $r_0$ . As  $r_0$  increases the shape of the 1-D slice remains the same but scales by a factor relating to  $r_0$ . Since the slice is symmetrical at  $\delta i = 0$  it is only necessary to look at  $\delta i = 0 - 3$ .

Figure 4.11(b) compares  $A_{\delta i, \delta j}^m$  and  $A_{\delta i, \delta j}^t$ , where  $\delta j = 0$  and  $\delta i = 0 - 3$  for a range of  $r_0$  values.  $A_{\delta i, \delta j}^t$  is given for an  $r_0$  value of 0.041 m. When the  $r_0$  value of  $A_{\delta i, \delta j}^t$  is the same as the  $r_0$  value of  $A_{\delta i, \delta j}^m$  the two maps should be equal, as conveyed by the  $x = y$  line in figure 4.11(b). However, when only the  $r_0$  value of  $A_{\delta i, \delta j}^m$  changes, the two maps will continue to have a linear relationship that passes through the origin but the gradient will change. Therefore, as  $r_0$  increases the gradient of  $A_{\delta i, \delta j}^m$  versus  $A_{\delta i, \delta j}^t$  decreases as a function of  $r_0$ . This linear relationship can be described mathematically as

$$A_{\delta i, \delta j}^m = A_{\delta i, \delta j}^t \left( \frac{r_0}{d} \right)^{-\frac{5}{3}}. \quad (4.4)$$

Figure 4.12 shows simulated results for the C9-SHIMM configuration with the expected  $r_0$  plotted against the estimated  $r_0$ . It can be seen that there is a good agreement. On-sky data will need to be corrected for airmass. Airmass is defined as,

$$X = \frac{1}{\cos(Z)}, \quad (4.5)$$

where  $Z$  is the zenith angle in radians. From this the airmass corrected  $r_{0A}$  can be calculated as

$$r_{0A} = r_0 X^{-\frac{3}{5}}. \quad (4.6)$$

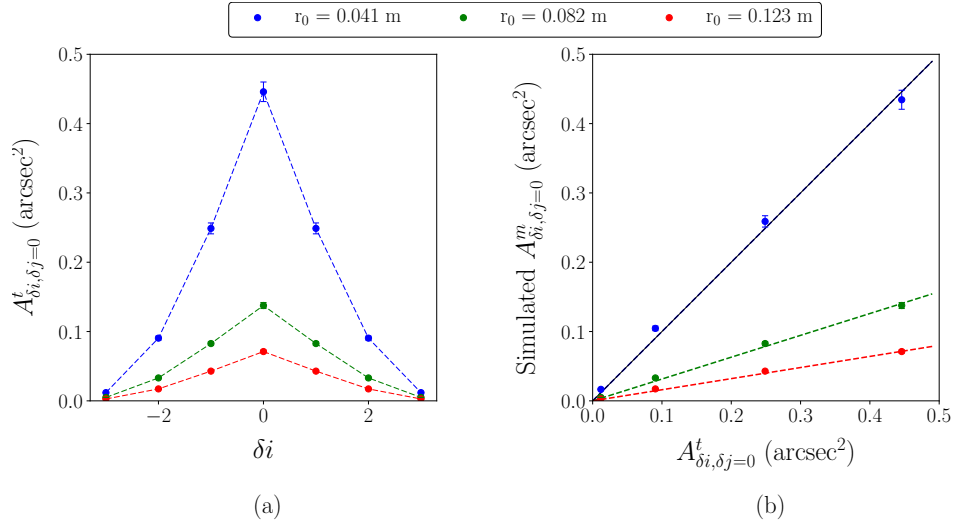


Figure 4.11: Simulated results taken from an auto-covariance map produced by using y centroids. (a) Shows a 1-D slice of the auto-covariance map where  $\delta j = 0$ . (b) Illustrates the relationship between the theoretical auto-covariance ( $A_{\delta i, \delta j}^t$ ) and the simulated measured auto-covariance ( $A_{\delta i, \delta j}^m$ ), where  $\delta j = 0$  and  $\delta i = 0, 1, 2, 3$ . The blue, green and red markers indicate results for different  $r_0$  values of 0.041 m, 0.082 m and 0.123 m respectively. The dashed lines indicate the linear fit. The black line is  $x=y$ . The error bars represent the statistical uncertainty of the simulation.

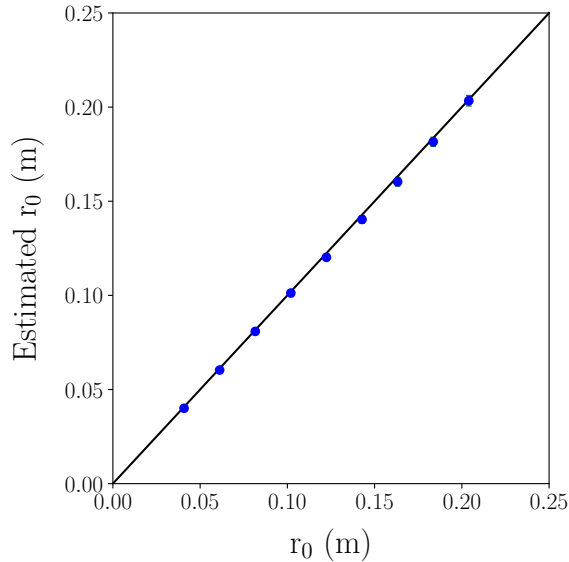


Figure 4.12: Simulated results displaying the expected  $r_0$  versus the estimated  $r_0$  (blue) and  $x = y$  line (black). The error bars are too small to be seen on this figure. The error bars represent the statistical uncertainty of the simulation.

## 4.4 Noise Analysis

Sources of noise in measuring the centroids of the spots include detector readout noise, as well as shot noise of the signal, the sky background and the detector dark current. Since short exposure images are used with bright sources, sky background and dark current noise are negligible.

In the presence of noise the fit described in the previous section requires modification, since the process of subtracting common motion of the centroids adds a constant bias to the whole auto-covariance function. For a complete step-by-step description of the effect of subtracting common tip/tilt see appendix A. The noise contribution to the auto-covariance is given as

$$\langle \epsilon'_l \epsilon'_m \rangle = \begin{cases} \left(1 - \frac{1}{n}\right) \langle \epsilon_l^2 \rangle & \text{if } l = m \\ -\frac{1}{n} \langle \epsilon_l^2 \rangle & \text{if } l \neq m \end{cases}, \quad (4.7)$$

where  $\epsilon$  is the noise in each centroid, subscripts  $l$  and  $m$  refer to the subaperture positions of  $[i, j]$  and  $[i', j']$  and  $n$  is number of subapertures. These describe the slopes for one axis (i.e. x centroids or y centroids). From equation 4.7 it can be seen that for large  $n$  the effect of noise becomes negligible except in case of  $i = j$  (i.e. the centroid variance). As a result, the central point ( $\delta i = \delta j$ ) of  $A_{\delta i, \delta j}^m$  is excluded from the fit described in the previous section. By excluding the central point an  $r_0$  estimate can be made independent of noise. The amount of noise present can be calculated from the measured central point and the expected central point given by the fit. This is the method employed by the data analysis for SLODAR observations.

However, since the C9-SHIMM only uses 12 subapertures, considerations need to be made when fitting the theoretical auto-covariance model to the measured auto-covariance (as described in the previous section). According to equation 4.7, for auto-covariances where  $\delta i \neq \delta j$  the value of the auto-covariance will shift down by  $-\frac{1}{n} \langle \epsilon_l^2 \rangle$ . Figure 4.13(a) demonstrates this for different noise levels. This means

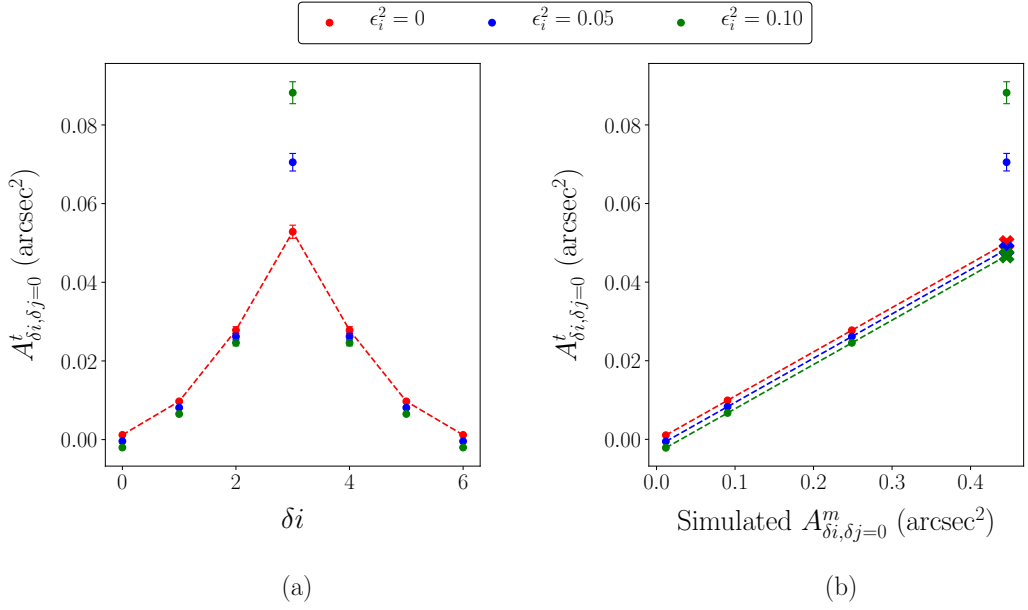


Figure 4.13: (a) Example  $A_{\delta i, \delta j}^m$ , where  $\delta j = 0$ , for simulated WFS data including shot noise. The dashed red line indicates the fit to the data in the case of zero noise. (b) Shows the effect noise has on the linear fit between  $A_{\delta i, \delta j}^t$  and  $A_{\delta i, \delta j}^m$ , where  $\delta j = 0$ . The dashed lines indicate the linear fit when the measured zero-offset point ( $j = i$ ) is excluded from the fit. The crosses indicate the estimated centroid variance in the absence of shot noise.

that the fit depicted in figure 4.11(b) will no longer intercept at the origin but will be offset by  $-\frac{1}{n}\langle\epsilon_i^2\rangle$ . However the gradient of the fit will remain unchanged, as shown in figure 4.13(b). The cross on the fit indicates the location of the estimated central peak value. The measured value (above the cross) is excluded from the fit.

## 4.5 On-Sky Tests

Table 4.2 gives the dates, observing sites, the test instrument and other on-site instruments making observations during the same period that can be used for comparisons.

Dates	Site	Instrument	Comparison Instrument	Approx. # hours
10 - 21 Sep 2016	La Palma	FASS-C11		5
23 - 28 July 2016	La Palma	FASS-C11		5
23 - 29 Apr 2016	Paranal	FASS-C9	Stereo- SCIDAR	18
30 Sep - 5 Oct 2015	La Palma	C9-SHIMM	Stereo- SCIDAR	11
25 - 30 Jun 2015	La Palma	C9-SHIMM	Stereo- SCIDAR	17

Table 4.2: List of observations with the SHIMM and corresponding comparison instrument.

### 4.5.1 SHIMM Data

As mentioned in section 4.3.2 the theoretical auto-covariance model was produced for a Kolmogorov atmosphere. By inspecting the data it appears the assumption was correct since there is a good fit between real data and the theoretical model. When the atmosphere is non-Kolmogorov the shape of the auto-covariance map changes and the fit shown in figure 4.11(b) becomes non-linear.

Figure 4.14 illustrates examples of on-sky data for a successful (a) and unsuccessful (b) fit. A single measurement of  $r_0$  required averaging over 1 – 5 minutes to reduce the statistical uncertainty. The error bars on the figure indicate this uncertainty. The poor fit could be due to a non-Kolmogorov atmosphere, to scintillation effects, discussed in chapter 6 or insufficient convergence of the covariance map.

A way to identify these cases is by the uncertainty of the fit that is given by the optimization routines provided by the SciPy python library (van der Walt et al., 2011), specifically using the `curve_fit` function. This function uses a least square minim-

ization routine, which outputs a covariance matrix that is used to estimate the uncertainty. When this uncertainty is greater than 20% the data is considered to have a poor fit. This occurred for  $\sim 15\%$  of the data. This limit of 20% was decided based on the correlation between the data obtained with the SHIMM and the other comparison instruments (see section 4.5.2). Uncertainty limits less than 20% did not change the value of the correlation coefficients of 0.85 when the SHIMM was compared with both the Stereo-SCIDAR and Robotic Differential Image Motion Monitor (RoboDIMM). However, including uncertainties up to 30% and 25% for the comparisons Stereo-SCIDAR and RoboDIMM respectively reduced the correlation relation to 0.84 and 0.81.

Figure 4.15 illustrates histograms of these results. It shows that in the case of a successful fit seeing values between 0.8 – 1.2 arcsec were estimated.

### **Repeatability**

In order to test the repeatability of the SHIMM instrument configuration, observations were taken simultaneously with two identical SHIMMs located side-by-side on the roof of the INT building. Data recorded in July and October 2015, illustrated in figure 4.16, indicates a good agreement between the two SHIMMs when they observe the same target. Measurements where the fit for acquiring  $r_0$  had an uncertainty greater than 20% were not included. It can be seen that there is a scatter on the results. Whilst they were side by side, the instruments were placed on the roof of the INT and was not in an open space. It is possible the wind shear and heat caused by the building effected the two SHIMMs differently. In addition, the ‘tube seeing’ that can occur in closed tube telescopes such as those used here, would have most likely been different. Given that the scatter is roughly equal along the  $x = y$  line it is unlikely that there is a systematic bias in either of the instruments.

### Target Magnitude Limitations

The arrangement of having two identical SHIMMs operating simultaneously permitted testing for the limiting target magnitude of the instrument. SHIMM1 observed a bright reference star, whereas SHIMM2 observed fainter stars at similar zenith angles and positions as the bright reference star. Figure 4.17 shows results of the seeing (a) and the noise (b) estimated by the two SHIMM instruments when observing targets of different brightness. Table 4.3 gives the correlation coefficients between the two C9-SHIMM instruments when the SHIMM2 is observing targets of different magnitudes. It can be seen that there is a much stronger correlation for  $V > 2.65$ . Figure 4.17(b) shows that the overall noise for SHIMM2 significantly diverges from that of SHIMM1 for targets fainter than  $V = 2.65$ . This indicates that the noise for fainter targets is dominated by shot noise, rather than statistical noise. Table 4.3 shows that for the faintest target the median noise value is almost double that of the brighter targets stars which a much larger variance in the estimated noise values. Therefore, it can be concluded that the preference is to always use second magnitude stars or brighter. However, even for third magnitude stars figure 4.17(a) shows that the estimation of  $r_0$  can still be accurate.

## 4.5.2 Comparison with Other Instruments

### Stereo-SCIDAR

For the observations made in July 2015 and October 2015 the SHIMM was located on the roof of the INT building. Concurrent observations were made with the high resolution Stereo-SCIDAR optical turbulence profiler instrument (Shepherd et al., 2013) mounted on the INT itself. Preliminary results for these nights are shown in figure 4.19. The comparison between the seeing measurements obtained from the SHIMM and the integrated turbulence strength from the Stereo-SCIDAR profiles

over these five nights is shown in figure 4.19(a). The results taken from these five nights produce a correlation coefficient of 0.85 between the two instruments.

For very low wind speed conditions, observations appeared to be badly affected by strong local turbulence. This effect was prominent for wind speeds less than 10 km/h ( $\sim 3$  m/s) where the correlation between the SHIMM and Stereo-SCIDAR drastically decreased. Low wind speeds are problematic since local turbulence does not traverse the telescope aperture quickly, and as a result the seeing measurement does not converge on a useful timescale, typically one minute. Therefore, observations made during wind speeds less than 10 km/h were discounted from the plot.

Figure 4.18 illustrates, in simulation, how slow wind speeds effect the measurement of  $r_0$  and its reliability. Figure 4.18 (a) shows how the value of  $r_0$  changes for different wind speeds for a range of dataset lengths when observing with the C9-SHIMM configuration (where exposure time is 2 ms and frame rate is 30 fps). As the length of the dataset increases the value of  $r_0$  plateaus. The error bars represent the statistical uncertainty in the measurement. Figure 4.18 (b) shows the standard deviation in these repeated measurements. It can be seen that for longer datasets ( 2 - 5 minutes) the standard deviation decreases substantially compared to short datasets ( $< 1$  minute). However, slower wind speeds have a systematically larger standard deviation than the faster wind speeds. This means that although the measurement of  $r_0$  is more accurate in the presence of slower wind speeds, as addressed by figure 4.5, the measurement of  $r_0$  is more precise for faster wind speeds as shown by the larger standard deviation in the repeated measurements. Further simulations were completed for a range of input  $r_0$  values. It was found that this conclusion was valid irrespective of the chosen value of  $r_0$ .

The uncertainties of the seeing measurements shown for the SHIMM, in figure 4.19(a), originate from the uncertainties of the fit described in equation 4.4. Seeing estimates where the uncertainty in the fit was greater than 20% were not included in the plot. These account for less than 9% of the data. The errors in Stereo-SCIDAR

are not shown but the statistical uncertainty for each measurement is of the order of 10%. However, the error analysis of the Stereo-SCIDAR is quite complex and varies with altitude, with very low and very high altitudes contributing more error (Shepherd et al., 2013).

### **RoboDIMM**

A comparison of the SHIMM and the Isaac Newton Group of Telescopes (ING)'s on-site RoboDIMM (O'Mahony, 2003a) is shown in figure 4.19(b) for the nights of 25 – 29th July. RoboDIMM data was acquired from public archives (O'Mahony, 2003b). In general, for every RoboDIMM data point there were two seeing estimates SHIMM. Therefore, the uncertainty in the SHIMM values was the accumulation of uncertainty associated with two data points. Although the plot indicates a correlation of 0.85, the same as the correlation between the SHIMM and Stereo-SCIDAR results, there is a much more obvious systematic overestimation of the seeing recorded by the SHIMM. Figure 4.19(c) also shows that when compared to the Stereo-SCIDAR, the RoboDIMM appears to show a systematic underestimation of the seeing. The spatial separation between the SHIMM and the RoboDIMM ( $\sim 370$  m) is much greater compared to the SHIMM and Stereo-SCIDAR, it is therefore not surprising that there is less agreement between the SHIMM and RoboDIMM as well as the Stereo-SCIDAR and RoboDIMM. The environments of all these instruments were very different. RoboDIMM is located permanently on a tower unaffected by local building structures and the Stereo-SCIDAR was inside a dome. Whereas the SHIMM was located on the INT roof, in close proximity to the control room door. Therefore, it is likely to have been affected by different local turbulence due to heat and the building structure, compared to the RoboDIMM and Stereo-SCIDAR. As described in section 4.1.2 finite exposure time will result in an underestimate in the seeing. In addition, chapter 6 details how scintillation noise could also results in an underestimate in the seeing. Due to these two instrumental effects, it was expected that the SHIMM in some instances would

underestimate the total integrated seeing. This indicates that the overestimation of the seeing observed by the SHIMM is likely due to local seeing that is not observed by the other instruments.

It can be seen that in both comparisons the SHIMM systematically overestimates the integrated turbulence strength with respect to Stereo-SCIDAR and the RoboDIMM, particularly in poor seeing conditions. Since the SHIMM was located next to the dome of the INT, it is likely to have experienced local seeing induced by the surrounding building. The RoboDIMM is located on an open tower away from the telescope buildings. As a result, the instrument is likely to experience less local seeing. Stereo-SCIDAR can remove the local seeing contribution from the estimate of the integrated turbulence strength by correcting for slow moving dome seeing. However, it is possible that the reduction process can overestimate this correction in slower low level wind speeds. Whilst observations during wind speeds less than 10 km/h were discounted, this effect could still be present in wind speeds higher than 10 km/h. In addition to this, it is possible that the SHIMM can suffer from tube seeing. Unlike the INT the SHIMM Celestron telescope is a closed tube telescope. Tube seeing arises from the different temperatures within the telescope tube itself. More observations are needed in order to identify whether this underestimation of seeing is a systematic effect, for example an image scale calibration error for one or more of the instruments, tube turbulence or if this was a result of local seeing specific to those nights.

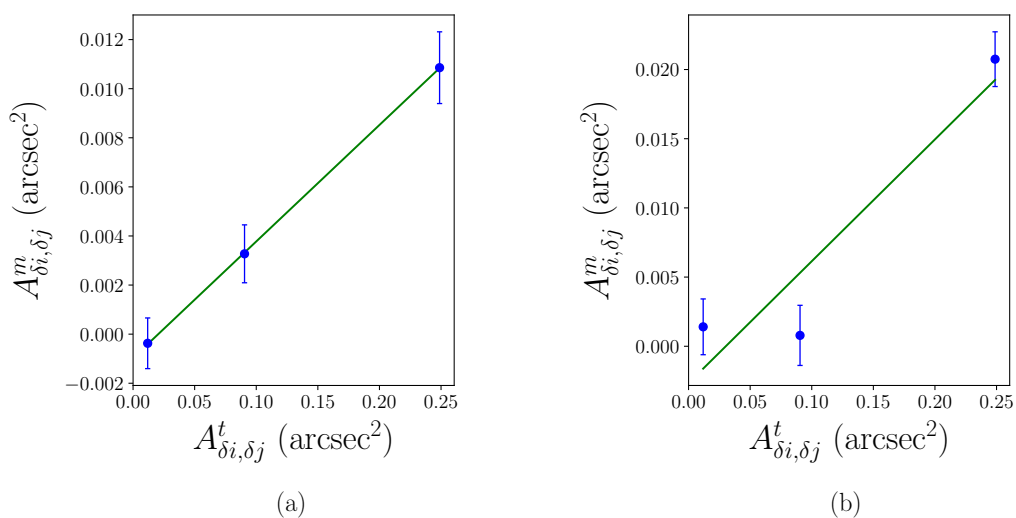


Figure 4.14: Example of on-sky results taken from an auto-covariance map (for  $\delta j = 0$ ) by using x centroids. (a) illustrates a good relationship between the theoretical and measured auto-covariances indicating showing that the assumption of Kolmogorov turbulence holds. (b) illustrates an example of a poor fit to the measured auto-covariance, which may be due to a number of reasons such as a non-Kolmogorov atmosphere, scintillation effects or insufficient convergence of the covariance map. The auto-covariance maps values were calculated by averaging maps that were acquired over a 5 minute interval. The error bars indicate the standard error of the averaged auto-covariance values.

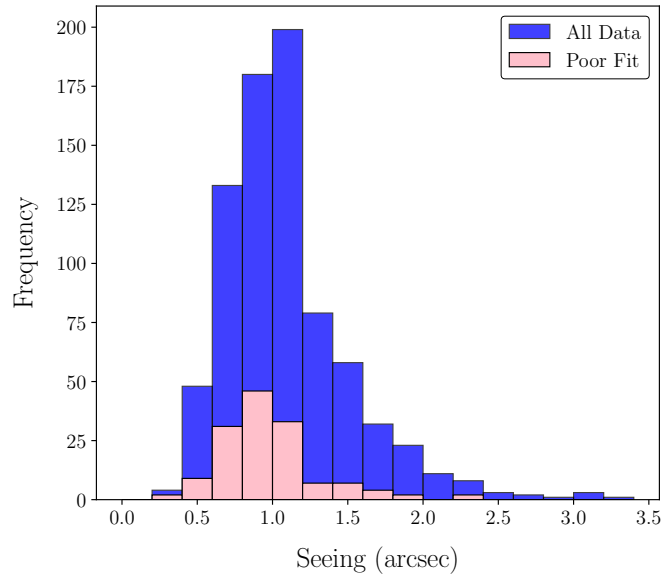


Figure 4.15: Histogram of seeing measurements taken on-sky in June and October 2015 by a C9-SHIMM located in La Palma. The different histograms indicate data where the fit for measuring  $r_0$  had an uncertainty of less than (blue) and greater than (pink) 20% possibly indicating instances that the Kolmogorov atmosphere assumption does not hold.

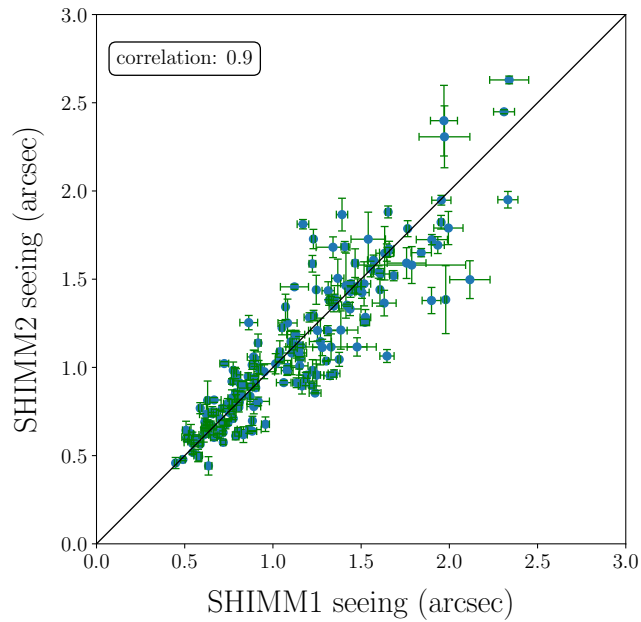


Figure 4.16: Results taken in June and October 2015 by two identical SHIMM instruments operating side by side observing the same target star.

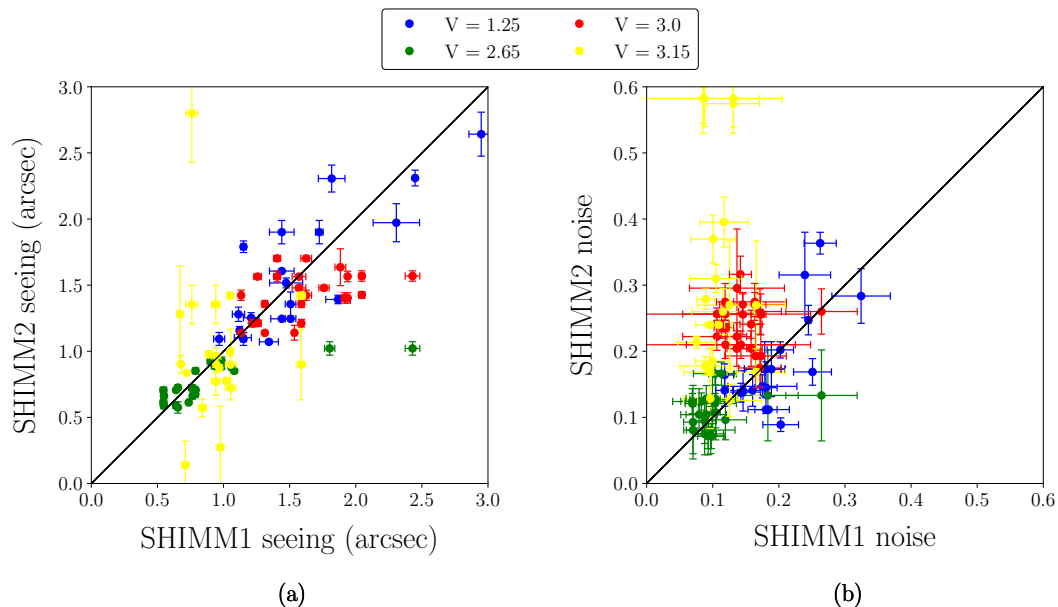


Figure 4.17: Measured on-sky seeing (a) and noise (b) comparisons between the two SHIMM instruments, where SHIMM1 observed targets of  $V = 1$  or brighter and SHIMM2 observed a range of target magnitudes.

Target Magnitude	Correlation Coefficient of Data (figure 4.17 (a))	SHIMM2 Noise (figure 4.17 (b))	
		Median	Variance
1.25	0.83	0.16	0.0048
2.65	0.78	0.11	0.0007
3.00	0.45	0.24	0.0012
3.15	$-1.4 \times 10^{-5}$	0.27	0.31

Table 4.3: Comparisons with the SHIMM1 and SHIMM2 data

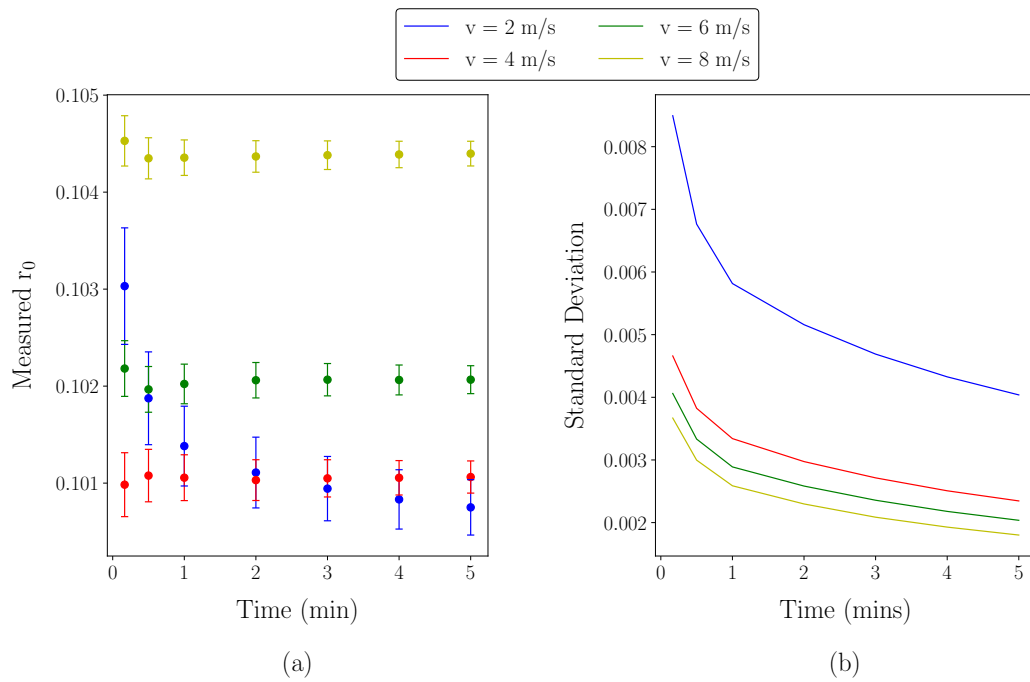


Figure 4.18: Simulated results showing the effects of slow wind speeds on the measurement of  $r_0$  and its reliability. This simulation is for the C9-SHIMM configuration with a frame rate of 30 fps and exposure time of 2 ms.

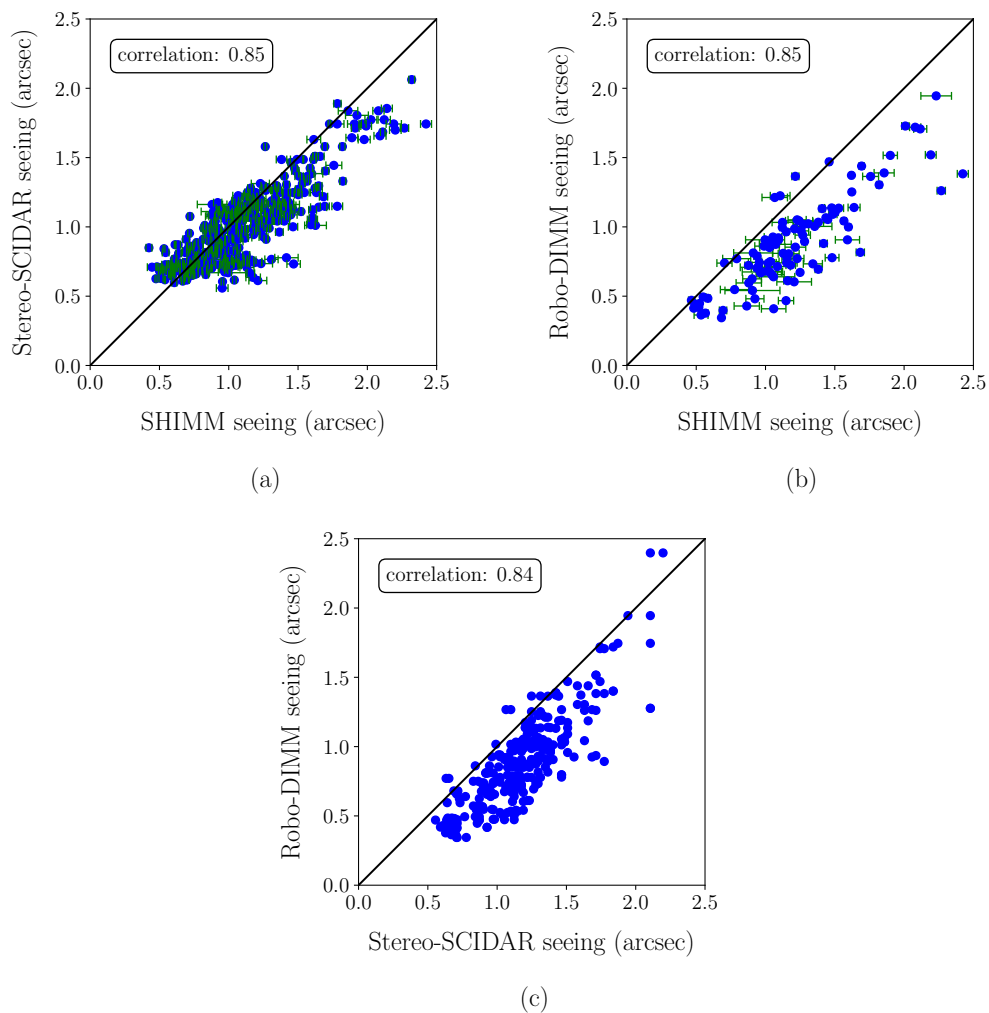


Figure 4.19: Preliminary results taken from five nights in June and October 2015. Here (a) compares SHIMM and Stereo-SCIDAR data, (b) compares SHIMM and RoboDIMM data and (c) compares Stereo-SCIDAR and RoboDIMM data. The black line in both plots are  $x = y$  lines.

## 4.6 Conclusions and Futher Work

The SHIMM is a new low-cost, compact, portable seeing monitor. In this chapter the instrument was presented from concept to deployment. The hardware and software required to operate this instrument under the initial requirements of being low-cost, compact and portable were discussed. The SHIMM employs a SH lenslet array to image an array of focused spots. This gives the SHIMM an advantage on the current DIMM instrument since it utilises more of the telescope aperture, but more importantly it can estimate  $r_0$  independent of noise. This is done by employing the SLODAR method of analysis.

Two configurations of the SHIMM were discussed: C9-SHIMM and C11-SHIMM. On-sky results of the C9-SHIMM taken at the ING, in La Palma were presented. These results included comparisons of the SHIMM with another SHIMM instrument, with Stereo-SCIDAR mounted on the INT and with the RoboDIMM permanently located on a tower on the ING site. Results show an excellent correlation between the two SHIMM instruments, demonstrating the repeatability of the SHIMM hardware configuration. Comparison with a second SHIMM allowed for on-sky determination of the minimum star target brightness that can be used. It was found that third magnitude stars can be used, however, to increase the signal to noise it is preferable to use a second magnitude star or brighter.

Comparisons with Stereo-SCIDAR showed a good correlation between the measured seeing values. There is a a tendency for the SHIMM to overestimate the seeing compared to the Stereo-SCIDAR and RoboDIMM. Local turbulence observed by the SHIMM is likely to contribute to this effect. However, there appears to be a systematic offset, possibly due to an image scale calibration error, which requires further investigation.

---

# SHIMM: Measuring the Atmospheric Coherence Timescale

In this chapter methods for estimating the atmospheric coherence time ( $\tau_0$ ) from SHIMM data will be described. Knowledge of this parameter is important for characterising the atmospheric conditions since it measures how fast the turbulence is evolving. This information is required for high-angular resolution techniques such as AO and interferometry (Kellerer and Tokovinin, 2007). For example, in AO the value of  $\tau_0$  indicates the timescale on which the AO correction procedure needs to operate in order for that correction to still be valid. Whilst there has been disagreement over the definition of  $\tau_0$ , it is now generally accepted that it is the time for optical phase changes of order  $\pi$  to occur at a given position, i.e.  $D_\phi(\tau_0) = \pi^2$  (Labeyrie et al., 2006).

By assuming frozen flow the turbulence can be modelled as a phase screen that traverses over the telescope aperture. In order to measure the velocity of the turbulent layer, the distance it has travelled in a given time must be measured. Therefore, the position of the turbulent layer needs to be measured at least twice before it traverses the full telescope aperture diameter. The C9-SHIMM was not designed with the intention of estimating the value of  $\tau_0$ . Since it utilises a 9.25 inch telescope aperture and a camera frame rate of 30 Hz the maximum detectable velocity

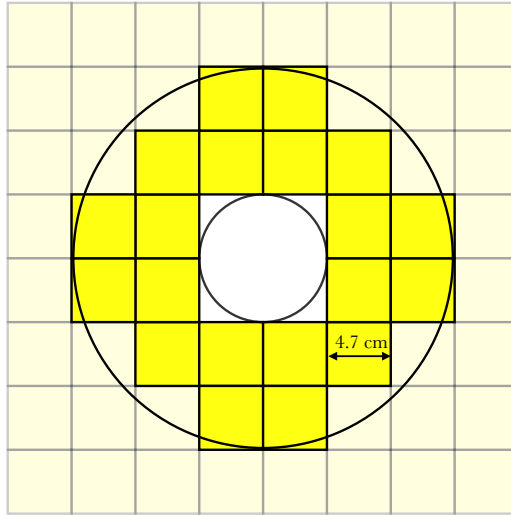


Figure 5.1: Illustration of the illuminated subapertures of the WFS mapped onto the C11-SHIMM telescope aperture, where each subaperture is 4.7 cm.

is  $\sim 7$  m/s. This value is too small to accurately measure  $\tau_0$ , since typical atmospheric turbulence velocities are faster. The C11-SHIMM was therefore configured with a larger telescope aperture of 11 inches and a CCD with a faster maximum frame rate of 200 Hz, (the mapping of the subapertures is shown in figure 5.1). This results in a maximum detectable velocity of  $\sim 55$  m/s. In reality the detectable velocity is slower. This is because the methods used, in this chapter, to measure wind speed requires the turbulent layers to move less than the aperture length for a given step. This will be discussed further in this chapter. Another reason is because square subapertures are used to sample a circular telescope aperture. In order to use fully illuminated subapertures, the whole telescope aperture can not be sampled, as depicted in figure 5.1. Utilising a larger telescope aperture has the additional advantage of allowing for larger subapertures which increases the amount of light collected and thereby increases the range of target magnitudes that can be used.

As described by equation 2.11,  $\tau_0$  is inversely proportional to the effective wind-blown turbulence velocity ( $v_{eff}$ ), which is defined by equation 2.12. In this chapter

two different methods for estimating  $v_{eff}$  will be discussed, for the C11-SHIMM configuration. The first method looks at the spatio-temporal auto-covariance of the spot centroids to calculate  $v_{eff}$ . The second was inspired by the FAst DEfocus monitor (FADE) method which uses the power frequency spectrum of the defocus Zernike mode to establish  $v_{eff}$  (Tokovinin et al., 2008).

After exploring both methods it was concluded that estimating  $\tau_0$  by using the power spectrum was more accurate for the SHIMM analysis. The power spectrum method was employed to estimate  $\tau_0$  for on-sky data. The results will be presented in this chapter. Whilst this method is preferable, the covariance map method can provide a useful graphical representation of turbulent layer velocities for on-sky data.

## 5.1 Covariance Map Method

Assuming frozen flow, the pattern of the WFS slopes traverse the telescope aperture at the wind speed of the corresponding turbulent layer. If an auto-covariance map,  $A_{\delta i \delta j}$  (see chapter 4), is made from the WFS centroid dataset then a peak will appear in the centre of the map, which corresponds to the superposition of all of the turbulent layers. However, if a spatio-temporal auto-covariance,  $T_{\delta i, \delta j, \delta t}$ , is taken for a centroid dataset at  $t = 0$  and with the same dataset but at  $t = \delta t$ , then the peaks corresponding to each layer will be offset by an amount related to the distance and direction that the turbulent layer has travelled in the time  $\delta t$  (Osborn, 2010).

The SHIMM requires common motion to be subtracted from the centroids in order to remove the effects of wind shake and telescope guiding errors. This means that the global tip/tilt due to the atmospheric aberrations are also subtracted. The covariance map method was explored for centroid datasets with and without common motion subtraction, in order to evaluate the effects subtracting tip/tilt has on measuring  $\tau_0$ . Both scenarios are described in this section. It is important

to note that all error bars indicated on results from simulated data is a result of the statistical uncertainty of the end-to-end simulation, without the presence of additional noise contributions such as shot noise.

### 5.1.1 With Common Motion

Figure 5.2 illustrates an example of a spatio-temporal auto-covariance map for a simulated dataset where a single turbulent layer traverses the telescope aperture at 9.4 m/s, in the direction of left to right with respect to the SH lenslet array. Since it is a single turbulent layer this motion of the layer can be seen by the central peak moving across the map over each minimum time step of 5 ms. From this the velocity of this layer can be estimated. It can be seen that the peak moves one subaperture separation (i.e. one covariance map element) in a single time step. Since the subaperture width is 4.7 cm and  $t = \delta t = 5$  ms, the wind speed is estimated to be 9.4 m/s, as expected.

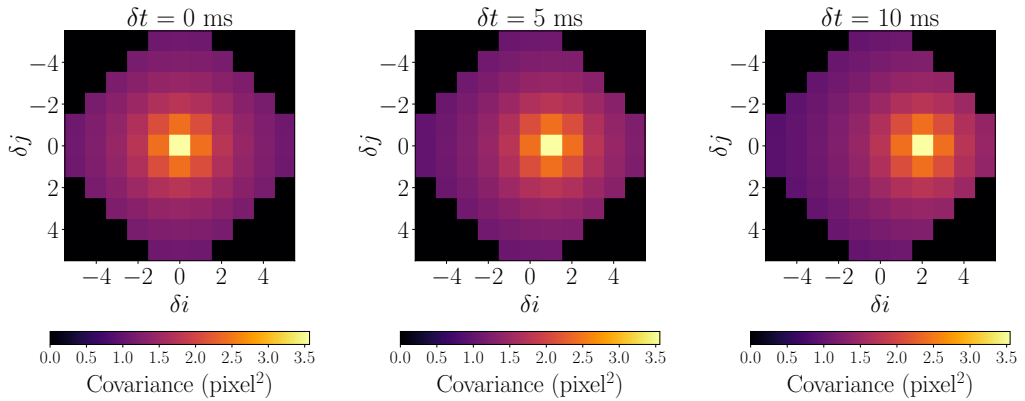


Figure 5.2: Simulated spatio-temporal auto-covariance map, for the C11-SHIMM configuration, at  $\delta t = 0, 5$  and  $10$  ms, when common motion has not been subtracted from the centroid dataset.

Since  $\delta t$  is a fixed value (5 ms in this case), and the subaperture sizes are known, the covariance map can be considered as a velocity map, where each map element

represents an offset for a particular wind velocity, with the central speed value of 0 m/s. Figure 5.3 shows the velocity map for  $\delta t = 5$  ms. The direction of the turbulent layer traversing the telescope aperture with respect to the SH lenslet array ( $\theta_{trav}$ ) is indicated by the compass in figure 5.3. When  $\theta_{trav} = 0^\circ$  the turbulent layer is travelling left to right.

The covariance maps in figure 5.2 have an approximately constant ‘background’ level, at points well away from the peak. However, adjacent map elements to the peak are greater than this background. This is because the peak is not a delta function, but instead has a FWHM that is approximately two covariance map elements. This is illustrated by simulated results in figure 5.4(a) by taking a 1-D slice of  $T_{\delta i, \delta j, \delta t}$  where  $\delta j = 0$  and  $\delta t = 5$  ms. The results show a simulation of a single turbulent layer with an input wind speed 18.8 m/s and  $\theta_{trav} = 0^\circ$ . The peak value is located at  $\delta i = 2$ , which corresponds perfectly with the input wind speed of 18.8 m/s.

If a turbulent layer has not travelled by a distance exactly equivalent to a subaperture width this spread of the peak can be asymmetric. In addition, in the presence of multiple layers of different velocities the covariance response from two different layers may superimpose and become indistinguishable. For the measurement of  $\tau_0$ , only the value of  $v_{eff}$  is required, and not the whole of the wind velocity profile. The value for  $v_{eff}$  is estimated according to the following

$$v_{eff}^{-\frac{5}{3}} = \alpha_1 v_1^{-\frac{5}{3}} + \dots + \alpha_n v_n^{-\frac{5}{3}} \quad (5.1)$$

where  $v$  is the velocity of individual turbulent layers  $n$ , and  $\alpha$  is the corresponding relative turbulence strength.

Due to the pattern of the WFS mask the spatio-temporal auto-covariance map has multiple subaperture separations that are associated with the same wind speed, as can be seen in figure 5.3. As a result, the covariance response is azimuthally averaged. This eliminates the need to measure  $\theta_{trav}$ , or the speeds of individual turbulent layers.

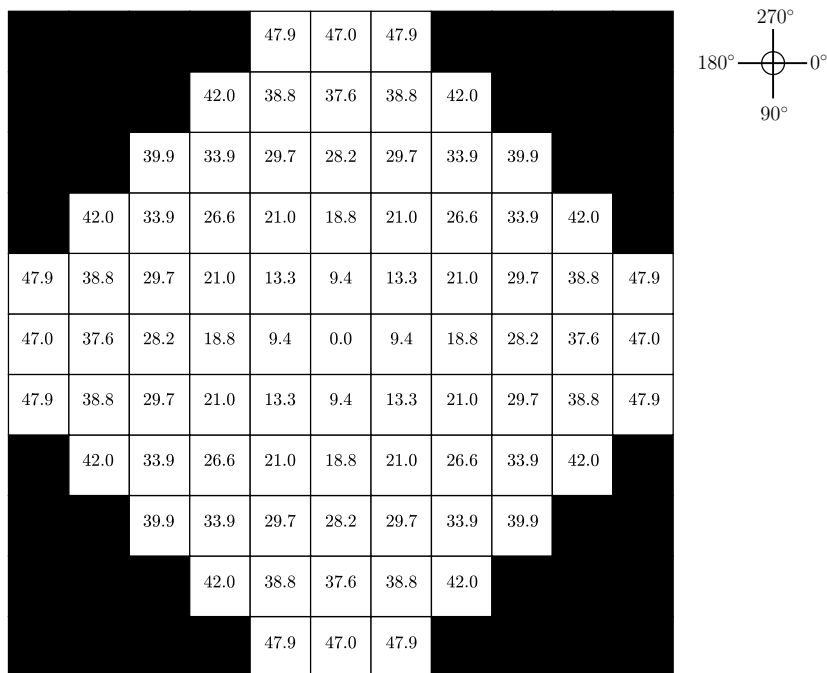


Figure 5.3: Velocity map, in units of m/s, illustrating how each subaperture separation in the covariance map relates to a particular wind speed at  $\delta t = 5$  ms. The compass indicates the value of  $\theta_{trav}$  is defined relative to the SH lenslet array.

Figure 5.4(b) displays simulated results of a 1-D slice  $T_{\delta i, \delta j, \delta t}$  where  $\delta j = 0$  and  $\delta t = 5$  ms for a two turbulent layer profile of equal turbulent strength. The wind speed and orientation of each turbulent layer is 18.8 m/s and 37.6 m/s and  $\theta_{trav} = 0$  and  $180^\circ$  respectively. Since they are of the same strength the peaks of the two layers are of the same value. To calculate  $v_{eff}$  the absolute strength is not required, only the values for  $\alpha$ , which are approximated as the averaged and normalised covariance strength for each wind speed.

It can be seen in figures 5.4(a) and (b) that there is a non zero minimum value of the covariance. This causes a bias to high velocities, due to the  $5/3$  power in equation 5.1. In order to correct this effect, the mean of the covariance map is subtracted from each covariance value and negative values are set to zero. Figure 5.5 illustrates how this allows for only the peaks corresponding to turbulent layers to be included in the calculation of  $v_{eff}$ .

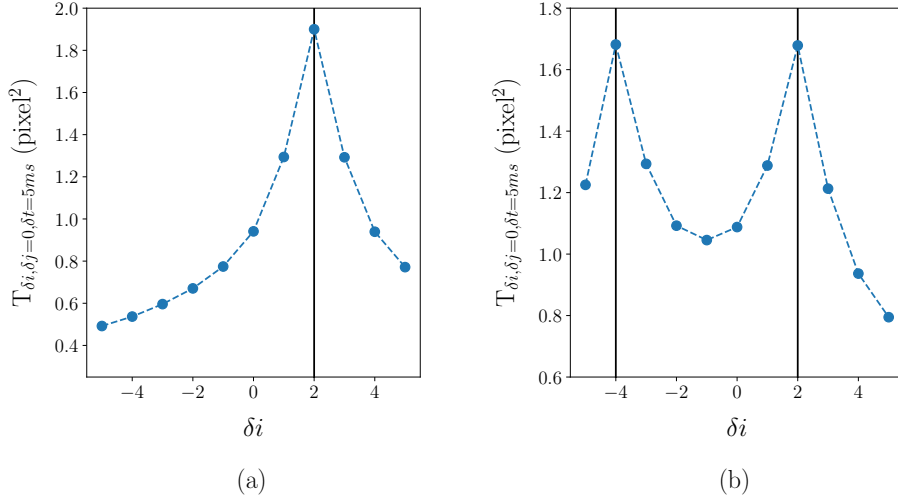


Figure 5.4: Simulated results displaying a 1-D slice of  $T_{\delta i, \delta j, \delta t}$  where  $\delta j = 0$  and  $\delta t = 5$  ms for (a) a single turbulent layer with wind speed 18.8 m/s and  $\theta_{trav} = 0^\circ$  and (b) two turbulent layers with wind speeds 18.8 m/s and 37.6 m/s and  $\theta_{trav} = 0^\circ$  and  $180^\circ$  respectively. The black vertical lines depict a delta function at the corresponding wind speeds.

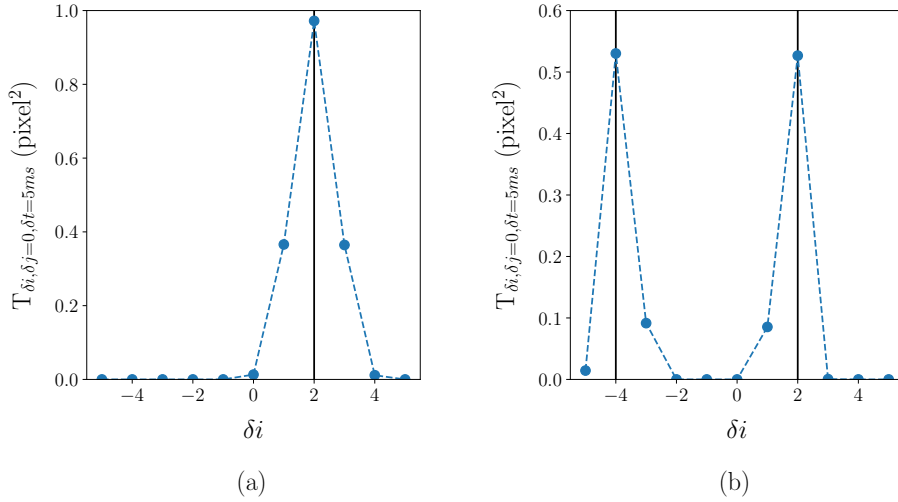


Figure 5.5: Simulated results with background subtraction for a slice of  $T_{\delta i, \delta j, \delta t}$  where  $\delta j = 0$  and  $\delta t = 5$  ms for (a) a single turbulent layer with wind speed 18.8 m/s and  $\theta_{trav} = 0^\circ$  and (b) two turbulent layers with wind speeds 18.8 m/s and 37.6 m/s and  $\theta_{trav} = 0^\circ$  and  $180^\circ$  respectively. The black vertical lines depict a delta function at the corresponding wind speeds.

### One Turbulent Layer System

Figure 5.6 shows simulated results for a single turbulent layer traversing the telescope aperture for a range of velocities. The figure demonstrates that for a single turbulent layer travelling at  $\theta_{trav} = 0^\circ$ , input wind speeds between 10 - 35 m/s agree, within the error bars, with the measured outputs. For wind speeds less than 10 m/s the spatial resolution is not high enough to distinguish between turbulence strength at very low speeds and at 0 m/s. The measurement of wind speeds greater than 35 m/s would require either a larger telescope aperture or a detector capable of taking images at a faster frame rate. However, as illustrated in figure 4.4 in section 4.1, wind speeds are typically below this range. Results for  $\theta_{trav} = 45^\circ$  show that the deviation from the  $x = y$  line occurs at lower wind speeds. This is expected since the effective extent of the sampled telescope aperture is smaller at  $\theta_{trav} = 45^\circ$ , i.e. the range of detectable velocities is less in this direction (see figure 5.3).

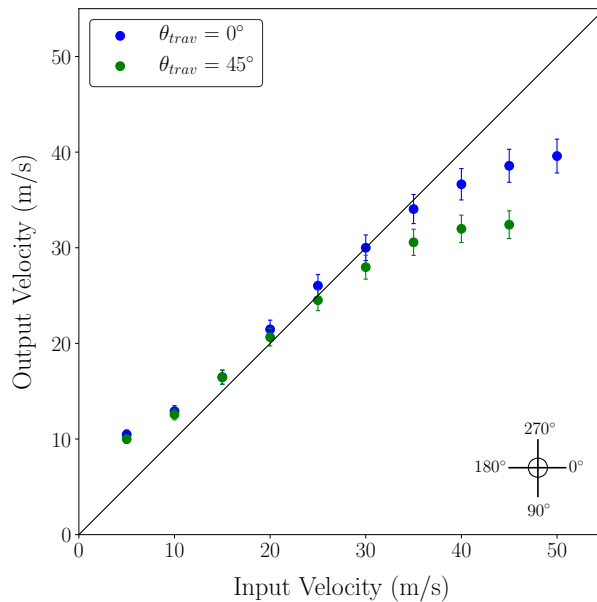


Figure 5.6: Simulated results of the input velocity of a single turbulent layer against the measured output velocity for different traversing direction of  $0^\circ$  (blue) and  $45^\circ$  (green). The direction of the turbulent layer is given relative to the SH lenslet array and is indicated by the compass. This is the same as that shown in figure 5.3.

## Two Turbulent Layer System

This method was further tested by applying it to atmospheric profiles with two turbulent layers. Simulated results are shown in figure 5.7. Optical turbulence profiles made of two layers were simulated for conditions where one layer traverses the telescope at  $\theta_{trav} = 0^\circ$  with an  $r_0$  value of 0.1 m. The second layer traverses the telescope in the opposite direction of  $\theta_{trav} = 180^\circ$  for a range of  $r_0$  values and speeds. Figure 5.7 indicates there is a good correlation between the input and output  $v_{eff}$ . It appears that for weaker faster moving turbulent layers  $v_{eff}$  can be underestimated. This could be a result of the background subtraction causing a ‘dampening’ of the signal of these layers.

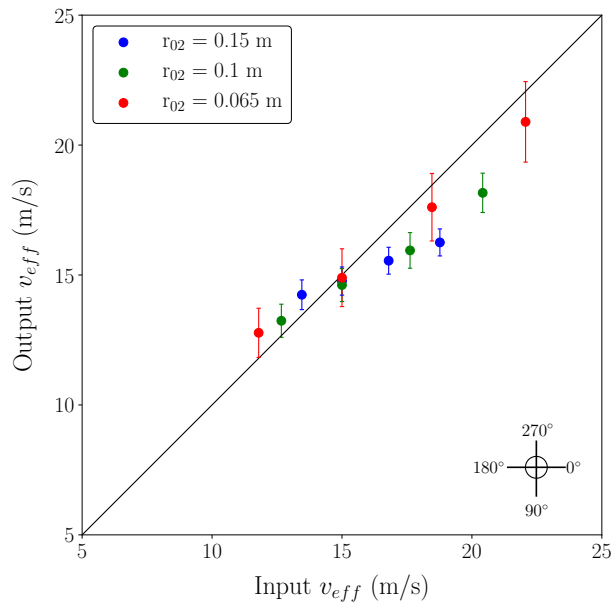


Figure 5.7: Simulated results of output  $v_{eff}$  against input  $v_{eff}$  for a two turbulent layer atmosphere. One layer has an  $r_0$  value of 0.1 m and at a wind speed of 15 m/s travelling at  $0^\circ$ . The other layer is traversing in the  $180^\circ$  direction at varying wind speeds for  $r_0$  values of 0.065, 0.1 and 0.15 m denoted by the blue, green and red markers respectively.

Figures 5.6 and 5.7 illustrate that this method can be used to estimate  $v_{eff}$  (and therefore  $\tau_0$ ) on centroid datasets without common motion subtraction. Large telescopes sheltered by a dome are much more stable and are not as effected by tracking errors and wind shake as smaller telescopes, such that subtracting common motion may not be necessary.

### 5.1.2 Without Common Motion

The SHIMM is a small portable instrument and is therefore affected by wind shake and telescope guiding errors. In order to remove these effects the common centroid motion of all subapertures must be subtracted. In this section the method above will be described for centroid datasets with common motion subtracted. Figure 5.8 illustrates an example spatio-temporal auto-covariance map obtained from a simulated single turbulent layer traversing the telescope at 9.4 m/s, where  $\theta_{trav} = 0^\circ$ . In figure 5.2, where common motion is not subtracted, it can be seen that there is an approximately constant background level. When common motion is subtracted there is typically a gradient of the background level across the auto-covariance map (see figure 5.8). This gradient occurs in the direction of  $\theta_{trav}$ . This becomes problematic when there is more than one turbulent layer present. As will be shown later in this section.

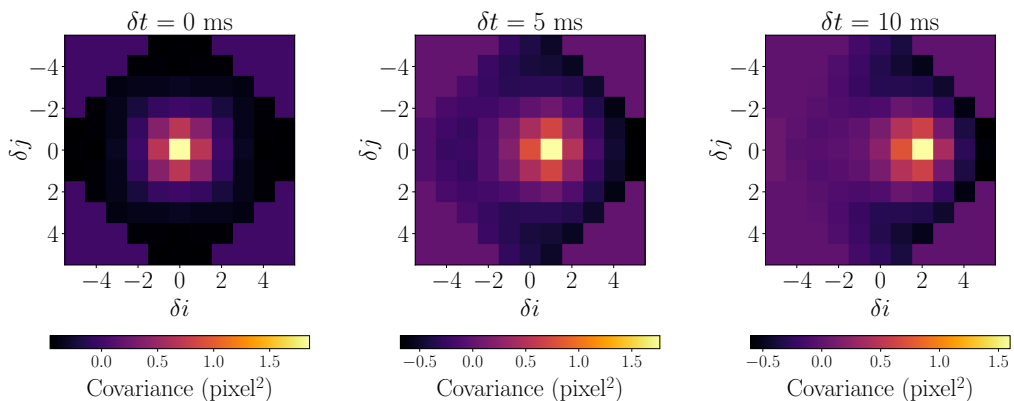


Figure 5.8: Simulated spatio-temporal auto-covariance map at  $\delta t = 0, 5, 10$  ms, when common motion has been subtracted from the centroid dataset.

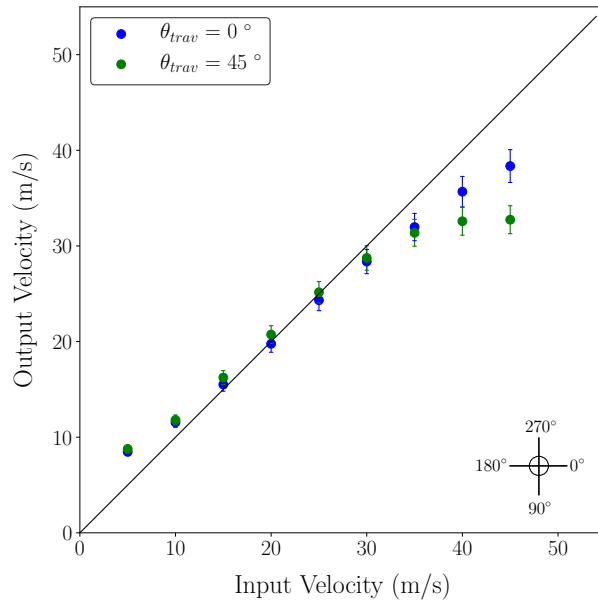


Figure 5.9: Simulated results of the measured output velocity of a single turbulent layer against the input velocity, when common motion is subtracted, for  $\theta_{trav} = 0^\circ$  (blue) and  $45^\circ$  (green). The definition of the direction of the turbulent layer is indicated by the compass on the bottom right of the image.

### One Turbulent Layer System

First the method described in the previous section was applied to a single turbulent layer. Figure 5.9 shows simulated results for a single turbulent layer, for a range of velocities, with common motion subtracted from the centroid datasets. These results are similar to those displayed in figure 5.6. This method correctly estimates the value of  $v_{eff}$ , for a velocity range of 10 - 35 m/s, within the statistical uncertainty. As with the results depicted in figure 5.6, turbulent layers travelling at  $\theta_{trav} = 45^\circ$  reach an asymptote faster than those travelling at  $\theta_{trav} = 0^\circ$  since the effective extent of the telescope aperture is smaller at  $\theta_{trav} = 45^\circ$ .

### Two Turbulent Layer System

This method was further tested for a two layer turbulent profile, with common motion subtraction. Optical turbulence profiles made of two layers were simulated for conditions where one layer traverses the telescope at  $\theta_{trav} = 0^\circ$  with an  $r_0$  value

of 0.1 m. The second layer traversed the telescope in the opposite direction of  $\theta_{trav} = 180^\circ$  for a range of  $r_0$  values and speeds.

Figure 5.10 indicates that there is a consistent bias to underestimate  $v_{eff}$ . The level of this bias increases for increasing values of  $v_{eff}$ . This is because of the gradient of the background layer. The affect of this gradient is illustrated in figure 5.11 by using a 1-D slice of  $T_{\delta i, \delta j, \delta t}$  where  $\delta j = 0$  and  $\delta t = 5$  ms. The figure shows three 1-D slices of  $v = 10$  m/s with  $\theta_{trav} = 180^\circ$ ,  $v = 30$  m/s with  $\theta_{trav} = 0^\circ$  and for the case where both turbulent layers are traversing the telescope aperture simultaneously. Each value of  $\delta i$  corresponds to a wind velocity (see figure 5.3). When the two layers are added, the peak value associated with the faster turbulent layer decreases and the peak value of the slow layer increases. This biases the results to underestimate  $v_{eff}$ .

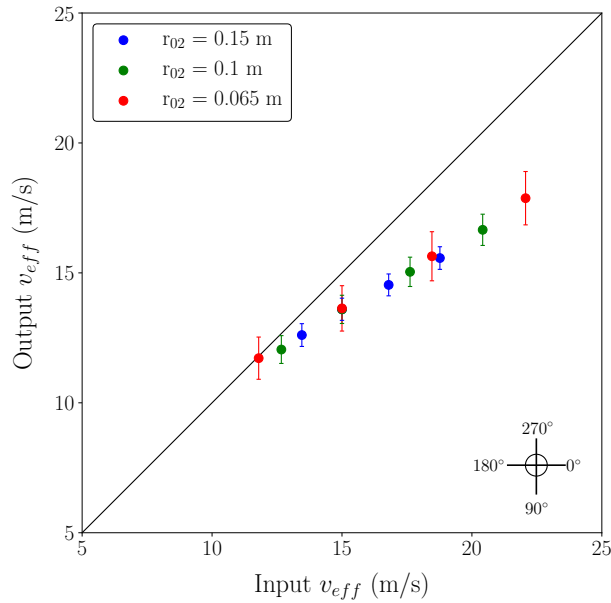


Figure 5.10: Simulated results of output  $v_{eff}$  against input  $v_{eff}$  for a two turbulent layer atmosphere. One layer has an  $r_0$  value of 0.1 m and at a wind speed of 15 m/s travelling at  $\theta_{trav} = 0^\circ$ . The other layer is traversing in the opposite direction  $180^\circ$  at varying wind speeds for  $r_0$  values of 0.065, 0.1 and 0.15 m denoted by the blue, green and red markers respectively.

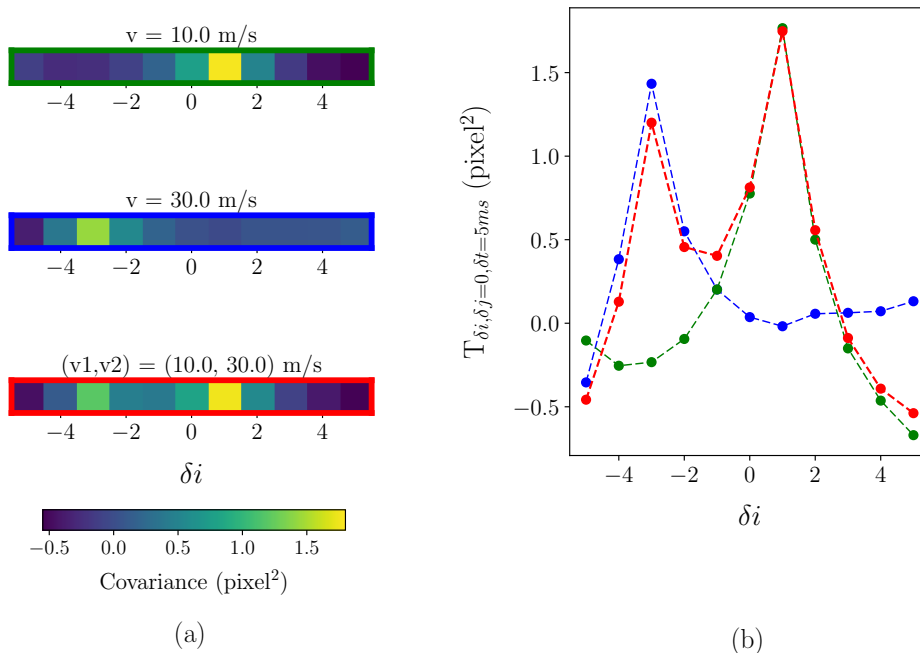


Figure 5.11: Simulated results displaying the effects of subtracting common motion for two layer turbulence profiles. (a) illustrates 1-D slices of  $T_{\delta i, \delta j, \delta t}$  where  $\delta j = 0$  and  $\delta t = 5\text{ms}$  for  $v = 10 \text{ m/s}$  traversing at  $\theta_{trav} = 180^\circ$  (blue),  $v = 30 \text{ m/s}$  traversing at  $\theta_{trav} = 0^\circ$  (green) and for the case where both turbulent layers are traversing the telescope aperture simultaneously (red). Each layer has an  $r_0 = 0.1 \text{ m}$ . (b) Illustrates these slices in 1-D.

### 5.1.3 Conclusion

Simulated results indicate that the covariance map method can only be used in the case where common motion is not subtracted. This would be applicable to a larger telescope with dome infrastructure which could ensure that wind shake and tracking errors are not problematic. The effects of subtracting common motion cause faster turbulent layers to be underestimated, therefore overall reducing the value of  $v_{eff}$  and increasing the estimated value of  $\tau_0$ .

Whilst this method can not be used quantitatively, it can be used qualitatively to display the different turbulent layers that are present. For example, it can display the relative strongest layers present. Figures 5.12 - 5.14 illustrate examples of on-

sky spatio-temporal auto-covariance maps, obtained by the C11-SHIMM, at the ING site in La Palma. In the examples of figures 5.12 and 5.13 the observations are dominated by a single slow moving turbulent layer, whereas in the case of figure 5.14, there are at least two strong turbulent layers, with different speeds and directions.

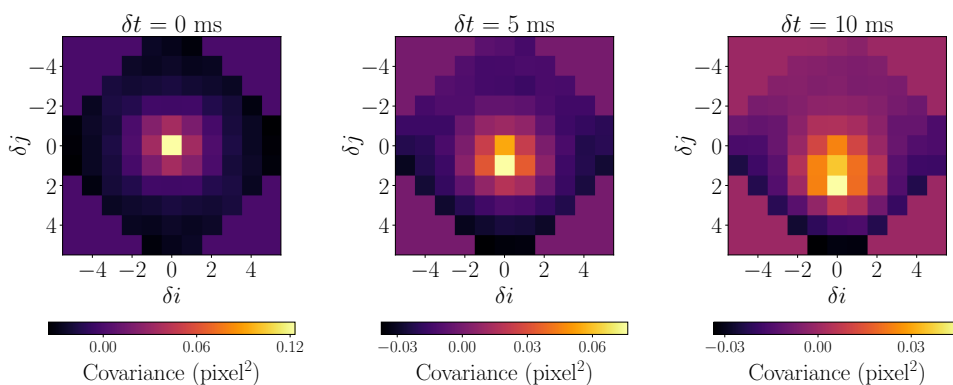


Figure 5.12: Example of an on-sky spatio-temporal auto-covariance map at  $\delta t = 0, 5, 10$  ms.

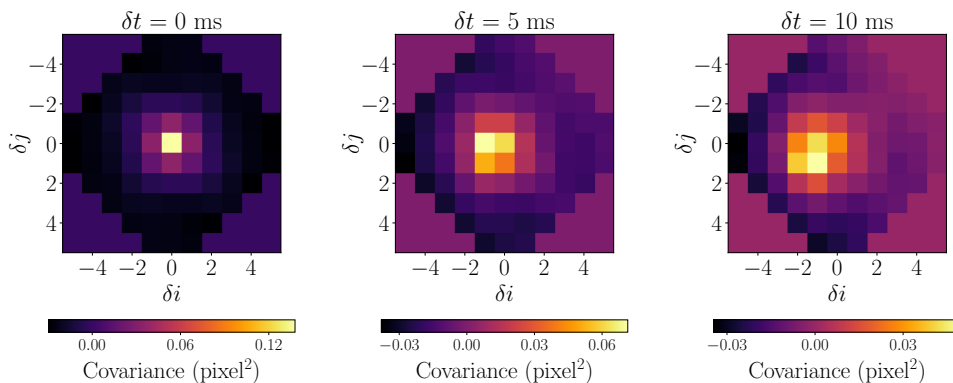


Figure 5.13: Example of an on-sky spatio-temporal auto-covariance map at  $\delta t = 0, 5, 10$  ms.

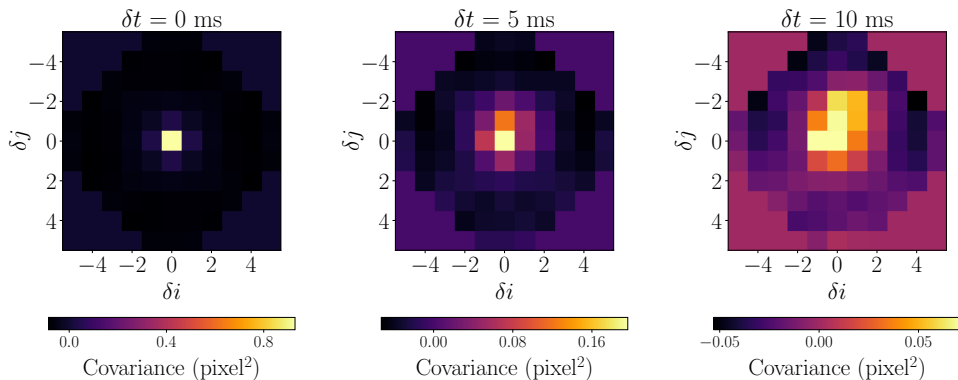


Figure 5.14: Example of an on-sky spatio-temporal auto-covariance map at  $\delta t = 0, 5, 10$  ms.

## 5.2 Power Spectrum Method

In this section a different approach for calculating  $\tau_0$  will be discussed. By acquiring the power spectrum of the centroid motion from each subaperture  $v_{eff}$  can be inferred. The power spectrum, as a function of frequency,  $f$ , is given as

$$\Phi(f) = |\mathcal{F}x(t)|^2 \quad (5.2)$$

where  $\mathcal{F}$  denotes a Fourier transform and  $x(t)$  is the x and y centroid motion. Figure 5.15(a) and (b) show examples of a log-log power spectrum, averaged over all subapertures. The simulated data is of a single turbulent layer traversing the telescope aperture at a wind speed of 1 m/s and 5 m/s respectively. The figure shows that the power spectrum at low frequencies behaves as  $f^{-2/3}$  and high frequencies as  $f^{-11/3}$  (Hogge and Butts, 1976; Saint-Jacques, 1998). The knee frequency ( $f_{knee}$ ) where these two lines intersect, is related to the value of the wind speed,  $v$ , by

$$f_{knee} = \beta \frac{v}{d}, \quad (5.3)$$

where  $d$  is the subaperture size and  $\beta$  is a constant that is determined empirically. This method for measuring  $v$  can be problematic. Estimating  $f_{knee}$  can be difficult for noisy data and for atmospheric profiles with multiple layers. Figure 5.15(c) shows an example power spectrum of a two turbulent layer profile, of wind speeds

1 m/s and 5 m/s of equal strength. The sets of dashed lines indicate where the two values of  $f_{knee}$  should be located. The oscillations at high frequencies are a peculiarity of the spatial sampling, and in reality would be smeared out as soon as there is some variability in wind velocity (Conan et al., 1995; Saint-Jacques, 1998). It can be seen that these locations are not as easily identifiable compared to figures 5.15(a) and (b), in the single layer case.

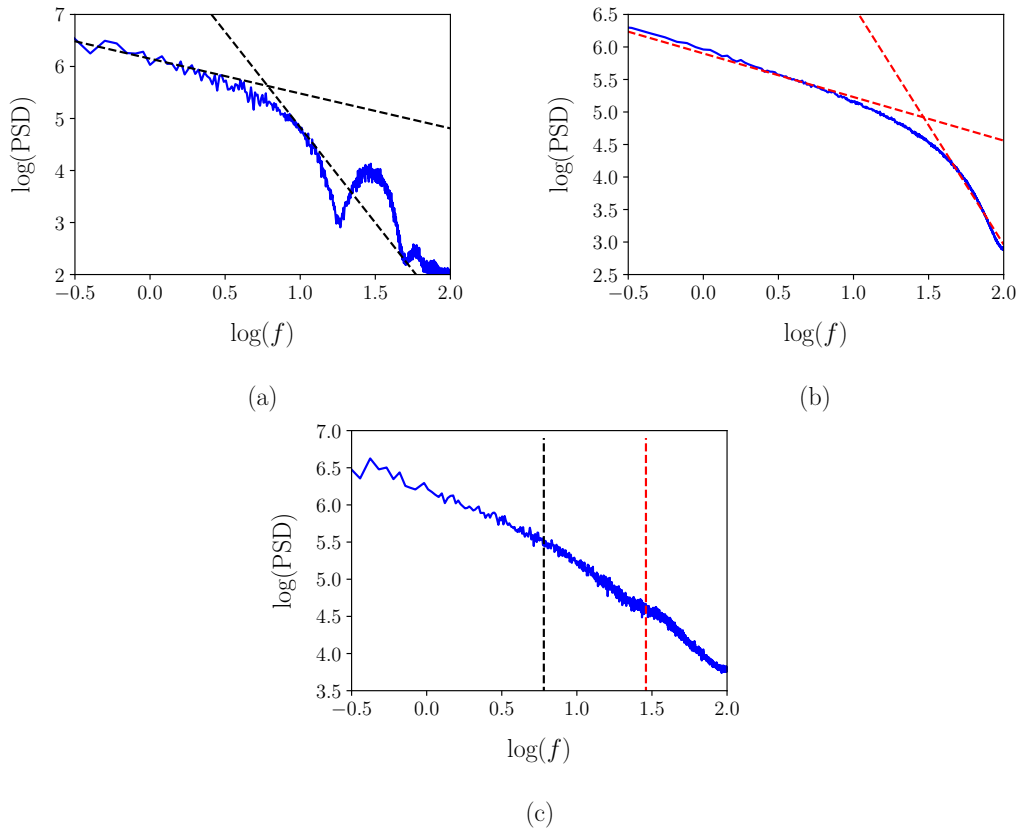


Figure 5.15: Power spectra of centroid datasets averaged over all WFS subapertures. (a) and (b) Displays power spectra obtained from a single turbulent layer traversing the telescope aperture at a wind speed of 1 m/s and 5 m/s respectively. The intercept of the two dashed lines show that spectra at low frequencies behaves as  $f^{-2/3}$  and high frequencies as  $f^{-11/3}$ . (c) Shows a power spectra for a two layer turbulence profile, of wind speeds 1 m/s and 5 m/s of equal strength. The red dashed line indicates the  $\log(f)$  value for the expected  $v_{eff}$ .

Another disadvantage of this method is that as  $v$  increases so will the value of  $f_{knee}$ . Eventually  $f_{knee}$  will become unmeasurable. For the C11-SHIMM configuration this occurs at wind speeds greater than 10 m/s. As shown by figure 4.4 in chapter 4, 10 m/s is approximately the median wind speed of turbulent layers (at all altitudes). This limiting velocity would result in a large fraction of the possible wind speeds being unsampled. Therefore, a variation on this method was explored by acquiring the power spectrum of particular Zernike modes of the wavefront aberration, found by fitting to the WFS centroids. Utilising low order Zernike modes moves  $f_{knee}$  to lower frequencies. Whilst tip/tilt are the strongest modes, and therefore easiest to measure, they are corrupted by telescope shake and guiding errors. The next strongest and slowest atmospheric term is defocus. It is in principle angularly symmetric and is unaffected by telescope shake and guiding errors. The defocus term has been used previously by the FADE instrument to estimate  $\tau_0$  by employing a small telescope with a central obstruction to produce a ring-like defocused image. As turbulent layers traverses the telescope aperture the radius of the ring-like image will fluctuate. This fluctuation can be used to determine the defocus term. The variance of the speed of the defocus can be used to estimate  $\tau_0$ , as shown by Tokovinin et al. (2008). Here, however, the Zernike analysis is applied to the WFS centroid data.

Figure 5.16 shows example power spectra for Zernike modes  $j = 2 - 5$ , for a single simulated turbulent layer of wind speed 15 m/s. Here  $P_j^{norm}$  against  $\log(f)$  is plotted, where  $P_j^{norm}$  is defined as

$$P_j^{norm} = \frac{f \Phi_j(f)}{\int \Phi_j(f) df}. \quad (5.4)$$

Utilising this linear-log scale emphasizes the sharp localization of the energy at peak frequency ( $f_{peak}$ ) (Hogge and Butts, 1976). In addition, the area under the curve is equal to the total energy of the power spectrum (Roddier et al., 1993). The parameter  $f_{peak}$ , similar to  $f_{knee}$ , is related to the velocity by

$$f_{peak} = \gamma \frac{v}{d}, \quad (5.5)$$

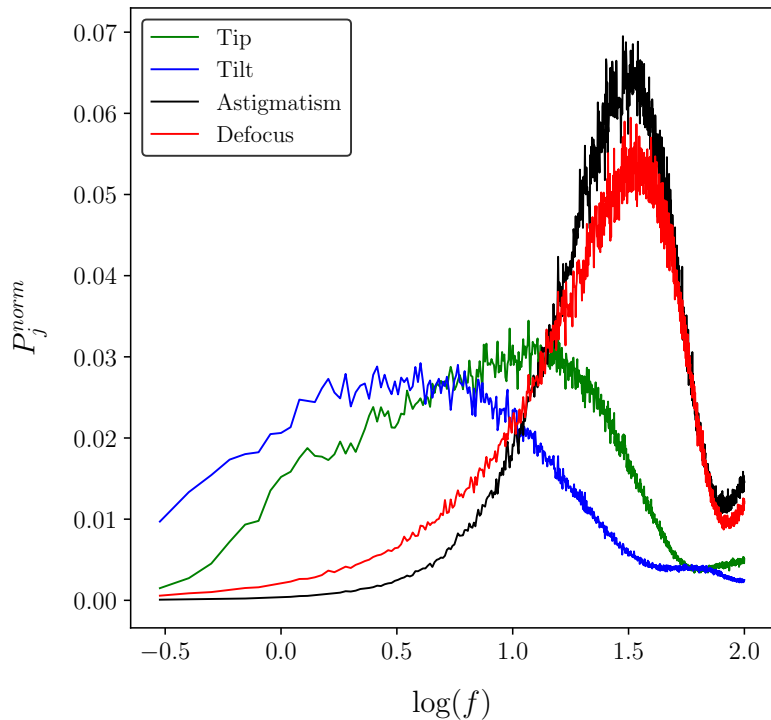


Figure 5.16: Simulated example of  $P_j^{norm}$  for a wind velocity of 15 m/s and a  $r_0$  value of 0.1 m. The coloured lines indicate different Zernike modes; green is tip ( $j = 2$ ), blue is tilt ( $j = 3$ ), red is defocus ( $j = 4$ ) and black is astigmatism ( $j = 5$ ).

where  $\gamma$  is a constant related to the WFS geometry and is determined empirically.

### 5.2.1 Single Layer

Firstly single turbulent layer profiles were used to test this method in simulation. A range of wind velocities were simulated and the corresponding  $P_{j=4}^{norm}$  were acquired. Power spectra were calculated from Zernike coefficients generated from the WFS centroids, as described in section 2.2.1.

Locating  $f_{peak}$  is required to estimate the wind speed of turbulent layers. A possible method to locate  $f_{peak}$  is to fit a single layer model, acquired from simulation, to data. This can be problematic for noisy data and when there are multiple turbulent

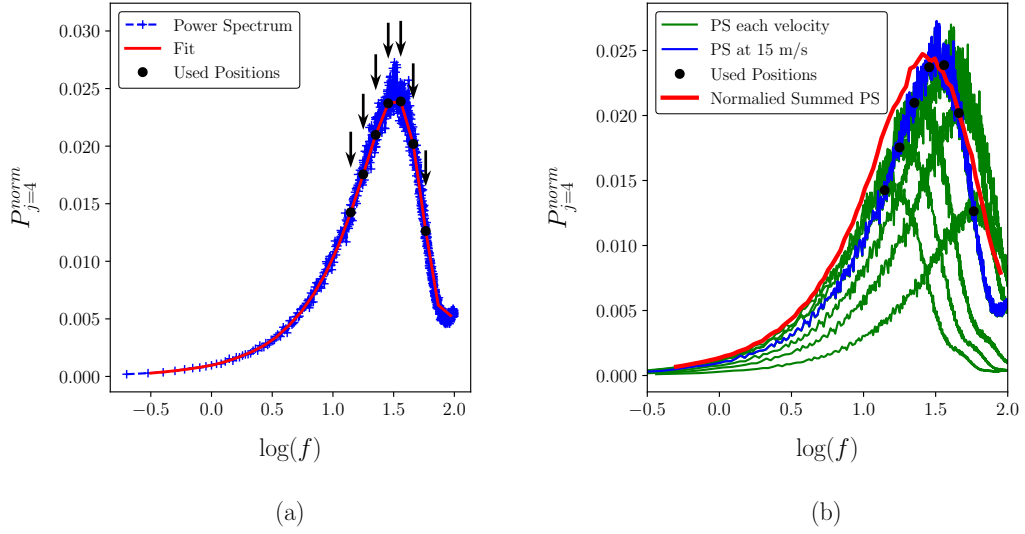


Figure 5.17: Here (a) illustrates the method for measuring the wind speed, using the C11-SHIMM configuration, an example spectrum (blue) from a single turbulent layer travelling at 15 m/s. The red line is the smoothed version of the data and the black markers indicate the sampling frequencies used for estimating the wind speed. Here (b) demonstrates how this method can be used, by assuming each marker represents a turbulent layer of particular strength and speed (green spectra). The sum of these individual spectra will form a spectrum (red) similar to the original spectrum (blue).

layers travelling at different speeds and turbulence strengths. Therefore, instead of acquiring a single peak position to calculate the velocity of the layer, many points of the spectrum are used to measure the value of  $v_{eff}$ .

This method is illustrated by figure 5.17. Figure 5.17(a) shows how the power spectrum is sampled. First the data is smoothed (depicted by the red line) by using a moving average of the power spectrum to reduce the scatter. Since there are fewer samples at low frequencies the moving average is completed in two parts for frequencies above and below  $\log(0.5)$ , where each is averaged over a different number of samples. Following this a spline interpolation is used. A number of points, in equal intervals, of the spline are found (denoted by the black arrow markers in figure 5.17(a)). These sampling points are treated as individual  $f_{peak}$ s. Each  $f_{peak}$  will correspond to a different velocity with a particular strength, therefore  $v_{eff}$  can

be found. Only sampling values above a threshold are used, to avoid the fit being biased by spurious low level features.

Figure 5.17(b) illustrates how using multiple samples (indicated by the black markers) can be used to estimate the wind speed. Each marker assumes a power spectrum of a particular strength and speed. Summing these individual spectra forms a power spectrum similar to that of the original power spectrum. This finding is exploited to provide a practical method to estimate  $v_{eff}$ . This method allows for estimating  $v_{eff}$  without needing to know how many turbulent layers are present and at what speed they are traversing the telescope aperture.

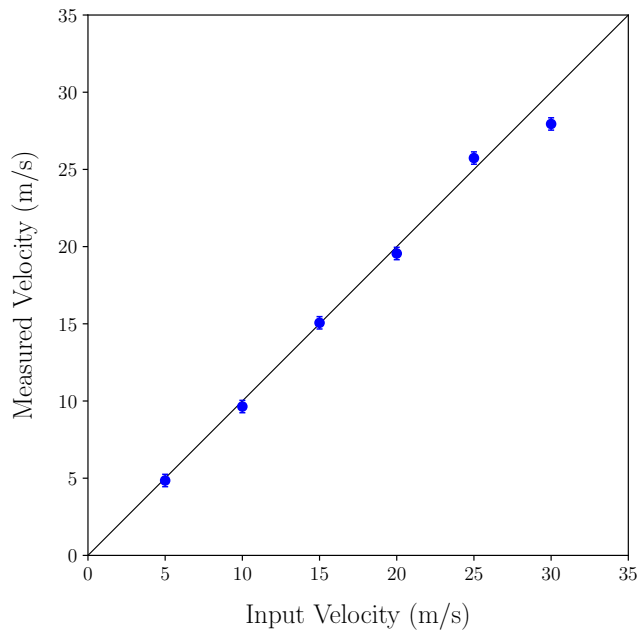


Figure 5.18: Simulated results for estimating the wind speed of a single turbulent layer with an  $r_0$  value of 0.1 m for a range of wind velocities, utilising the power spectrum method. The black line indicates  $x = y$ .

Results from simulated data are shown in figure 5.18. For wind velocities faster than 25 m/s the estimation deviates from the expected value, because the  $f_{peak}$  can no longer be sampled, and only the left side gradient of the peak is observed. The error in these values are due to the uncertainty in the interpolation given by a

weighted sum of the squared residuals of the spline approximation. An investigation was made into the effects of different wind directions. It was found that the output remained unchanged.

## 5.2.2 Two Layers

Optical turbulence profiles with more than one layer will produce spectra with multiple peaks, each corresponding to a different layer. Measuring the amplitude of these peaks will produce the relative strengths of each layer. With the relative strengths and the position of the peaks,  $v_{eff}$  can be estimated. The same method described above, and illustrated in figure 5.19(a), was used to produce the results shown in figure 5.19(b).

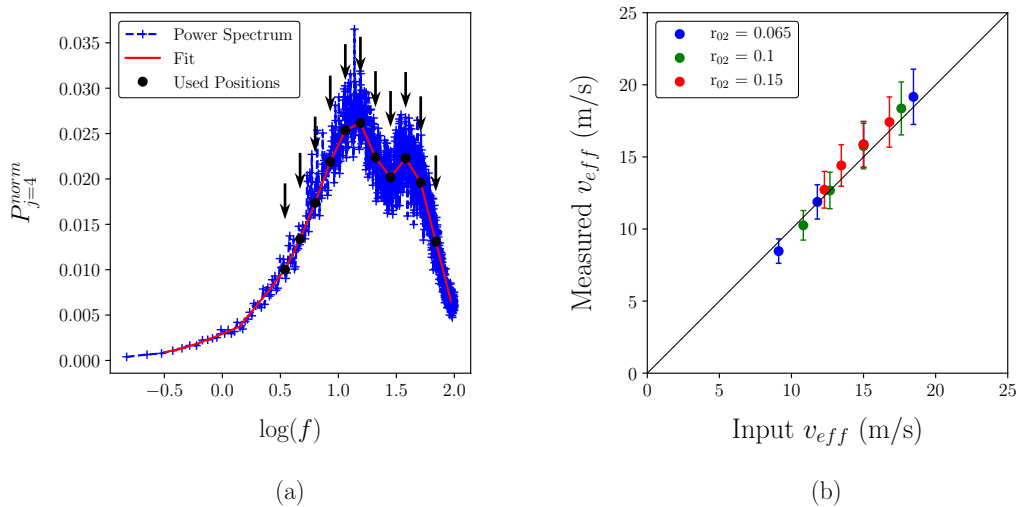


Figure 5.19: Here (a) illustrates the method for measuring the wind speed for an example spectrum (blue) from a two turbulent layer profile travelling at 5 and 15 m/s, of equal strengths. The red line is the fit and the black markers indicate the sampled frequencies used for estimating the wind speed. Here (b) shows simulated results for estimating the wind speed of a two turbulent layer profile. One layer is travelling at 15 m/s with a  $r_0$  value of 0.1 m. The second layer was travelling at a range of values between 5 – 20 m/s with  $r_0$  values of 0.065 m (blue), 0.1 m (green) and 0.15 m (red). The black line indicates  $x = y$ .

The simulated results indicate that this method works for velocity profiles with wind speeds less than 25 m/s. In order to measure faster layers either a detector with a faster frame rate is required or a larger telescope aperture. However, results from Stereo-SCIDAR, at La Palma and Paranal, show that turbulence wind speeds greater than 25 m/s occur only  $\sim 7\%$  of the time, as shown by figure 4.4, in section 4.1.

## 5.3 On-Sky Results

In this section on-sky results taken by the C11-SHIMM will be presented. These observations took place in July 2016 and September 2016 at the ING site in La Palma. The C11-SHIMM was positioned on the WHT roof. For details of the observations see table 4.2 in section 4.5.

### 5.3.1 Data Reduction

The first two stages of data reduction; data quality control and centroiding, are described in chapter 5 section 4.3. However, some considerations needed to be made for acquiring power spectra. If saturated pixels are present the frame can not be simply deleted since the correct time intervals are required for the temporal offsets. Instead, all centroids of saturated frames are set to zero so that the frame can be easily located and the correct temporal offsets can be achieved. Under strong scintillation it is possible for subapertures of random frames to have too weak a signal. In this case, the centroid value is set to zero. If this occurs for more than 10% of frames the dataset is considered unusable. Setting the centroid value to zero can result in additional noise at high frequencies. However by using multiple datasets for a single measurement of  $\tau_0$ , this effect should average out.

### 5.3.2 Results

Figure 5.20 displays example power spectra obtained from on-sky data. Here, four contrasting cases will be discussed.

**Case 1 ( $v < 25$  m/s):** Figures 5.20(a) - (c) illustrate examples where all turbulent layers traverse the telescope apertures at wind speeds less than 25 m/s. In this case the power spectrum method works the most reliably. This is because the peaks that are formed are fully observed, as indicated by the negative gradient of the power spectra at higher frequencies. This is unlike the turbulent layers present in figures 5.20(d) - (f) which are partially cut by the maximum frequency value.

**Case 2 ( $v < 1.5$  m/s):** Figures 5.20(c) and (e) show examples of very slow moving turbulent layers. The method for measuring  $v_{eff}$  still works in this case, however it is possible that these layers result from turbulence local to the SHIMM instrument. This turbulence would not necessarily also be seen by a nearby large astronomical telescope. The C11-SHIMM was located on the roof of the WHT, this means that that the instrument was not in an open space. The building structure could induce local turbulence from wind shear caused by building structure and heat radiated from the building.

**Case 3 ( $v > 25$  m/s):** As described in section 5.2.1 wind speeds greater than 25 m/s can not be measured accurately, with the current C11-SHIMM configuration. Figures 5.20(d) and (e) are examples of turbulent profiles with multiple strong wind speeds present. In these cases the power at high frequencies is due to a fast moving turbulent layer with a velocity which has a peak frequency that can not be sampled. The last few points of the interpolation indicate the gradient of the power at high frequencies. If it is positive that means the true value of  $v_{eff}$  is likely to be greater than that which is reported. As a result, the system reports this case when the estimate of  $v_{eff}$  is produced.

**Case 4 ( $v > 30$  m/s):** Figure 5.20(f) is an example of a turbulence profile which appears to be dominated by a turbulent layer faster than 30 m/s. However, it was found that this power spectrum occurs when the data becomes shot noise dominated. This will be further discussed in this section.

Figure 5.21 shows the estimated values of  $v_{eff}$  from on-sky data taken by the C11-SHIMM. The two histograms in each sub-figure show results for: all estimated values of  $v_{eff}$  and case 1, when all turbulent layers have a wind speed less than 25 m/s. The mean value of  $v_{eff}$  for case 1 and case 3 (i.e. where at least one turbulent layer has a wind speed greater than 25 m/s) in figure 5.21(a) is 11 m/s and 25 m/s respectively. The histogram of all the estimated  $v_{eff}$  values produce a bimodal results, which is unexpected. Figure 5.22 displays histograms of  $v_{eff}$  measured at La Palma and Paranal over a series of nights by Stereo-SCIDAR. The C11-SHIMM estimates a much larger proportion of its results to be above 20 m/s compared to Stereo-SCIDAR.

The reason for this is due to the SNR of the data. Figure 5.23 illustrates the effects of shot noise on the defocus power spectrum. In simulation, shot noise was added to a diffraction limited spot image, so as to only test the effects of shot noise and not atmospheric changes. It can be seen that the shot noise in the image results in an increased intensity at higher frequencies. In terms of the measurement of  $v_{eff}$ , this results in the incorrect measurement of a single fast turbulent layers.

Figure 5.21(b) shows results when only targets brighter than second magnitude were observed. It can be seen that whilst the histogram from case 1 remains almost unchanged, the histogram displaying all data shifts to values much more comparable with Stereo-SCIDAR.

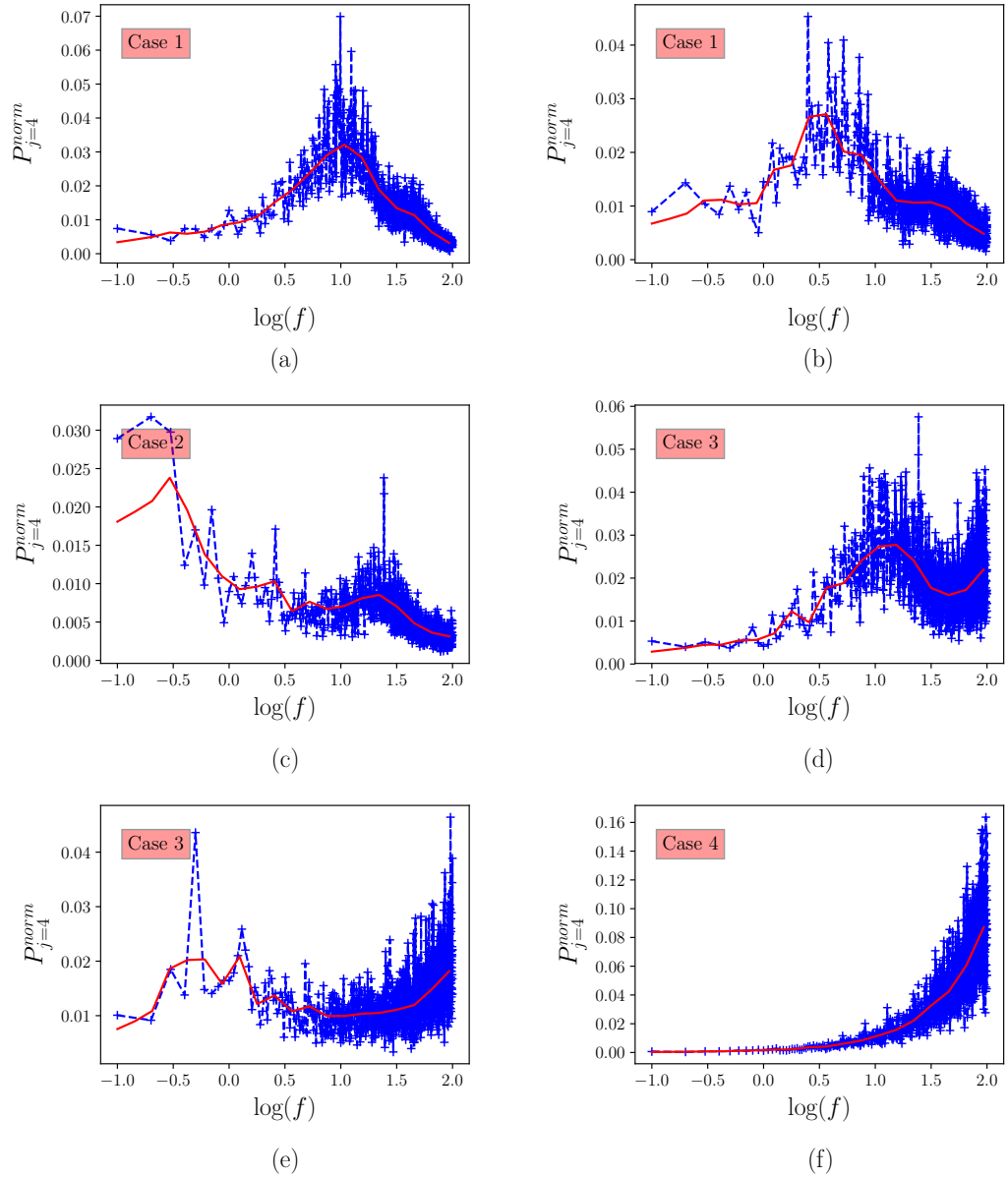


Figure 5.20: Example power spectra of the defocus term of on-sky data taken with the C11-SHIMM at the INT site, La Palma, showing the four cases. The blue line depicts the raw power spectra data, the red line displays the interpolated fit used to calculate the  $v_{eff}$ .

By comparing figures 5.21(b) and 5.22 it can be seen that the C11-SHIMM observed a higher frequency of turbulent layers slower than 5 m/s i.e. case 2. By comparing local wind speeds measured at the WHT (provided by the public WHT archives (Sorensen and Mendez, 2002)) it was found that all measured values of  $v_{eff}$  less than 5 m/s corresponded to periods when the local wind speeds were less than 5 m/s. It is possible that it would be beneficial to threshold the minimum wind speed of turbulent layers that are used when estimating  $v_{eff}$  so as not to include a bias due to slow local wind speeds. Figures 5.21(c) and (d) shows histograms with different thresholds at  $\log(f) = 0.0$  and  $0.5$ , corresponding to wind speeds of  $\sim 0.5$  and  $1.5$  m/s. As expected these thresholds result in the mean of the histograms shifting to larger values of  $v_{eff}$ . The summation of the histograms in figure 5.21(d) becomes bimodal again. Therefore, it is perhaps beneficial to only threshold for wind speeds faster than  $0.5$  m/s. More observations are required at all times of the year to see if the results from C11-SHIMM will agree with Stereo-SCIDAR for a statistically large dataset.

Figure 5.24 illustrates a histogram of  $\tau_0$  obtained by the C11-SHIMM on La Palma for target stars brighter than second magnitude. The median value of  $\tau_0$  for case 1 and case 3 is  $4.1$  and  $1.9$  ms respectively. Case 1, when all turbulent layers are less than  $25$  m/s shows a good agreement with the results obtained by Stereo-SCIDAR on La Palma which has a median  $\tau_0$  value of  $4.4$  ms, shown in figure 5.25.

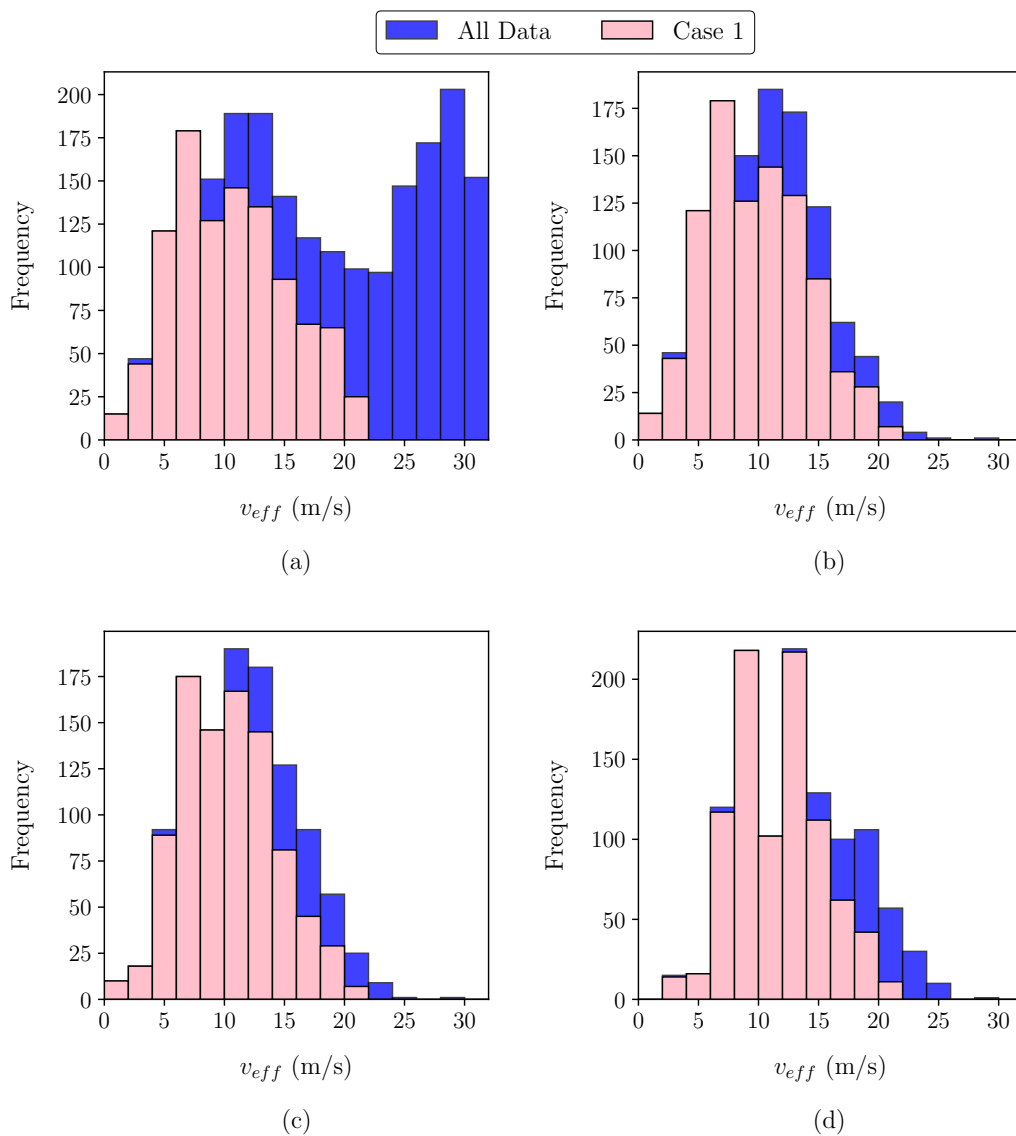


Figure 5.21: Histogram of  $v_{eff}$  estimates obtained from on-sky results by the C11-SHIMM. The blue histograms indicate all results. The pink histograms indicate results where all measured turbulent layers were slower than 25 m/s (case 1). The sub-figures display results for: all data (a); data with signal to noise considerations i.e. when the observed target was of second magnitude or brighter (b); and data with noise considerations and velocities less than 0.5 m/s (c) and 1.5 m/s (d) were excluded from the calculation of  $v_{eff}$ .

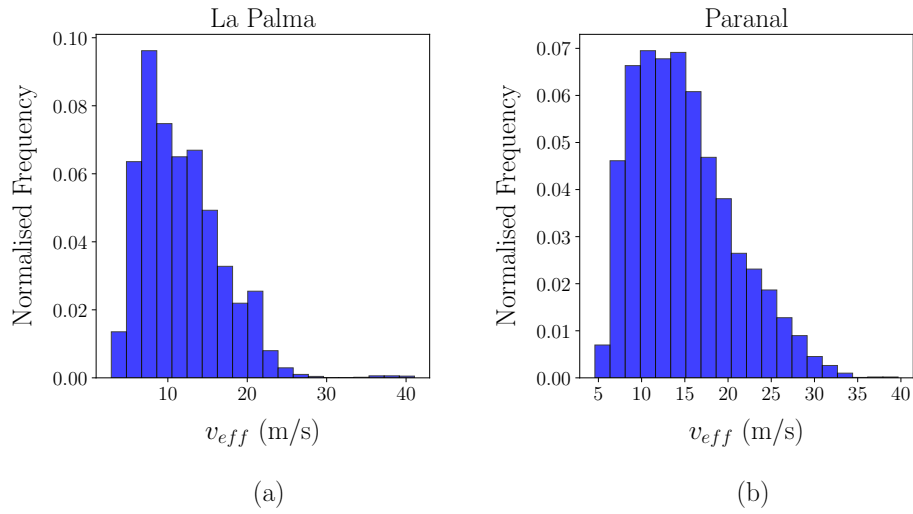


Figure 5.22: Histogram of the  $v_{eff}$  measured by the Stereo-SCIDAR taken from two different observing sites mounted on the INT at La Palma (a) and onto an AT of the VLT at Paranal (b) over a range of nights.

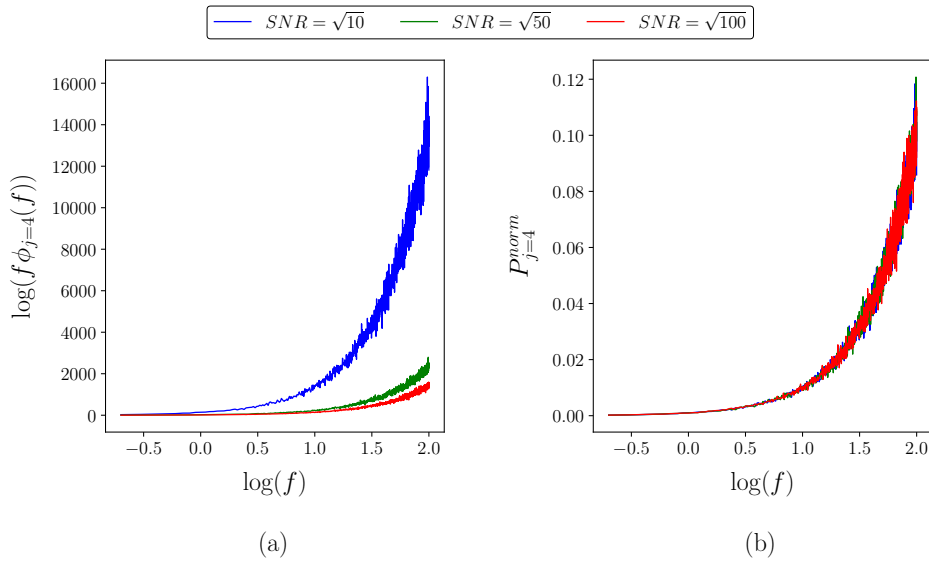


Figure 5.23: Power spectra of the defocus Zernike term from simulated diffraction limited data for a range of shot noise values. The results show that the presence of shot noise results in increase in power for higher frequencies. (a) Shows that for increasing values of the SNR of an image the power at high frequencies decrease. (b) Shows the normalised power spectra  $P_{j=4}^{norm}$ , as expected they are the same for all SNR values.

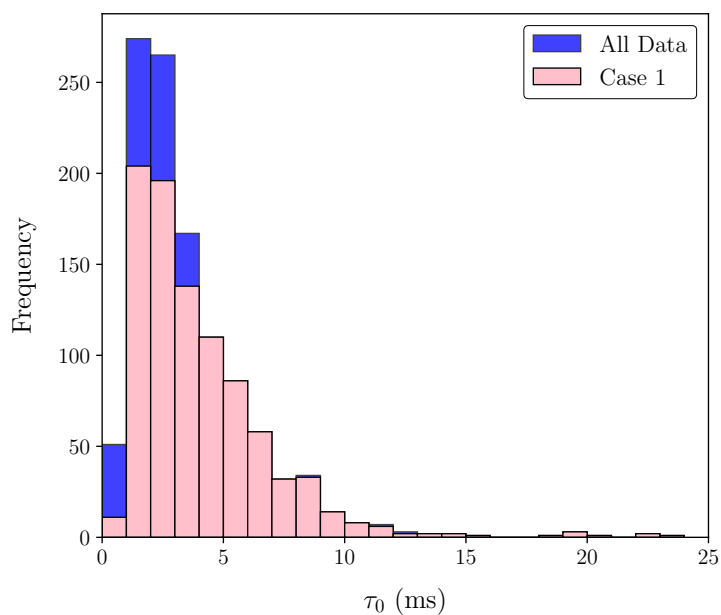


Figure 5.24: Histogram of  $\tau_0$  measurements obtained on-sky by the C11-SHIMM when observing targets brighter than second magnitude. The blue histogram indicate all estimated values of  $\tau_0$ . The pink histogram indicate results where all measured turbulent layers were slower than 25 m/s (as described by case 1).

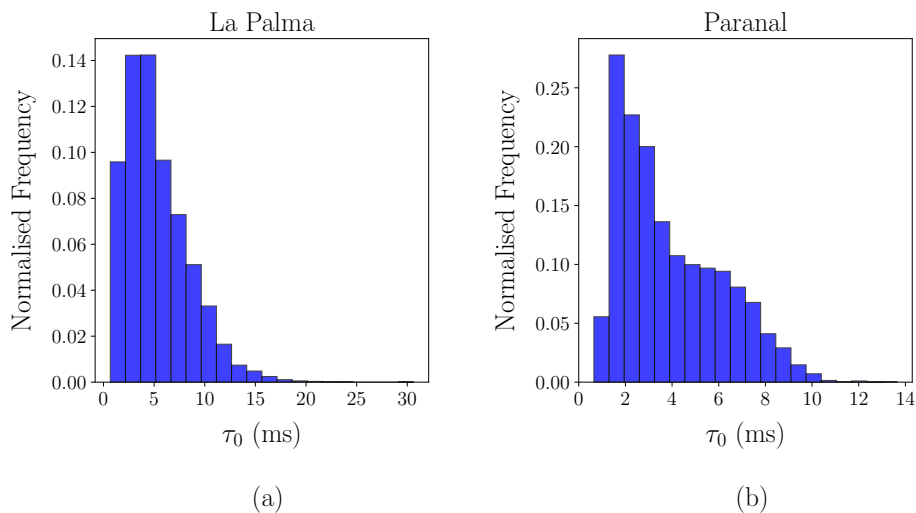


Figure 5.25: Histogram of  $\tau_0$  measured by the Stereo-SCIDAR taken from two different observing sites mounted on the INT at La Palma (a) and onto an AT of the VLT at Paranal (b) over a range of nights.

### 5.3.3 Limitations & Noise

There are three key limitations in the measurement of  $\tau_0$  by the SHIMM: the maximum measurable velocity, the effect of slow moving turbulent layers and shot noise. The current C11-SHIMM configuration cannot measure velocities greater than 25 m/s (however the presence of high wind speeds can potentially be identified). This is specific to this configuration, i.e. a larger telescope aperture or faster frame rate camera could be employed.

As described in the previous section it is not possible to distinguish slow turbulent layers in the free atmosphere from turbulence local to the instrument itself. The effects of local turbulence can be reduced by placing the SHIMM on a tower, uninhibited by close local building structures and heat.

In the previous section the effects of shot noise on power spectra was discussed. It can be seen that this effect can be detrimental to estimating  $v_{eff}$  (and therefore  $\tau_0$ ). By observing target stars brighter than second magnitude this effect can be avoided. During these observations the C11-SHIMM configuration was observing on the same telescope as the Full Aperture Seeing Sensor (FASS) (described in the next chapter) by utilising a beamsplitter. This reduced the amount of light received by the SHIMM and therefore limited the magnitude of the star that could be used. When the C11-SHIMM is operating alone it should be able to use fainter targets. Another source of noise is statistical noise which can be reduced by averaging more datasets. Typically data is averaged for between one and five minutes. Averaging over longer periods is problematic since the atmospheric turbulence profile is likely to evolve significantly.

In calculating  $\tau_0$  the sources of error are from the estimation of  $r_0$  and  $v_{eff}$ . The uncertainty in  $r_0$  has been discussed in the previous chapter. Assuming no systematic bias in the centroiding procedure, the uncertainty in calculating  $v_{eff}$  originates from the method of reducing the power spectra. There are two stages in reducing the power spectra, the moving average and the interpolation. The uncertainty in

the points of the moving average is found from the standard error of the number-point average. The uncertainty in the interpolation is given from the weighted sum of the squared residuals of the spline approximation. The propagation of these errors through to the calculation of  $v_{eff}$  delivers an uncertainty in the measurement of  $v_{eff}$ .

## 5.4 Conclusion & Future Work

In this chapter two methods for estimating  $\tau_0$  has been presented; the covariance map method and the power spectrum method. It was found that the covariance map method can not be used for small telescopes affected by telescope shake and telescope guiding errors. However, it can serve as a graphical demonstration of the wind velocities of dominant turbulent layers.

The defocus power spectrum method can be used to estimate the value of  $\tau_0$  by estimating the value of  $v_{eff}$ . The method itself has no limitations in estimating  $\tau_0$ . However, with the current C11-SHIMM configuration only turbulent layers with wind speeds below 25 m/s can be accurately measured. In order to measure faster wind speeds either a larger telescope aperture or a detector with a faster frame rate is required.

In order to confirm this method, concurrent measurements of  $\tau_0$  with turbulence profilers such as Stereo-SCIDAR or SLODAR would be beneficial. An extended campaign of observations is planned at Paranal observatory in 2017/2018 as will be described in the next chapter. This campaign is for the combined instrument FASS-SHIMM. The FASS is capable of measuring wind speeds of high altitude layers (Guesalaga et al., 2016). The FASS is unable to observe turbulent layers below 400 m, therefore the FASS and SHIMM will estimate different values for  $\tau_0$ . However, it will be beneficial to compare whether the turbulent layers present at higher altitudes, observed by FASS, are apparent in the power spectra obtained by the C11-SHIMM.

---

# SHIMM: Optical Turbulence Profile and Correction of Seeing Measurements for Scintillation

Scintillation of the light from a target star, due to high altitude turbulence, can cause an over- or underestimation of the measured value of  $r_0$  in seeing monitors and profiling instruments, such as the DIMM and MASS respectively (Tokovinin and Kornilov, 2007), as described in sections 3.2 and 3.3. This effect is also relevant for the SHIMM, since like the DIMM, it will overestimate the value of  $r_0$  in the presence of scintillation. The SHIMM software can correct for the effect of scintillation on  $r_0$  by extracting intensity information from the WFS spots. The measured scintillation index together with the correlation of the scintillation between neighbouring subapertures can be used to estimate the vertical profile of the turbulence and thus correct the measured value of  $r_0$ . By fitting a model to this scintillation information and the measured  $r_0$  a fixed three layer turbulence profile can be estimated. In this instance a model defined by turbulent layers at 0, 5, and 15 km is used. Whilst this does not give high resolution information it does, for example, notify the SHIMM user as to whether the profile is dominated by a ground layer or higher altitude turbulence. This information is important for site characterisation and

queue scheduling. As described in section 2.2.2, strong high altitude turbulence causes scintillation noise that can be detrimental to high precision photometry. Whereas, strong ground layer turbulence will effect direct imaging and may require ground layer AO. The ability to estimate the turbulence profile provides a distinct advantage over the traditional DIMM design, which only measures the total integrated seeing.

The method of using scintillation correlations has been employed by the optical turbulence profiler CO-SLIDAR, which was based on a large telescope ( $\sim 1.5$  m). CO-SLIDAR utilises a SHWFS to measure the wavefront slopes as explained in section 3.1 and 3.4. In addition, it obtains scintillation information by summing the pixel intensity for each subaperture in the focal plane (Robert et al., 2008). The measurement of slope correlations between the two stars allows the instrument to be sensitive to low altitude turbulence, in a method similar to that of SLODAR. Scintillation correlations and correlations between slopes and scintillation deliver high-altitude layer sensitivity (Robert et al., 2011).

In this chapter the effect of scintillation on the estimated value of  $r_0$  will be demonstrated. The correction of  $r_0$  for the SHIMM will be addressed, as well as a method for estimating a three layer optical turbulence profile. Simulated and on-sky data will be presented for the C11-SHIMM, including comparisons with Stereo-SCIDAR data.

This chapter will also introduce the concept of the FASS instrument. The FASS instrument has been developed in collaboration with Pontifical Catholic University of Chile (PUC), Chile. The concept and analysis was developed by Andrés Guesalaga at PUC, and the design, manufacturing and testing was completed at Durham University.

The FASS is based on the same principle as the MASS instrument, but utilises the full aperture of the telescope and exploits an Electron-Multiplying CCD (EMCCD) instead of PMTs. An EMCCD is employed instead of a CCD since it combines

low detection limits with high frame rates (O’Grady, 2006). The EMCCD is a device that works on the principal of impact ionization, where extra electrons are produced and transferred to the next pixel (Basden, 2015). This amplification (EMgain) occurs before the readout and as a result the signal can be amplified above the readout noise.

These modifications provide advantages in the manufacturing and maintenance of the FASS, relative to the MASS, as it is comprised of entirely off-the-shelf components. In addition, it can produce a profile with a much higher vertical resolution. As described in section 3.3, the MASS generates a six layer turbulence profile, whereas the FASS can provide as many as 17 layers when mounted on a telescope of aperture size 9.25 inches.

The FASS instrument was combined with the SHIMM to make the FASS-SHIMM, by employing a dichroic beamsplitter to pass red and blue light to the FASS and SHIMM optics respectively. The purpose of combining these instruments is two fold. The FASS detector is placed at the optical conjugate plane of the telescope aperture. Scintillation is therefore only detected for turbulent layers higher than  $\sim 400$  m, i.e. layers for which there is a significant propagation distance to the telescope pupil. Hence, the ground layer of turbulence is not directly measured by the FASS. However, when the FASS is operated in parallel with the SHIMM the ground layer can be determined from the difference of the total seeing measured by the SHIMM and the integral of the FASS turbulence profile. The SHIMM also provides autoguiding for the combined system. Pointing offsets cannot be determined from the (pupil conjugated) FASS images. These are essentially the same advantages obtained for the current combined MASS-DIMM instrument.

In this chapter the principles and implementation of the FASS-SHIMM instrument will be described, including preliminary on-sky results.

## 6.1 Effects of Scintillation

The effects of scintillation on the measured  $r_0$  value for the DIMM has been discussed in Tokovinin and Kornilov (2007). The main effect is shown by figure 6.1(a). Simulations were made for a range of  $r_0$  values over propagation distances of 0 to 16 km for the C11-SHIMM WFS geometry (see figure 5.1 in section 5.3). It can be seen that as the propagation distance increases, so does the measured value of  $r_0$ . This effect is due to the increase in the amount of scintillation with propagation distance, as depicted by figure 6.1(d).

The presence of scintillation results in a change in the shape of the auto-covariance map generated by a set of WFS spots (see section 4.3). This effect is discussed for the SLODAR instrument in Goodwin et al. (2007). Figure 6.2 illustrates this effect by taking a 1-D slice from an auto-covariance map, generated from simulated data for the C11-SHIMM configuration, for a range of propagation distances. As the propagation distance increases the shape of the auto-covariance slice changes, with the peak value decreasing and the ‘wings’ of the slice increasing. As a result, the fit used to estimate the value of  $r_0$  no longer holds, resulting in an incorrect estimate of  $r_0$ , as shown by figure 6.1(a).

Figure 6.1(b) illustrates that this effect gets worse as  $r_0$  decreases, i.e. for stronger turbulence. The overestimation in  $r_0$  can be substantial, with differences as large as 60% in the value of  $r_0$ , for the examples shown in figure 6.1.

From figure 6.1(a) it can be seen that it is not possible to distinguish whether a measured value of  $r_0$  results from a relatively strong but high altitude layer or a weaker low altitude layer. For example, a measured  $r_0$  of 0.1 m could be due to a turbulent layer at the ground with  $r_0 = 0.1$  m or a turbulent layer at 16 km altitude with  $r_0 = 0.065$  m. Therefore the scintillation index and correlation of the scintillation of neighbouring subapertures are used to distinguish between these scenarios. The scintillation index,  $\sigma_I^2$ , is calculated using equation 2.21. The

correlation is given as

$$Corr = \frac{A \times B}{\sqrt{A^2 \times B^2}}, \quad (6.1)$$

where  $A$  and  $B$  are given by

$$A = (I_A - \langle I_A \rangle), \quad (6.2)$$

$$B = (I_B - \langle I_B \rangle), \quad (6.3)$$

and  $I$  is the time-varying intensity of a single subaperture  $A$  or  $B$ . Figure 6.1(c) and (d) show how the correlation and scintillation index increase with propagation distance for different  $r_0$  values. The correlation values are calculated by averaging the correlation of all instances where  $A$  and  $B$  are subapertures with an adjacent separation of one in either the x or y direction. For example, in the case of the C11-SHIMM configuration there are 12 possible combinations in the x direction and 12 combinations in the y direction. It is important to note that in this chapter simulations were conducted without additional noise, such as shot noise. Therefore, all error bars shown on results from simulated data is due to error propagation of the statistical uncertainty of the simulation. This uncertainty is reduced by a factor of  $1/\sqrt{N}$ , where  $N$  is the number of runs of a simulation, as according to the standard error. If the error bars are not visible on the plot it can be assumed that they are too small to be observed, unless otherwise stated.

Correcting for the effects of scintillation is important to produce an accurate estimation of  $r_0$ . This will first be addressed for a single layer turbulence profile to illustrate how the measured value of  $r_0$  can be corrected for scintillation in the most simple case. This method will then be discussed for increasingly complex profiles of two and three turbulent layers. Finally, it will be shown how using three unknown parameters,  $r_0$ ,  $\sigma_I^2$  and  $Corr$  can be used to estimate a turbulence profile at fitted altitudes of 0, 5 and 15 km.

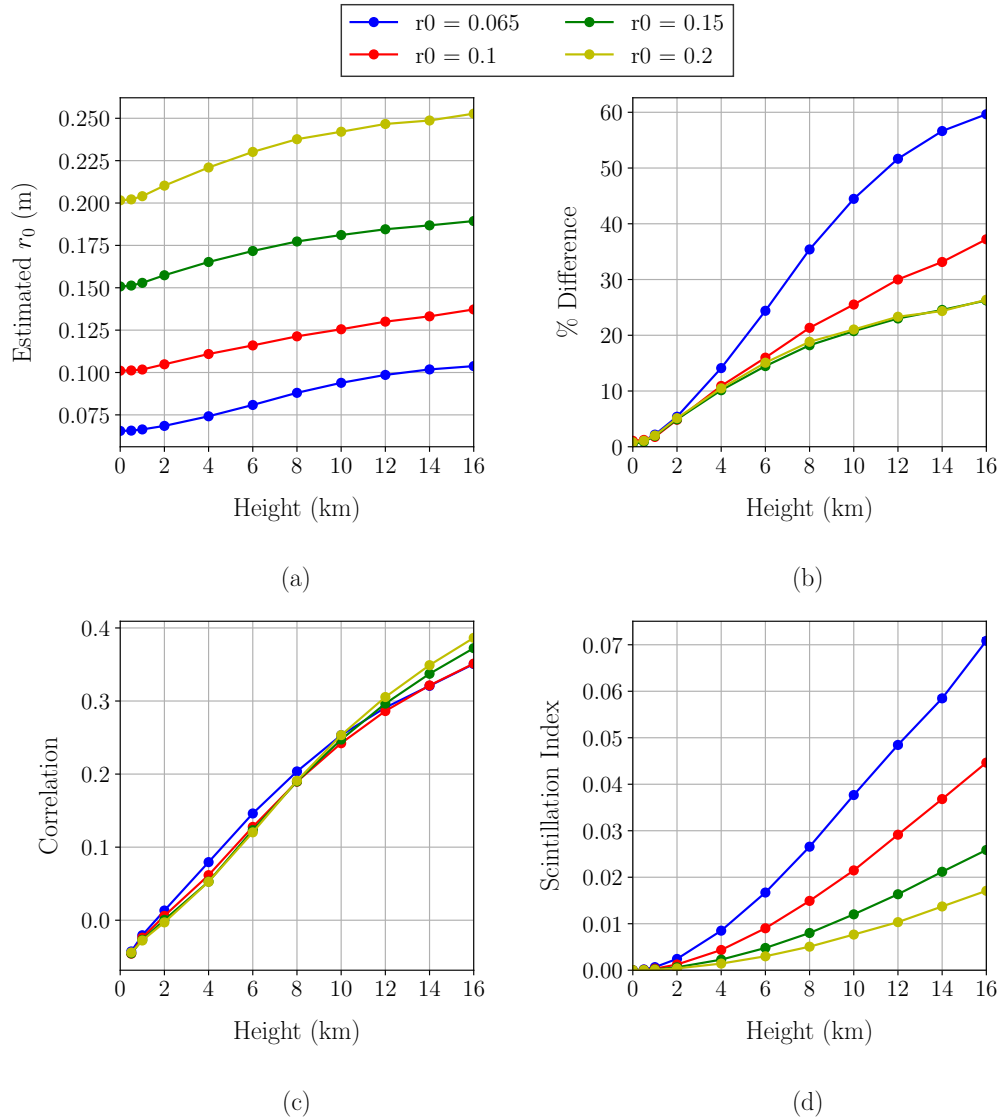


Figure 6.1: Simulated results for  $r_0$  values of 0.065, 0.1, 0.15 and 0.2 m depicted by the blue, red, green and yellow block lines respectively, for the WFS configuration of the C11-SHIMM. Here (a) shows how the estimated  $r_0$  increases with propagation height, (b) illustrates how the percentage difference of the measured and real  $r_0$  increases with decreasing  $r_0$  values (c) demonstrates the relationship between correlation between the intensities of neighbouring subapertures and propagation distance, and (d) shows how the scintillation index increases with height.

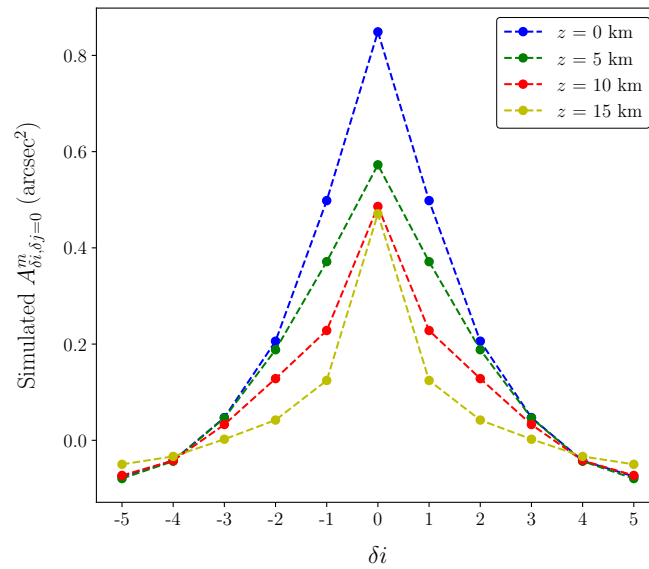


Figure 6.2: Simulated results showing a 1-D slice taken from an auto-covariance map produced by y centroids for a range of propagation distances,  $z = 0$  km (blue), 5 km (green), 10 km (red) and 15 km (yellow). The 1-D slice is taken for when the subaperture separations are in the y direction, with respect to the WFS is zero i.e.  $\delta j = 0$ . Increasing the propagation distance changes the shape of the auto-covariance slice, which results in an incorrect estimate of  $r_0$ .

## 6.2 Single Layer Turbulence Profiles

Two methods were investigated for correcting the effects of scintillation on  $r_0$  measurements for a single turbulent layer. This makes the assumption that all the atmospheric turbulence is represented by a single layer. The first method works by interpolating values from figures 6.1(c) and (d). The second method uses a model to form a reference look-up table. Both methods and their validity will be discussed.

### 6.2.1 Interpolation

Figure 6.1(c) shows that the correlation of scintillation is approximately independent of  $r_0$ . With this assumption it is possible to estimate the propagation distance for a single turbulent layer by using a spline interpolation. Once the altitude is known then the value of  $r_0$  can be determined from figure 6.1(d) using a further interpolation, for a given measured scintillation index value. Figure 6.3 displays simulated results of the percentage difference of the measured and input  $r_0$  before and after scintillation correction.

It can be seen that this method for correcting the effects of scintillation does not always produce accurate results, since large percentage differences are still present in some cases. This is because the assumption that the correlation is independent of  $r_0$  is not sufficiently accurate. For example, by referring to figure 6.1(c), a correlation of 0.1 can result from turbulence at a range of altitudes, approximately  $\pm 0.5$  km. This can lead to a range of possible  $r_0$  values for a given scintillation index value, resulting in a wrong correction. In the cases where  $r_0$  is larger than 0.1 m, the corrections give a substantial improvement on the accuracy of the measured  $r_0$  value.

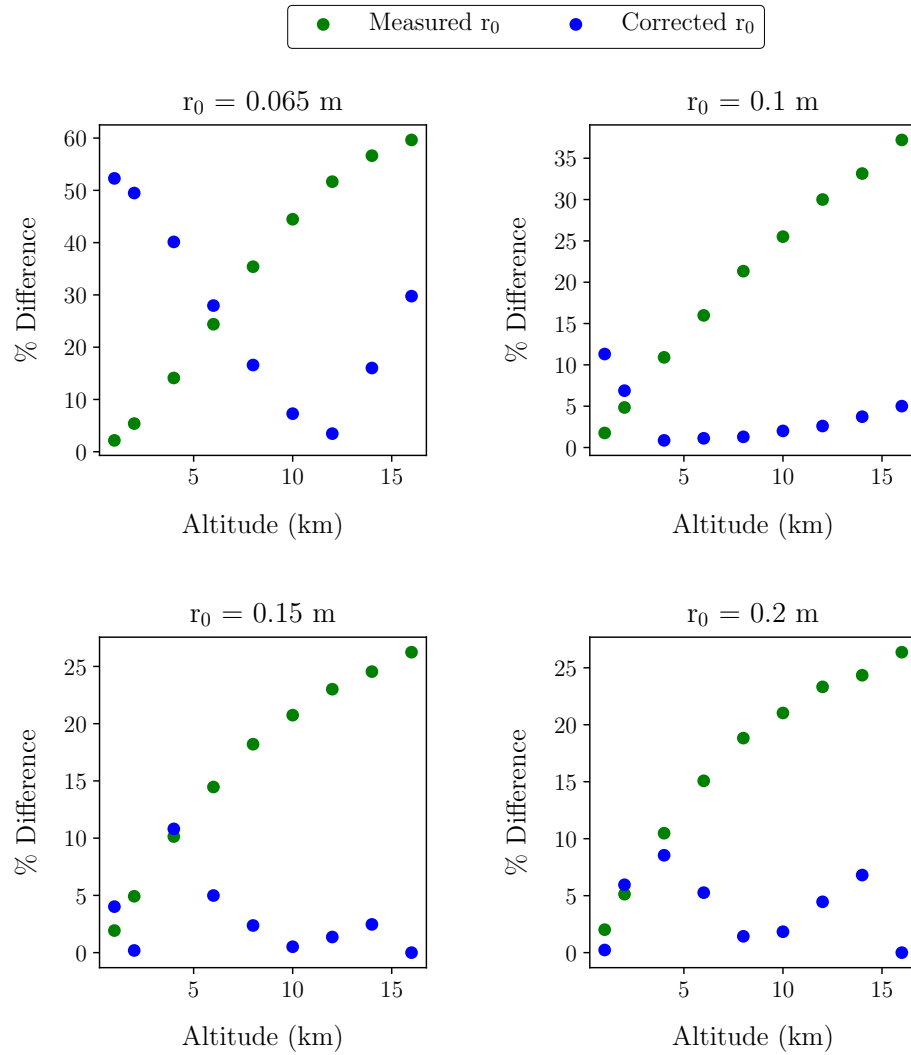


Figure 6.3: Simulated results for the C11-SHIMM configuration showing the percentage difference between a measured and input  $r_0$  before (green) and after (blue)  $r_0$  correction for scintillation. The error bars are too small to plot.

## 6.2.2 Model

Figure 6.1(b) and (c) show that a given combination of the scintillation index and correlations are unique to a specific value of  $r_0$ . The model method uses a detailed reference look-up table listing different values of  $r_0$  and their corresponding

scintillation information parameters. Since no two values of  $r_0$  will produce the same scintillation parameters a least squares fit can be used to find an optimum propagation distance and a value of  $r_0$ , with the smallest residual.

The simulated results for this method are shown in figure 6.4, with the estimated value for  $r_0$  before and after correction versus the input value of  $r_0$ . The circular markers refer to turbulent layers propagating from different altitudes to the ground, for a range of  $r_0$  values. The errors in the corrected values originate from the residual of the fit of the reference look-up table to the measured parameters. It can be seen that after correction the value for  $r_0$  is in much better agreement with the input  $r_0$  values, and agree within the estimated uncertainty.

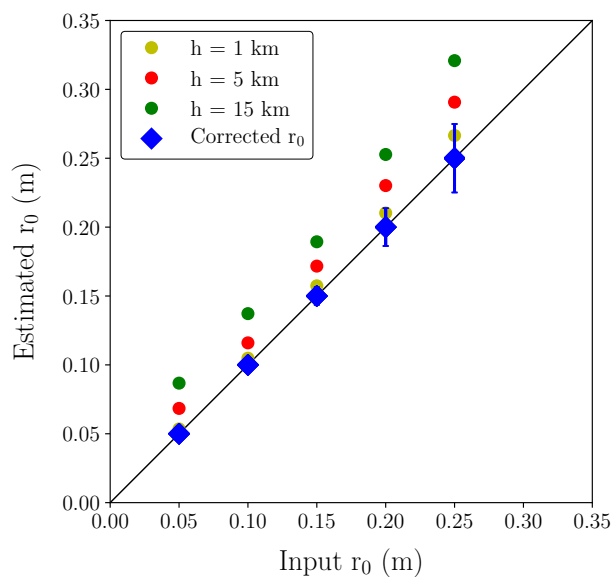


Figure 6.4: Example of simulated results for the C11-SHIMM configuration showing the measured  $r_0$  versus the input  $r_0$  before (circle markers) and after (blue diamond)  $r_0$  correction for scintillation by utilising the reference look up table. The circular markers refer to the turbulent layers at altitudes of 1 km (yellow), 5 km (red) and 15 km (green).

## 6.3 Two Layer Turbulence Profiles

In this section, a two layer atmosphere will be considered. The first layer will be fixed at the pupil plane (altitude 0 km) and a second ‘floating’ layer at varying altitudes,  $h_2$ , above the pupil plane. These multi-layer profiles have been simulated as described in section 2.3.2. Turbulence at a propagation distance of 0 km i.e. at the pupil plane will not induce intensity variations. Therefore, for a profile with turbulence at the ground and at altitude  $h_2$ , figure 6.1(c) and (d) will remain unchanged. However, for a two layer profile the measured  $r_0$  value will change as follows

$$r_0^{-\frac{5}{3}} = r_{01}^{-\frac{5}{3}} + r_{02}^{-\frac{5}{3}}, \quad (6.4)$$

where the subscript 1 and 2 refer to the turbulent layers at altitudes 0 km and  $h_2$  respectively. Since  $r_0$  relates to  $C_n^2$ , according to equation 2.8, this becomes

$$C_n^2 = C_{n_1}^2(h_1) + C_{n_2}^2(h_2). \quad (6.5)$$

Since the propagation distance changes the measured value of  $C_n^2$  at the ground, by  $\Delta C_n^2$ , the overall measured turbulence strength will change as follows

$$\begin{aligned} C_{n_m}^2 &= C_n^2 + \Delta C_n^2 \\ C_n^2 + \Delta C_n^2 &= C_{n_1}^2(h_1) + \Delta C_{n_1}^2(h_1) + C_{n_2}^2(h_2) + \Delta C_{n_2}^2(h_2) \end{aligned} \quad (6.6)$$

where  $\Delta$  refers to the change in the turbulence strength through propagation. Since the first layer is at the ground  $\Delta C_{n_1}^2(h_1) = 0$ , resulting in  $\Delta C_n^2 = \Delta C_{n_2}^2(h_2)$  i.e. the change in the measured turbulence strength at the ground will be equal to the change in the turbulence strength incurred by the propagation of the turbulent layer at  $h_2$ . Therefore,  $C_{n_m}^2$  can easily be corrected by adopting the method described in section 6.2.2 by using the scintillation information to find  $C_{n_2}^2(h_2)$  and the associated propagation distance. With this information  $\Delta C_{n_2}^2(h_2)$  can be estimated and subtracted from  $C_{n_m}^2$ .

Figure 6.5 displays simulated results of input  $r_0$  values versus measured  $r_0$  before and after correcting the effects of scintillation. The turbulence profiles consist of

two turbulent layers at 0 km and  $h_2$  for a range of values of  $r_0$ . It can be seen that this method works well, as the corrected values are all equal to the input values within the uncertainty.

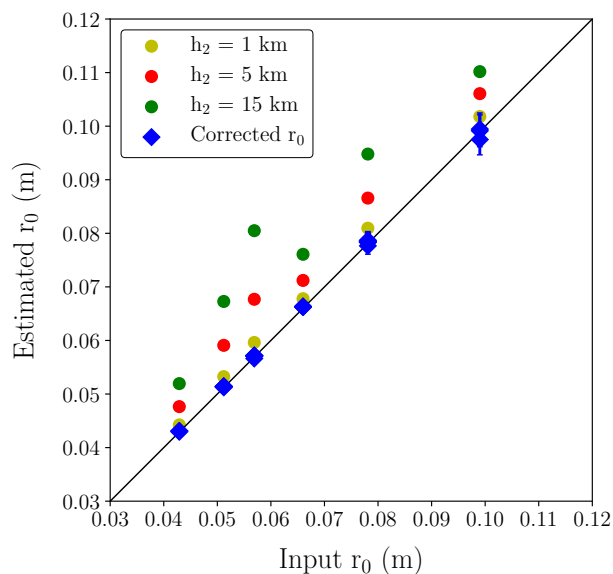


Figure 6.5: Example of simulated results for the C11-SHIMM configuration, showing the measured  $r_0$  versus the input  $r_0$  before (circle markers) and after (blue diamond)  $r_0$  correction for scintillation by utilising the reference look up table. The turbulence profiles consisted of two turbulent layers, at altitude 0 km and at  $h_2$ . The circular markers refer to the turbulent layers at altitudes  $h_2$  of 1 km (yellow), 5 km (red) and 15 km (green).

## 6.4 Three Layer Turbulence Profiles

This section will describe how the value of  $r_0$  can be corrected for scintillation by using a three layer model of the atmospheric profile. The turbulence profile is estimated by three layers at chosen fixed altitudes, such that three unknowns (the turbulence strength at these altitudes) are estimated from three measurable quant-

ities; the scintillation index, intensity correlation between neighbouring subapertures and the measured  $r_0$ . Here the chosen altitudes are 0, 5 and 15 km. The work presented in this chapter is to illustrate a proof of concept, further investigation is required to optimise the chosen altitudes.

As an initial investigation each altitude was chosen for specific reasons. It was important to acquire a model, that could be fitted to data, where each layer produces distinguishable responses i.e. to have an orthogonal response.

- **The Ground Layer (0 km):** As shown by figure 6.1 the ground layer turbulence does not cause any scintillation effects. However, it does contribute to the total integrated seeing. Therefore, of the three measurable quantities, only one is affected by the ground layer. This makes it an ideal fixed layer to choose. In addition, typical atmospheric profiles have a strong turbulent layer at the ground.
- **The Higher Layer (15 km):** As shown by figure 6.1 the higher altitude layers produce the most amount of scintillation as well as highly correlated intensities of neighbouring subapertures. This will affect the measured scintillation index and correlation substantially. It is therefore desirable to choose a high altitude for one of the layers in the model. For this reason, and the fact that typical atmospheric profiles have a strong turbulent layer at the jet stream, the highest fixed turbulent layer was set to 15 km.
- **The Middle Layer (5 km):** The intermediate layer must cause distinguishable effects from the two other turbulent layers. It is desirable that the middle turbulent layer would produce a high scintillation value but without a significant correlation between neighbouring subapertures. This would make it distinguishable from the high layer (15 km), since it produces strong scintillation and a high correlation, and from the ground layer which produces zero in both parameters. It is clear from figure 6.1(c) and (d), that in order to satisfy these conditions i.e. significant scintillation but low correlation, the altitude

of the middle layer should be between 4 to 8 km. For this investigation a layer at 5 km was chosen.

Figure 6.17 in section 6.5 illustrates how a single turbulent layer at varying altitudes is represented by the three layer fixed altitude model for the C9-SHIMM, for simulated data. It can be seen that greater than 50% of the turbulence strength is allocated to the intermediate altitude (5 km) bin, for input layer altitudes from 3 - 10 km, with a peak response of approx. 80% for input layers in the range 5 - 7 km.

This demonstrates that, by including the measured correlation of scintillation in the model fit, and assuming realistic statistical uncertainties in the measurements, the 3 layer model is able to successfully distinguish turbulence at mid-altitudes from that at the ground or at high altitudes.

The fraction of turbulence strength allocated to the 5 km layer peaks when the input layer is at 5 km. However, only 80% of the strength is placed in this altitude bin, with the remaining 20% allocated, incorrectly, to the 0 km and 15 km layers. Some further modelling is required to determine the optimum altitude for the mid-altitude layer in the model. i.e. it is possible that a higher peak response may be obtained if a slightly different model altitude is assumed.

Also, the response could be investigated as a function of the statistical uncertainty of the input data. It is possible that averaging the measurements over a longer time period will reduce the statistical uncertainty and likely to improve the peak response, i.e. will reduce the fraction of turbulence wrongly allocated to the other model layers.

Figure 6.6 displays simulated results for three turbulent layers at 0, 5 and 15 km, for a range of turbulence strengths. Figure 6.6(a) displays the percentage difference between the measured and input turbulence strengths when the strength at 0 km is fixed ( $50 \times 10^{-15} \text{ m}^{1/3}$ ). Figure 6.6(b) and (c) shows how the scintillation index and correlation change for different turbulent strengths at 5 and 15 km. Since

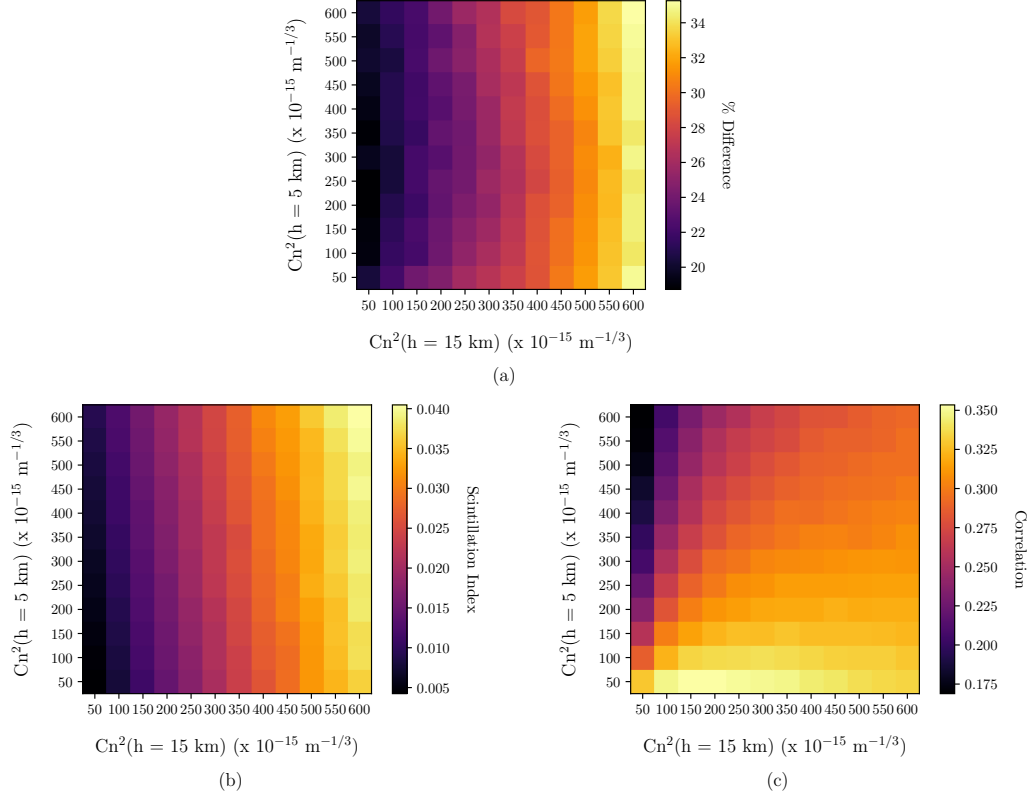


Figure 6.6: Simulated results for a turbulence profile with three turbulent layers with fixed altitudes 0, 5 and 15 km, for the C11-SHIMM configuration. The  $C_n^2$  at 0 km is  $50 \times 10^{-15} \text{ m}^{-1/3}$ . Axis values indicate the increasing input  $C_n^2$  values for the 5 and 15 km layers. The figures show how (a) the measured  $C_n^2$  (b) scintillation index and (c) the correlation changes with different  $C_n^2$  values.

these scintillation properties are unaffected by turbulent layers conjugate to the pupil plane i.e. at altitude 0 km, figures 6.6(b) and (c) will be the same for any turbulent strength at the pupil plane. These figures are a graphical representation of the reference look-up table for the C11-SHIMM WFS configuration that is used to determine the strength of the layers at 5 and 15 km.

The correction was implemented in the same way as described in the previous two sections. By cross referencing the measured scintillation parameters with the model

parameters, the turbulent strength at 5 and 15 km can be estimated.

### 6.4.1 Correction of $r_0$

The change in the measured turbulence strengths induced for propagation distances of 5 and 15 km can be estimated. The sum of  $\Delta Cn^2(h = 5)$  and  $\Delta Cn^2(h = 15)$  can then be subtracted from  $C_{nm}^2$ . Figure 6.7 shows simulated results of the measured  $r_0$  value before and after correcting for scintillation, for different turbulent profiles. Each plot shows results for three layer turbulent profiles, where the altitude profile is denoted on each plot. A range of turbulent strengths were used ( $C_n^2 = 100 \times 10^{-15} - 500 \times 10^{-15} \text{ m}^{1/3}$ ) for turbulent layers at altitudes of 5 and 15 km with a fixed turbulent strength of  $C_n^2 = 50 \times 10^{-15} \text{ m}^{1/3}$  at altitude 0 km.

By comparing the values for  $r_0$  before and after correcting for scintillation, it can be seen that the estimated value of  $r_0$  after correction is much closer to the input  $r_0$  value (illustrated by the  $x = y$  line). Whilst the correction is not always exact, it is at least an order of magnitude improvement in accuracy to the original estimation of  $r_0$ .

### 6.4.2 Profiling

The method described above for correcting the measured value of  $r_0$  for the effects of scintillation involves estimating the turbulence strength at 5 and 15 km. The turbulence strength at 0 km can be derived from this, by differencing the corrected total integrated strength and the strength acquired from the altitudes at 5 and 15 km. It is therefore possible to estimate a crude three layer turbulence profile. This provides an additional functionality of the SHIMM instrument that is not provided by the current DIMM instrument.

In practice, applying this method directly to acquire a three layer profile can fail, producing a negative strength at the ground. This typically occurs either when the

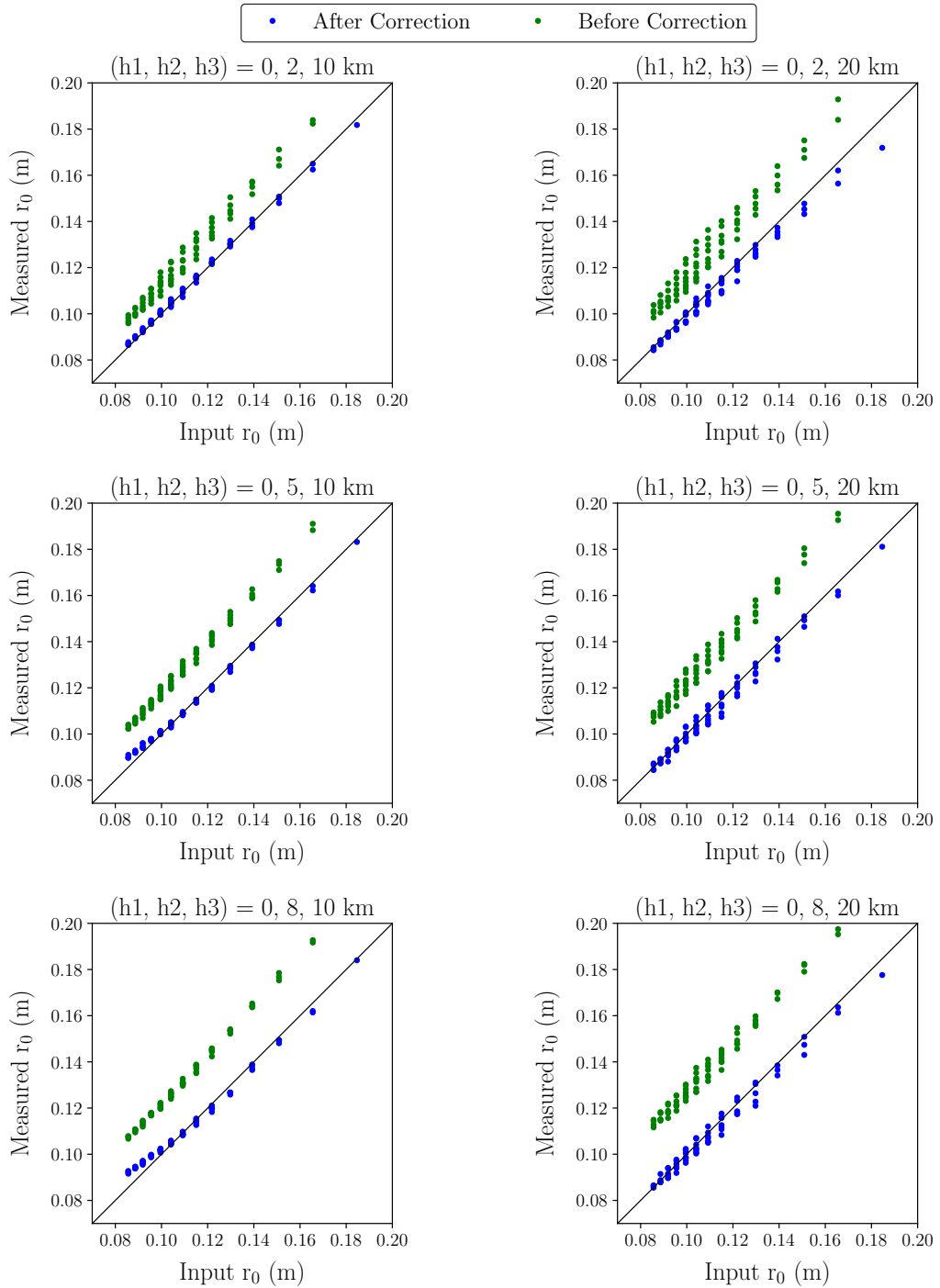


Figure 6.7: Simulated results displaying the measured uncorrected (green) and corrected (blue) values of  $r_0$  versus the known input  $r_0$ , for the C11-SHIMM configuration. Each figure displays results for two turbulent layers at varying heights and a fixed ground layer.

total turbulence strength has been underestimated or when the turbulence strength at high altitudes has been overestimated.

This problem can be solved by incorporating the measured  $r_0$  value into the fit. This is done by using the corrected turbulence strength value to limit the total turbulence of three turbulent layers. With this method three measured parameters,  $r_0$ ,  $\sigma_I^2$  and  $Corr$ , are used to estimate three unknowns i.e. the turbulence strength of each turbulent layer at 0, 5 and 15 km. A least square fit can be applied to acquire a three layer profile at these altitudes. Example simulations using this fitting process are illustrated in figures 6.8 and 6.9. Figure 6.8 shows examples where the input and corrected total turbulence strength are equal. The input profiles have turbulent layers at a range of altitudes and, as a result, the turbulence is shared between the fitted layers. For example, in the case of the profile with turbulent layers at 2 and 10 km (top left image), the turbulence strength at 2 km has been shared between the turbulent layer at 0 and 5 km in the fit. Whilst these input and output profiles differ in detail, the values of  $\theta_0$  associated with them agree within statistical uncertainty. This indicates that this method can be used to provide a useful estimate of the turbulence profile as a three fixed layer model.

Figure 6.9 shows examples where the corrected total turbulent strength sometimes underestimates the total turbulent strength. In general, it appears the underestimation is by approximately  $50 \times 10^{-15} \text{ m}^{1/3}$ . Whilst this measurement of the total turbulent strength is incorrect, it can still, in some cases, estimate the values of  $\theta_0$ , within the estimated uncertainty.

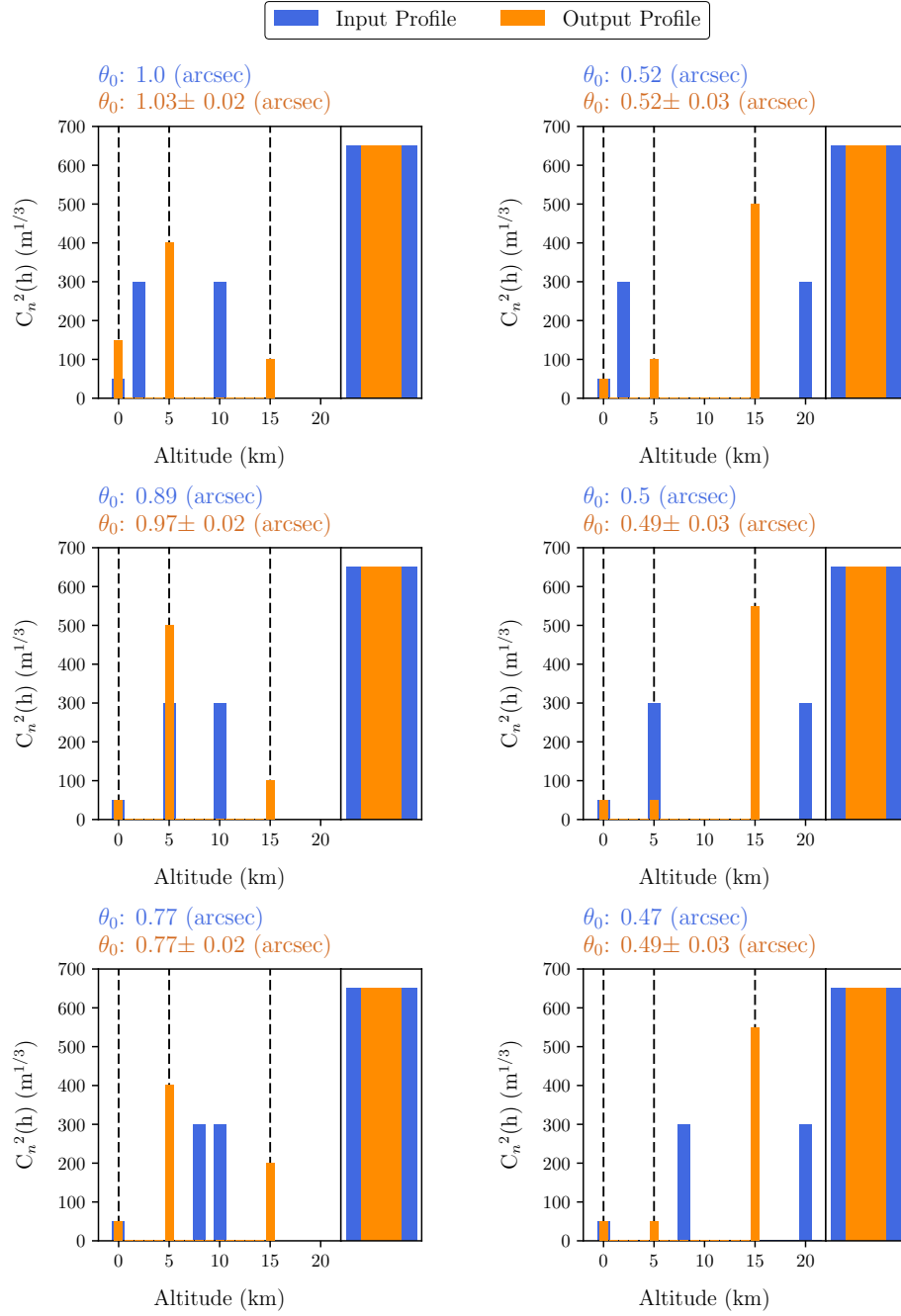


Figure 6.8: Example of simulated results displaying the input (blue) and output profiles (orange) fit to a three layer turbulence profile at altitudes 0, 5 and 15 km (denoted by the black dashed lines), for the C11-SHIMM configuration. The single broad bar on the right hand side of each figure displays the total turbulence strength. The values of  $\theta_0$ , calculated from the two profiles, are noted on the left above each figure.

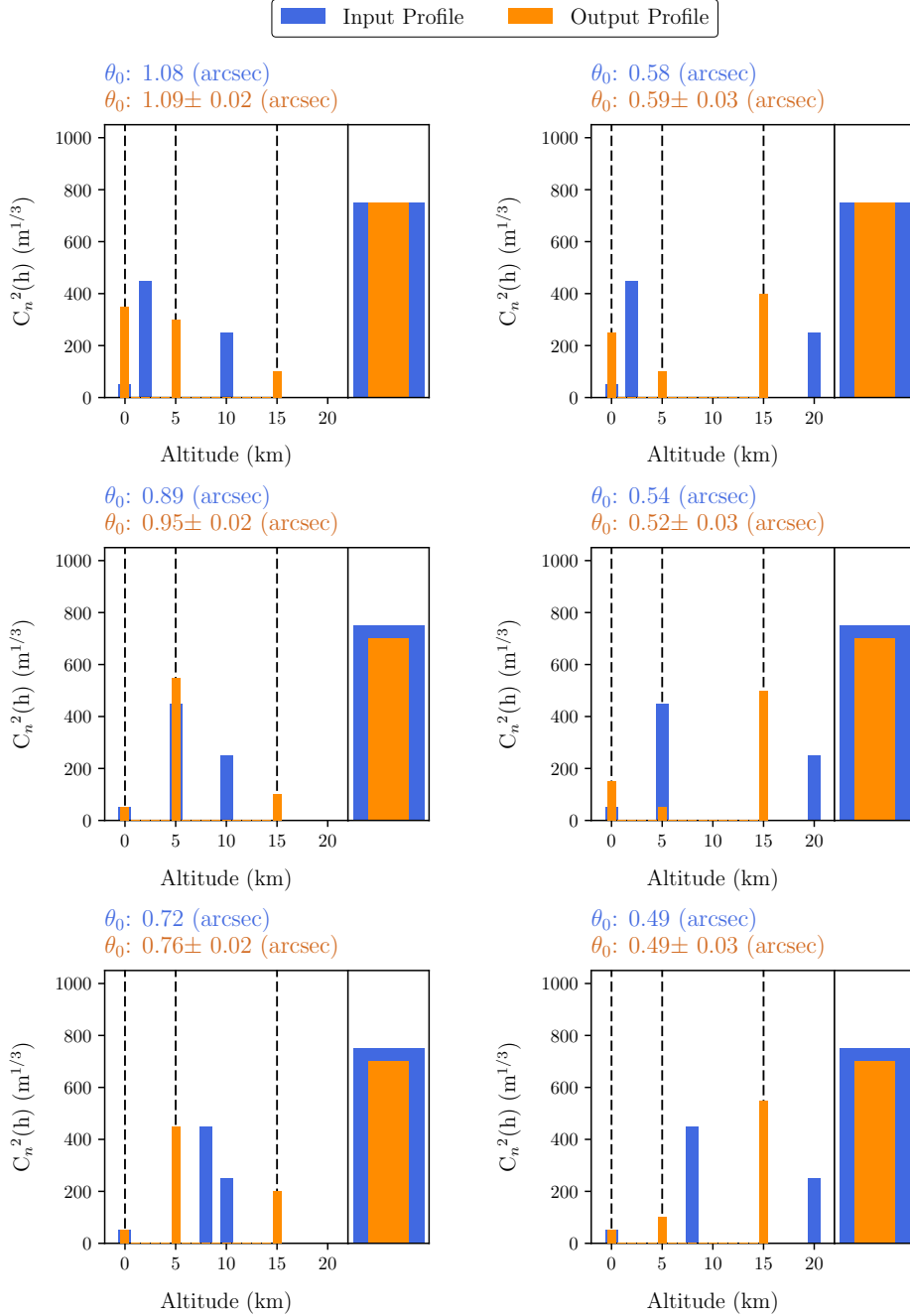


Figure 6.9: Examples of simulated results, for the C11-SHIMM configuration, when the total turbulence strength of the input (blue) and output fitted (orange) profiles are not equal. The measured parameters of  $r_0$ , scintillation index and correlation is fitted to the input profile to form a three layer turbulence profile at altitudes 0, 5 and 15 km (denoted by the black dashed lines). The single broad bar on the right hand side of each figure displays the total turbulence strength. The values of  $\theta_0$ , calculated from the two profiles, are noted on the left above each figure.

## 6.5 On-Sky Results

In this section on-sky results from observations obtained in July 2015 and September 2015 by the C11-SHIMM, will be presented. In addition, comparisons between Stereo-SCIDAR and the C9-SHIMM, obtained in June 2015 and October 2015, will also be presented. For details of the observations see table 4.2 in section 4.5. The first two stages of data reduction, i.e. data quality control and centroiding, are described in chapter 4 section 4.3. Obtaining scintillation information requires the same quality control.

### 6.5.1 Results

#### Correcting Scintillation Effects on $r_0$

Figure 6.10 displays corrected values of  $r_0$  versus the initial measurement of  $r_0$ . The median correction is of  $\sim 8\%$ . Correction to  $r_0$  occurs when high altitude turbulent layers are present. A large correction implies that of the total integrated turbulence strength a large proportion of the turbulence is in the high altitude layers. Large corrections of up to 30% occurred only for cases where the initial measurement of  $r_0 > 0.15$  m. This implies that at times of small  $r_0$  i.e. bad seeing, the profiles would have been ground layer dominated.

The error bars in the measured  $r_0$  are given by the propagation of error from the uncertainty in the fit of the theoretical model to the on-sky data. The  $r_0$  correction process requires estimates of the turbulence strengths for the fixed layers at 5 and 15 km. These are found from the scintillation information. The sources of error in  $\sigma_I^2$  and  $Corr$  will be from statistical uncertainty and shot noise. Each measurement of the scintillation index and correlation of neighbouring subapertures were averaged over a number of datasets within a 1 – 5 minute period. The uncertainty in this scintillation information was established from the standard error of samples used. This averaging reduces the statistical uncertainty.

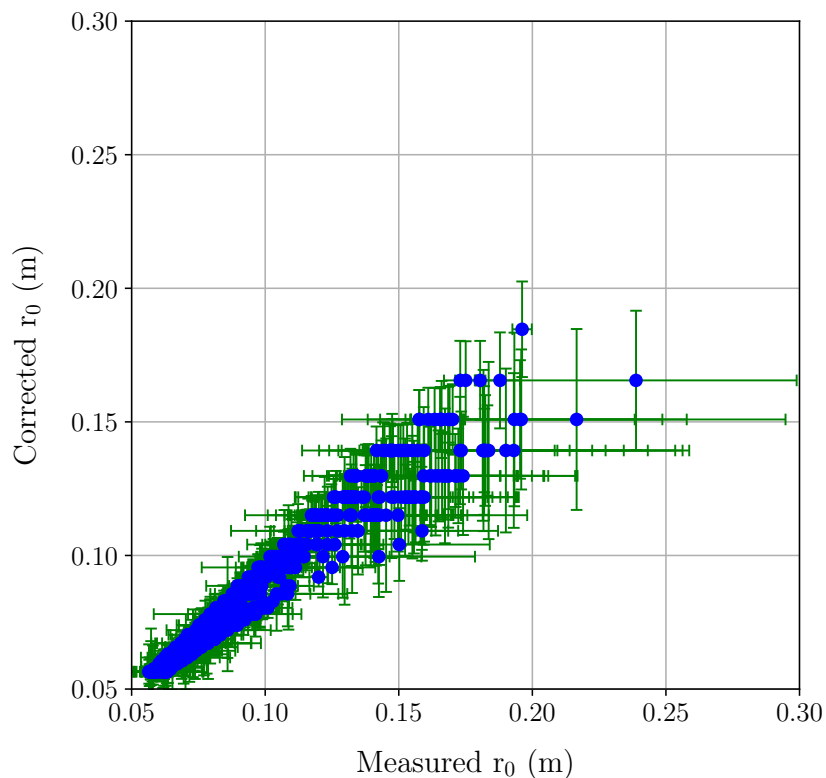


Figure 6.10: Scintillation correction of on-sky  $r_0$  estimates taken with the C11-SHIMM in La Palma, taken over 15 nights. The figure displays the corrected values of  $r_0$  against the measured values of  $r_0$ .

Shot noise can be reduced by observing only bright target stars. To reduce the uncertainty on the measurement of  $\sigma_I^2$ , the shot noise must be much less than scintillation noise, i.e.  $\sigma_I \gg 1/\sqrt{N}$ , where  $N$  is the number of photons. For example, if the value of  $\sigma_I$  for a single subaperture is  $\approx 0.26$ ,  $N$  must be  $\gg 15$  photons. The number of photons on a CCD is described as

$$\textit{photons} = \textit{bandwidth} \times \textit{throughput} \times \textit{rate} \times t_{\textit{exp}} \times A, \quad (6.7)$$

where *bandwidth* is the wavelength range that is observed, *throughput* is the fraction of the incoming photon flux above the atmosphere that is detected by the instrument, *rate* is the number of photons from above the atmosphere,  $t_{\textit{exp}}$  is

the exposure time and  $A$  is the area of the subaperture. If the following is assumed:  $bandwidth = 3700 \text{ \AA}$ , which corresponds to the visible spectrum bandwidth;  $throughput = 0.45$ , which corresponds to the quantum efficiency at the midpoint wavelength of the visible spectrum;  $t_{exp} = 2 \text{ ms}$ ; and  $A = (4.7 \text{ cm})^2$ ; then in order to obtain a shot noise ten times less than scintillation noise a magnitude star of  $\sim 6$  is required. In practise only targets greater than second magnitude were used. It should be noted that, the throughput will also be effected by the transmission of light through the atmosphere, the telescope mirror(s) and the SHIMM optics. For a more realistic number this needs to be tested in the lab.

In correcting the scintillation effects on  $r_0$ , the accuracy in  $r_0$  is improved, however the precision decreases due to the uncertainty accumulated from using additional measured parameters.

### **Turbulence Profiling**

Figure 6.11 displays examples of turbulence profile sequences, estimated from C11-SHIMM data, for four different nights in September 2016. These profiles have not been corrected for airmass. Intervals in the profile sequences were due to target changes, telescope autoguiding corrections and occasional overcast. The values of  $\theta_0$  over each night are also displayed in figure 6.11, illustrating how the parameter changes with different profiles. As expected the value of  $\theta_0$  increases as the turbulence strength at the ground becomes proportionally stronger compared to the other turbulent layers.

Figure 6.12 illustrates an example of on-sky data for a single night, demonstrating how the scintillation fitting parameters (the scintillation index and the correlation between the intensities of neighbouring subapertures) evolve, as well as the percentage difference in the change of  $r_0$  before and after scintillation correction. As expected the scintillation index increases as the turbulent layers at higher altitudes increase. The turbulence profile also coincides with the evolution of the correlation

of intensities of neighbouring subapertures. For example the minimum correlation value occurred when the 5 km turbulent layer is the strongest turbulent layer. This agrees with the correlation model illustrated in figure 6.6. The greatest correction in the value of  $r_0$  occurred when a larger proportion of the total turbulence strength is in the higher altitudes. For example, whilst the turbulence at altitude 15 km is the strongest at time = 6 hours, the largest correction occurred at time = 4 hours. This is because at time = 4 hours the ground layer is much weaker compared to the higher altitude layers.

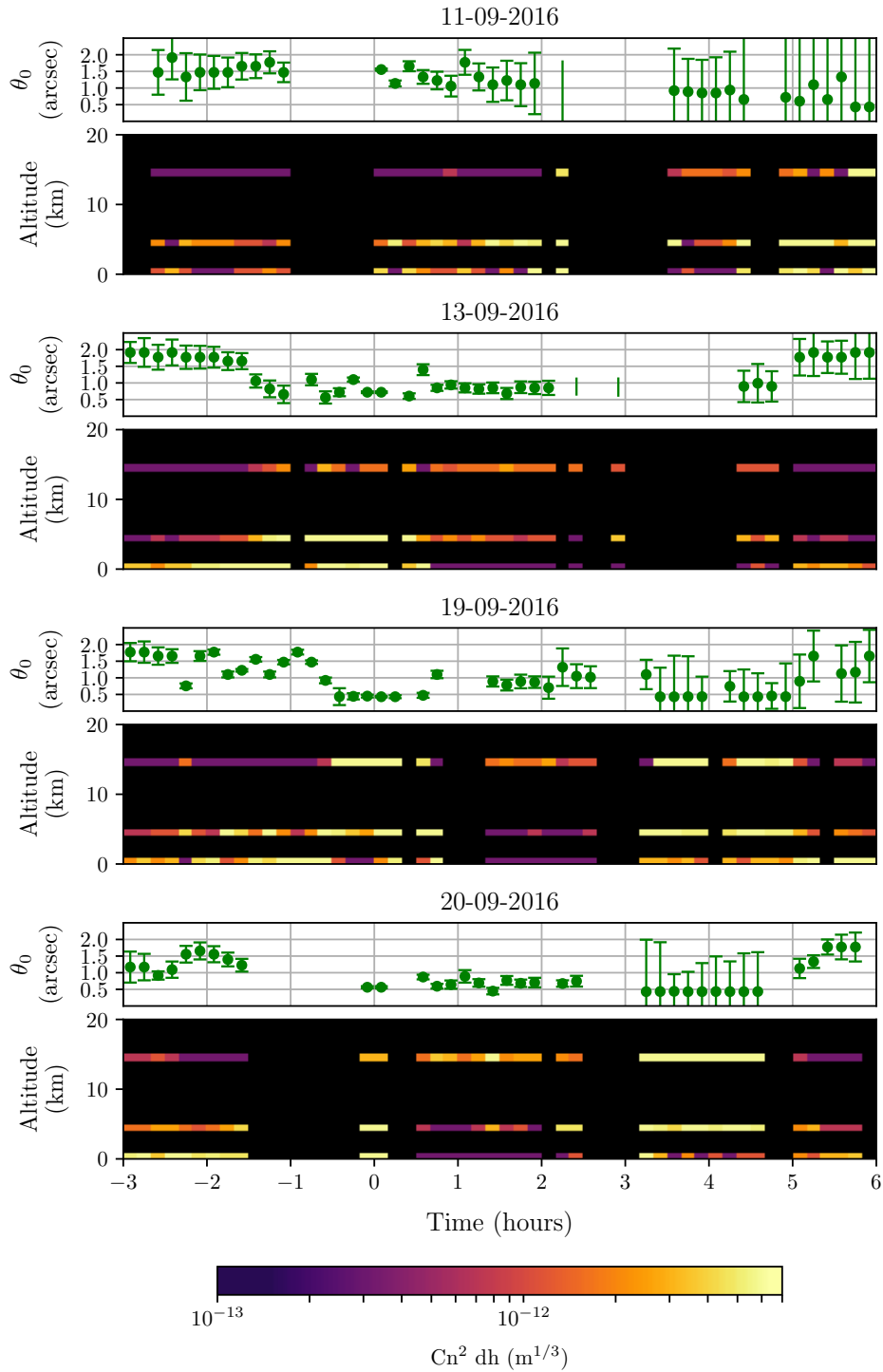


Figure 6.11: Examples of on-sky turbulence profile sequences recorded with the C11-SHIMM over a range of nights. The value of  $\theta_0$  as a function of time (green markers) are displayed above each profile. Intervals in the profile sequences are from when the C11-SHIMM was not observing.

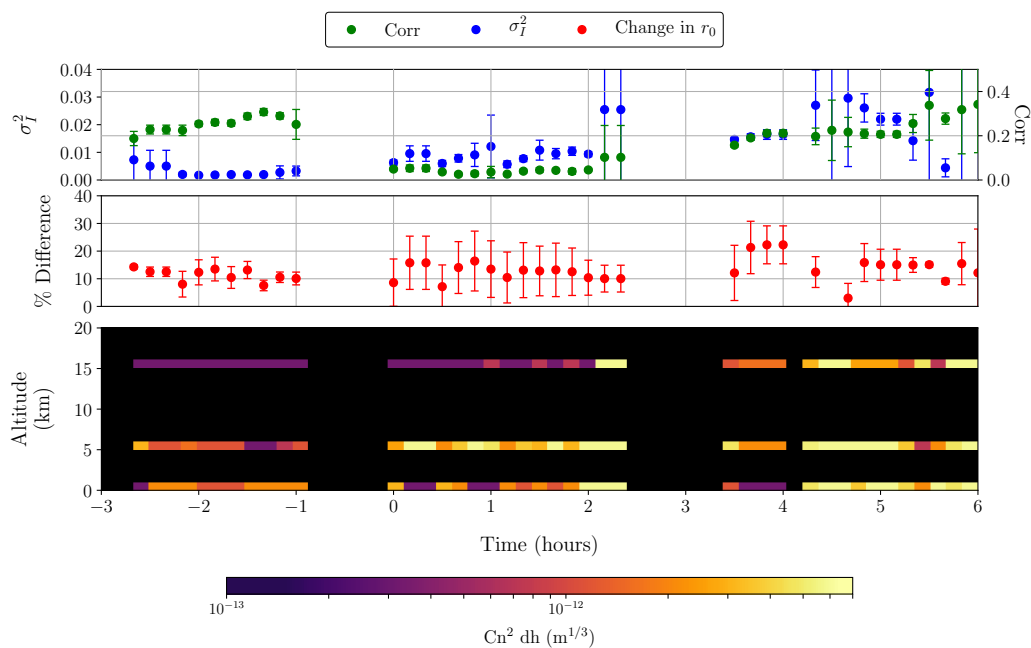


Figure 6.12: An example on-sky turbulence profile recorded with the C11-SHIMM at the ING site in La Palma. The scintillation index (blue), the correlation between intensities of neighbouring subapertures (green) and the percentage difference in the change of the measured  $r_0$  value before and after correction (red) are also displayed.

This method was further applied on the C9-SHIMM data obtained at La Palma in June and October 2015. This required a reference look-up table specific for the WFS configuration of the C9-SHIMM. These results were compared to contemporaneous results obtained by the Stereo-SCIDAR, mounted on the INT. In order to compare the two instruments the SHIMM needed to be corrected for airmass. This correction was applied to both the altitude and the turbulence strength of the layers. The correction in the altitude is due to the propagation distance, which will alter the amount of scintillation observed by the instrument. The altitude is therefore corrected by  $h = z \cos(Z)$ , where  $z$  is the propagation distance and  $Z$  is the zenith angle. Once airmass corrected the altitude of the estimated turbulence profile will not be fixed at 5 and 15 km. The airmass correction on the turbulence

strength is derived from equation 2.8 where the integrated  $C_n^2(h)$  is proportional to  $\cos(Z)$ .

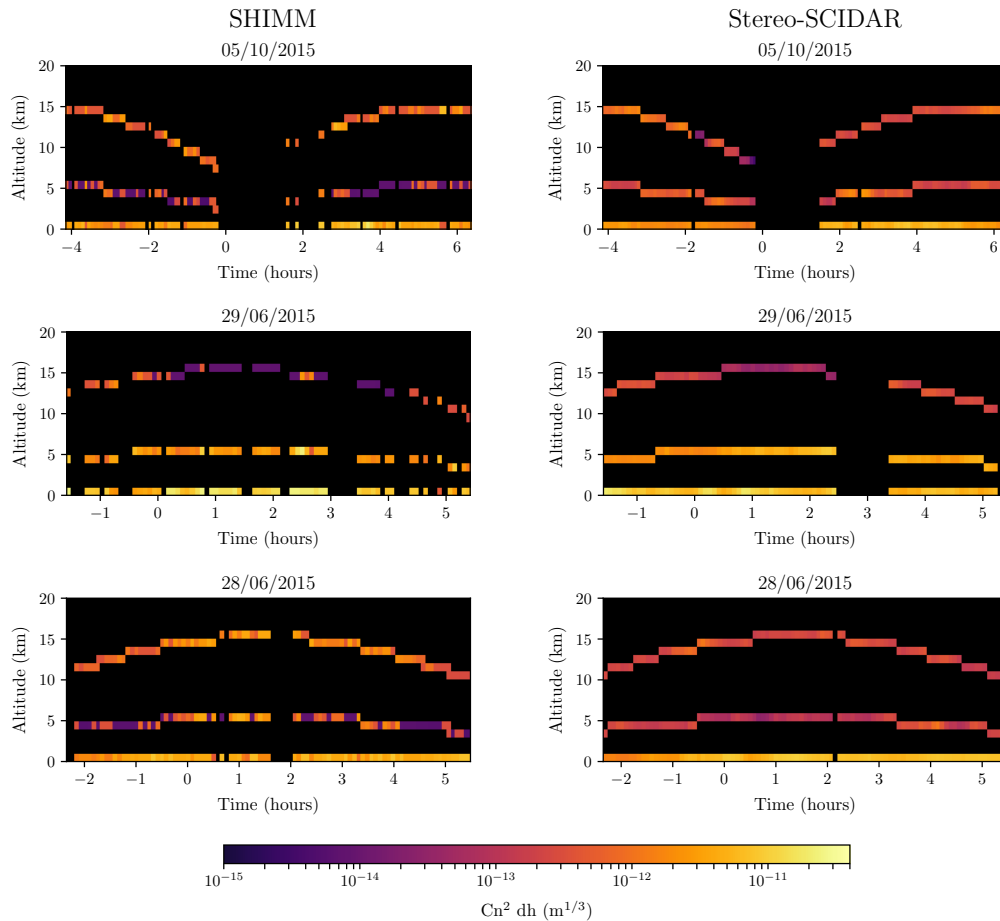


Figure 6.13: Examples of on-sky turbulence profiles recorded with the C9-SHIMM and Stereo-SCIDAR over a range of nights in 2015. Stereo-SCIDAR data, see figure 6.14, has been binned to match the three altitude profile of the SHIMM. The programme used to bin the Stereo-SCIDAR data was provided courtesy of Douglas J. Laidlaw.

Figure 6.13 displays three nights of data obtained at La Palma by the C9-SHIMM and Stereo-SCIDAR mounted on the INT. The Stereo-SCIDAR data, see figure 6.14, has been binned to match the vertical profile resolution of the SHIMM. The programme used to bin the Stereo-SCIDAR data was provided courtesy of Douglas J.

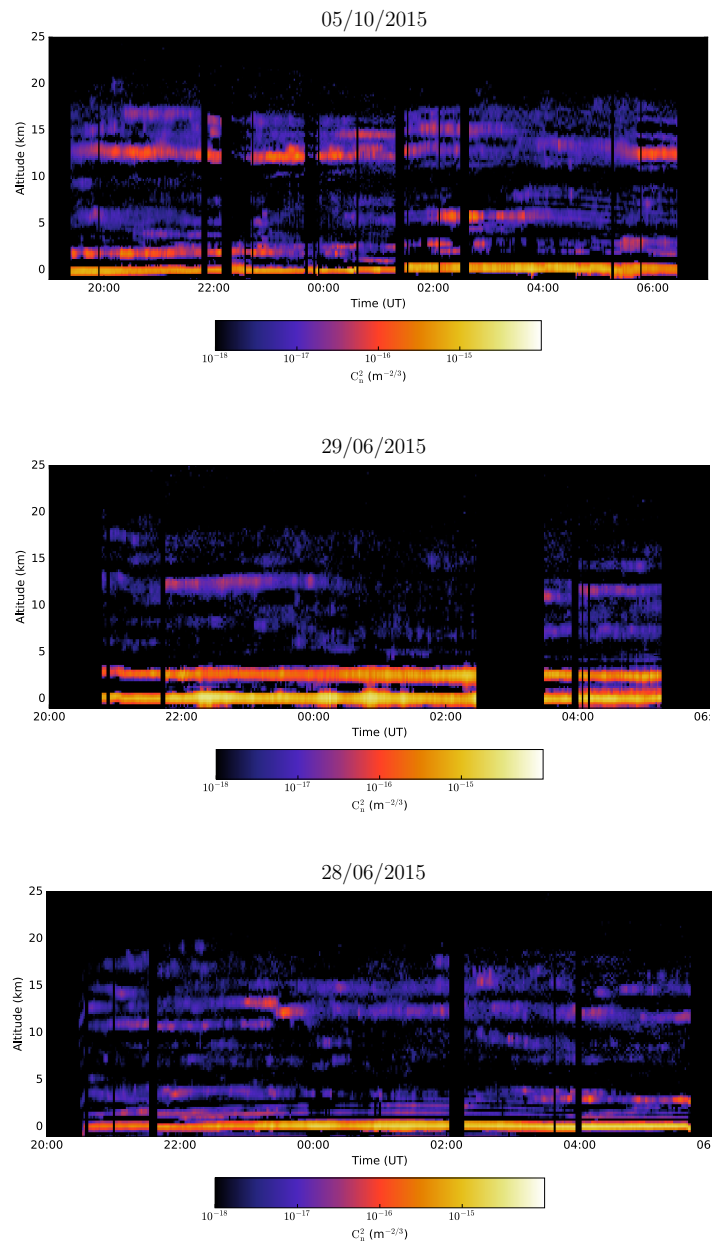


Figure 6.14: Examples of on-sky turbulence profiles recorded with Stereo-SCIDAR in La Palma.

Laidlaw. Anecdotally, the profiles show very similar features. Figure 6.14 shows the high resolution profiles recorded by Stereo-SCIDAR for the corresponding nights shown in figure 6.13 (Shepherd et al., 2013). It can be seen that on the 28th and

29th June 2015 there was little activity at high altitudes compared to that observed at the lower altitudes. However, on the 5th October 2015 strong turbulence was recorded at approximately 12 km for most of the night. Most of the nights when both the SHIMM and Stereo-SCIDAR were in operation, Stereo-SCIDAR recorded profiles similar to that of the 28/29th June profiles, i.e. relatively weak high altitude turbulence.

Figure 6.15 shows a comparison between the measured values of  $\theta_0$  from the Stereo-SCIDAR and SHIMM instruments. Whilst the results illustrate a lot of scatter between the measurements of the two instruments, there does not appear to be a systematic bias to over- or underestimate  $\theta_0$ . SHIMM values with uncertainties greater than 20% were not plotted in this comparison.

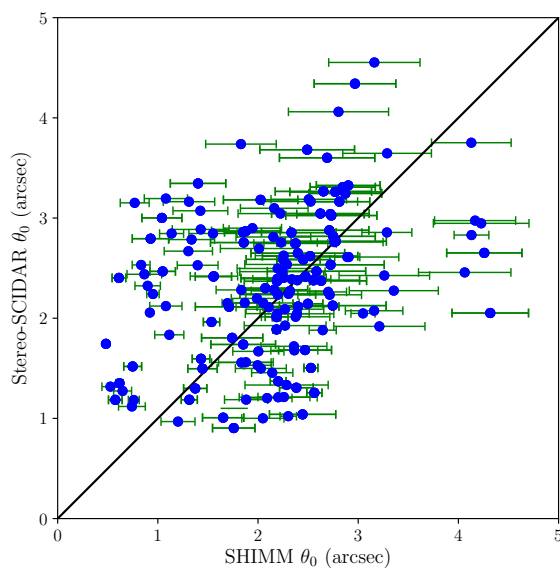


Figure 6.15: On-sky comparisons of  $\theta_0$  estimates from the Stereo-SCIDAR, mounted on the INT, and the C9-SHIMM in La Palma.

Figure 6.16(a)-(c) shows comparisons of the turbulence strength at 0, 5 and 15 km (after airmass correction) between the two instruments, respectively. It appears that there is agreement between the turbulence strength at the ground. Figure 6.16(b) indicates there is also an agreement at the 5 km altitude bin. However, the data shows there is more scatter, in particular for turbulent strengths less than  $100 \times 10^{-15} m^{1/3}$ . For strong turbulence the comparison suggests that the SHIMM underestimates the turbulence strength. Figure 6.16(c) shows there is a lot of scatter in the comparison of the two instruments for the 15 km altitude bin, with a tendency for the SHIMM to overestimate the turbulence strength. However, a good agreement of the total seeing estimated by the two instruments is shown in figure 6.16(d), particularly for seeing values less than 1.5 arcsec. It is possible that the reason for the discrepancies between the turbulence strength estimations at 5 and 15 km is due to the placement of turbulent layers that lie between the two altitudes. Figure 6.17 illustrates how the three layer C9-SHIMM model places a simulated single turbulent layer at different altitudes. The method for binning the Stereo-SCIDAR's high resolution turbulence profile is by linear integration of its measured turbulent layers. In order to create a profile analogous with the SHIMM's three layer profile, this binning method defines bin boundaries of Stereo-SCIDAR data. For example, for the 5 km bin, the boundaries are 2.5 and 10 km. Therefore, a turbulent layer at 8 km will be totally allocated to the 5 km bin. Whereas, as shown by figure 6.17, the SHIMM analysis will allocate approximately 70% and 20% of the turbulence to the 5 and 15 km bin respectively.

The error bars on the SHIMM results, in figures 6.15 and 6.16, were calculated from the error propagation of the residuals of the least square fit between the theoretical model and the measured parameters.

Anecdotally, it appears that this method can produce a useful estimate for the turbulence profile. However, more data is required to see: if the differences between the profiles obtained by the two instruments is systematic or random; what the effects of considering polychromatic light will have on the results; if the difference

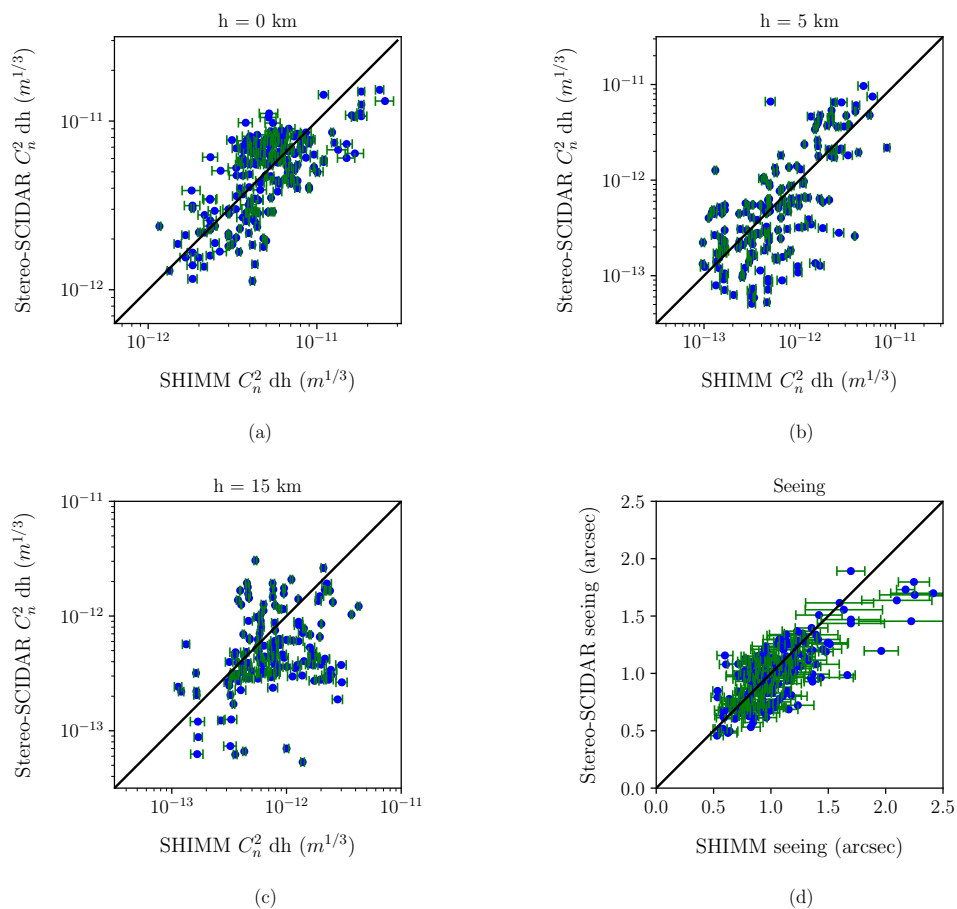


Figure 6.16: On-sky comparison results, between the Stereo-SCIDAR mounted on the INT and the C9-SHIMM, for the turbulence strength at 0 km (a), 5 km (b) and 15 km (c) when airmass corrected, and the total integrated seeing (d).

in the direction of the observed target stars has an impact on the measurement of the profile; and whether for a large data sets the correlation between the results will converge. As described above, the on-sky data used for these comparisons were taken on nights when the turbulence profile observed by Stereo-SCIDAR looked similar to that on the 28/29th June 2015, shown in figure 6.14. These nights typically observed weak turbulence at high altitudes. More concurrent data with a range of activity is required to find the limitations of the SHIMM profiling method, and to identify when erroneous results are measured.

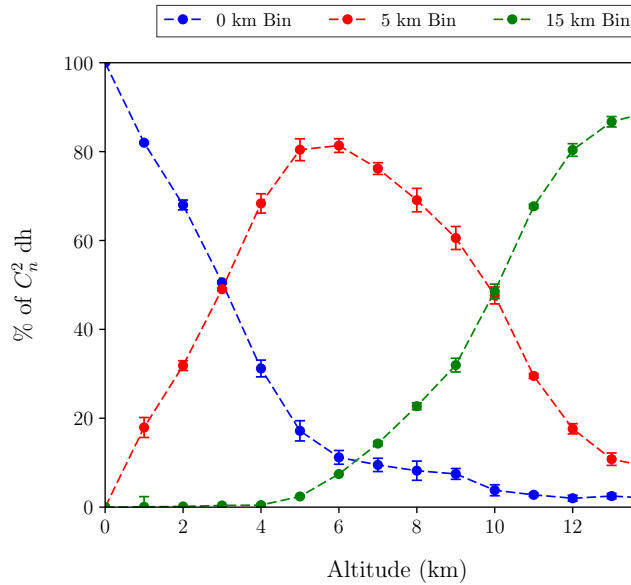


Figure 6.17: Illustration of how a single simulated turbulent layer is binned into the 0 km (blue), 5 km (red), and 15 km (green) bins as defined by the SHIMM’s three turbulence layer model. As a single layer is placed at different altitudes the total turbulence strength of that layer is distributed amongst the three defined altitude bins.

## 6.5.2 Limitations & Noise

The three key contributing noise and uncertainty factors in utilising the described method for correcting scintillation effects on  $r_0$  and producing a fixed three layer turbulence profile are: the uncertainty in the fit to measure  $r_0$ , this can be due to statistical noise, non-Kolmogorov turbulence or scintillation; the statistical uncertainty of each measurement of  $r_0$  and the scintillation information; and the contributing noise factors in measuring the total number of photon counts for each subaperture.

The uncertainty associated with the measurement of  $r_0$  has been discussed in chapter 4. Statistical noise can be reduced by averaging more datasets. Typically data is averaged for between 1 – 5 minutes. Data averaged over too long a

period however will not produce accurate results since the atmospheric turbulence profile is likely to evolve significantly over this period. Noise in measuring photon counts will be shot noise, sky background and readout noise. Since short exposures are used for observing bright target stars, sky background and readout noise is negligible. In order to reduce shot noise target stars were limited to second magnitude or brighter. The uncertainty in the correlation in intensities of neighbouring subapertures will not be effected by shot noise, since it is uncorrelated.

More concurrent data from the SHIMM and Stereo-SCIDAR is required to determine if there is a limitation in measuring turbulence profiles accurately under a range of atmospheric conditions.

## 6.6 Conclusions and Futher Work

In this chapter the necessity for correcting scintillation effects on  $r_0$  was discussed. It was found that the scintillation index and correlation of intensities between neighbouring subapertures can be used to correct the scintillation effects on  $r_0$ , by employing a reference look-up table. It was shown that this method results in an order of magnitude improvement in accuracy of the estimated value of  $r_0$  and is often equal to the input value of  $r_0$  within uncertainty. Using the three measured parameters,  $r_0$ , the scintillation index and the correlation in the intensity of neighbouring subapertures, it is possible to obtain a three layer turbulence profile. The accuracy of this method was illustrated by simulating different turbulence profiles and correctly estimating the value of  $\theta_0$ .

The method for correcting  $r_0$  and estimating a three layer profile was applied to on-sky data and results were presented. Concurrent observations with a high resolution profiling instrument Stereo-SCIDAR was presented. These results showed some agreement between the two instruments, however more contemporaneous measurements are required to confirm this method and understand it's limitations. An extended observing campaign for the FASS-SHIMM is scheduled for 2017/2018

at Paranal. This would provide an opportunity to compare results with both a Stereo-SCIDAR instrument and the FASS.

The model was based on using a fixed layer turbulent model. The three chosen altitudes presented in this chapter (0, 5 and 15 km) were used as a proof of concept for this method. Further investigation is required into the optimisation of middle and higher fixed altitudes.

The model used for estimating the turbulence profiles assumes monochromatic light. In reality this is not the case, and the spectrum of the target and spectral response of the CCD will effect the measurement of the profiles. This effect is further discussed in the next section. Integrating the effects of polychromatic light into the model will be an important next step in developing the estimation of the turbulence profile with the SHIMM instrument.

## **6.7 FASS-SHIMM**

The FASS is a novel turbulence profiling technique that exploits a low noise EMCCD to image the full aperture of the telescope in order to measure the atmospheric turbulence profile. This technique could replace the current MASS instrument since it is not only easier to implement, but it also aims to produce higher resolution turbulence profiles. The FASS instrument is a collaborative development between PUC, Chile and Durham University, UK. The concept and analysis was developed by Andrés Guesalaga at PUC, and the design, manufacturing and testing was completed at Durham University.

The FASS was combined with the SHIMM, to make the FASS-SHIMM. The FASS when conjugated to the ground can not detect the ground layer turbulence. Since the SHIMM measures the total integrated turbulence, the strength of the ground layer can be found by differencing these measurements from the two instruments. The FASS and SHIMM are an ideal combination since both instruments require the

full unmasked aperture of the telescope. This is in contrast to the MASS-DIMM, where aperture masks for both instruments are used.

### 6.7.1 Concept

As described in section 2.2.2, as the altitude of a turbulent layer increases the structure of the scintillation pattern in the pupil image (‘flying shadows’ or ‘speckles’) changes i.e. the characteristic size of the Fresnel zones associated with the layer increase. The MASS instrument employs a four ring aperture system to act as a spatial filter. The same analysis could be achieved via software analysis of a well sampled pupil image, i.e. defining the ring apertures in software. However, an alternative approach is to extract the speckle size and intensity information from 2-D spatial power spectra obtained from the pupil image (Guesalaga et al., 2016). Figures 6.18(a) and (b) show examples of pupil images obtained with the 9.25 inch FASS-SHIMM telescope, exhibiting small scale structures associated with low altitude turbulence and larger scale structures associated with higher altitude turbulence, respectively. It can be seen in figure 6.18(b) that the size of the structures can be as large as the radius of the pupil images for this telescope. As a result, to measure the size of the speckles, concentric rings are defined, as depicted by the green lines in figure 6.19, and unravelled to obtain linear vectors. This increases the effective length of which the structures are sampled.

By calculating the power spectra of each linear vector, and averaging for a large number of images, spectra are obtained which are used for the profile estimation. Smaller speckles will populate higher spatial frequencies whereas large speckles will tend to concentrate energy at low spatial frequencies. Weighting functions, similar to those for the MASS (see section 3.3), can be calculated assuming Kolmogorov turbulence. These can then be used to estimate the optical turbulence profile via a fit to the measured data.

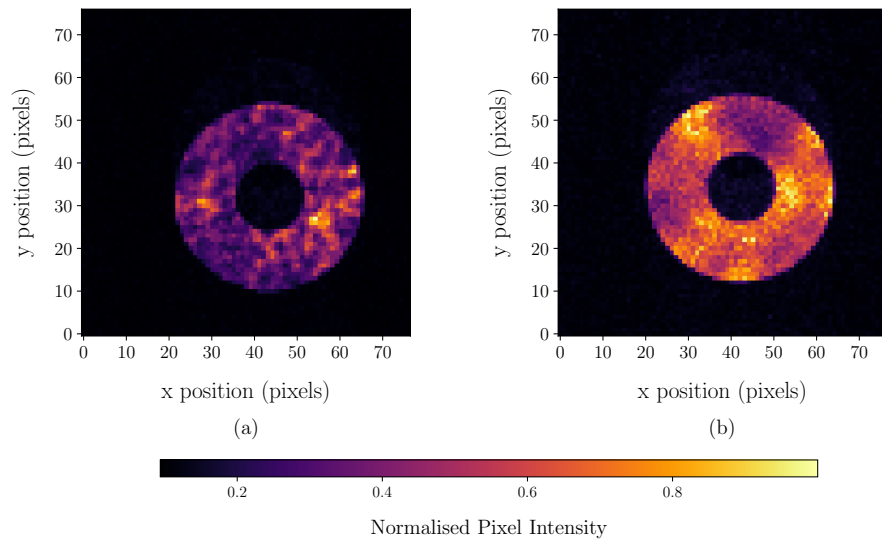


Figure 6.18: Examples of on-sky pupil images, from the 9.25 inch telescope, showing different speckle patterns, one dominated by low altitude turbulence (a) and one by higher altitude turbulence (b).

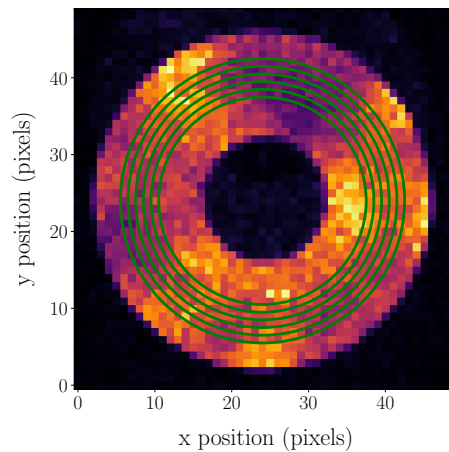


Figure 6.19: The green lines indicate example concentric rings that are unraveled via interpolation from a 2-D Cartesian annulus to obtain linear vectors.

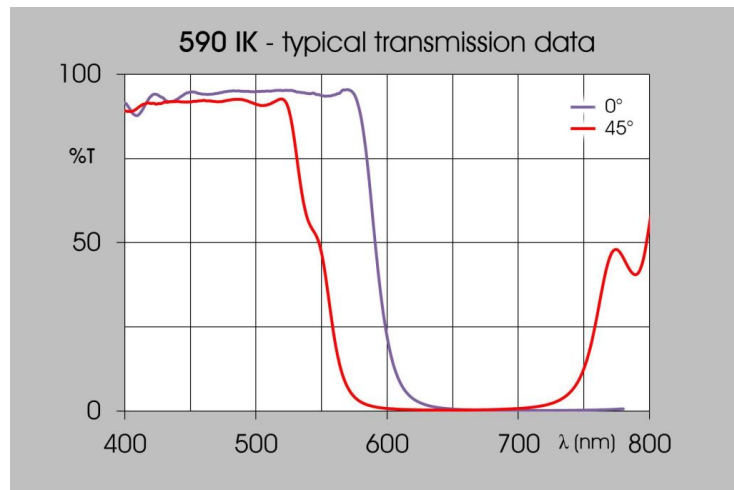


Figure 6.20: Showing dichroic spectral response (Comar part 509IK125) employed by the FASS-SHIMM and used at 45°.

## 6.7.2 Hardware & Software

In order to permit simultaneous observations with the FASS and SHIMM, a dichroic beamsplitter was used to pass red and blue light to the FASS and SHIMM optics respectively. This configuration was chosen since scintillation effects are more prominent at shorter wavelengths, which could cause saturation on the EMCCD. Figure 6.20 shows the spectral response of the dichroic when used at 45°, producing a 50% transmission at 550 nm.

Figure 6.21 displays the FASS-SHIMM optics that can be used for both C9- and C11-SHIMM configurations. Figure 6.22 illustrates a schematic of the optical configuration of the FASS-SHIMM. Light from the telescope passes through an achromatic lens to produce a parallel beam to the dichroic beamsplitter. Collimated red and blue light pass through re-imaging lenses to produce separate images with the same focal ratio for both the SHIMM and FASS optics. The SHIMM optics are as described in chapter 4. The FASS optics are comprised of a single collimating achromatic lens which images the telescope pupil onto the EMCCD.

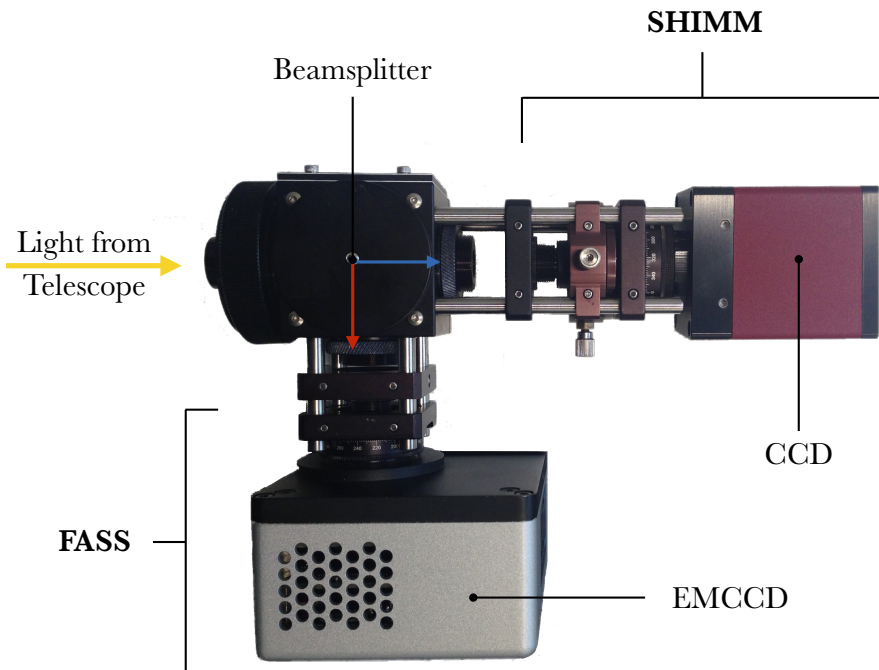


Figure 6.21: Image of the FASS-SHIMM optics. Light from the telescope enters the optics where the red and blue light passes to the FASS and SHIMM optics respectively.

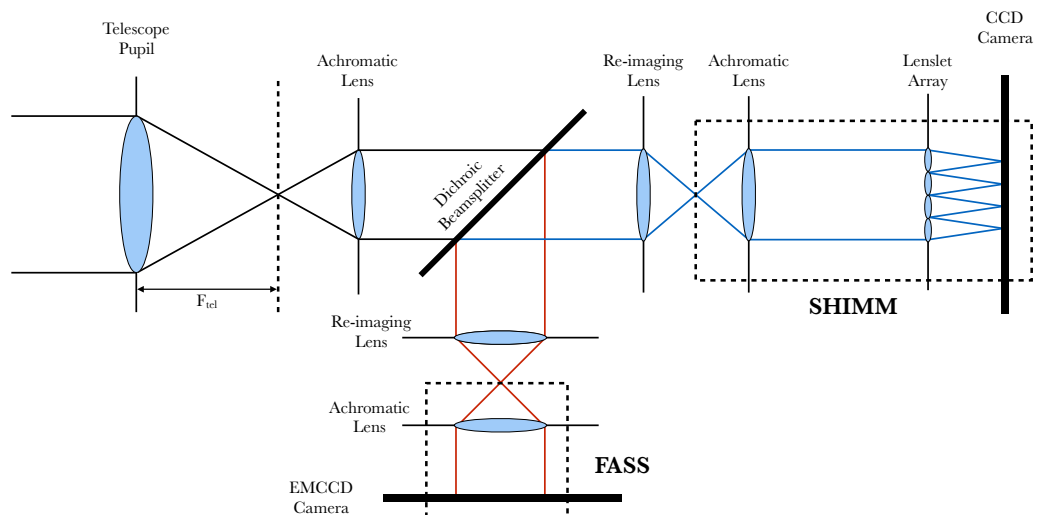


Figure 6.22: Schematic of the optical configuration of the FASS-SHIMM. Light from the telescope is collimated before passing red and blue light to the FASS and SHIMM branches respectively, via a dichroic beamsplitter. Re-imaging lenses are used to produce the same image as that located at the telescope focus.

In this implementation separate PCs were used for the FASS and the SHIMM components of the instrument. The EMCCD used for FASS was the Andor Luca S model. The specifications of the FASS are listed in table 6.1. When the FASS is combined with the SHIMM additional custom mounting components are required.

Features	Specifications
<b>Telescope</b>	
Model:	Celestron CGEM 9.25 inch f/10 Schmidt Cas-sagrain & Celestron CGEM 11 inch f/10 Schmidt Cassagrain
Mount:	VX Mount
<b>Optics</b>	
Lens:	Edmund Optics achromat lens with focal length of 30 mm.
Mount:	Thor labs lens mount and rotation stage.
<b>Detector</b>	
Model:	658 x 496 Andor Luca-S EMCCD
Pixel Size:	10 $\mu\text{m}$
Binning:	4 x 4
ROI:	72 x 72 pixels
Frame Rate:	153 Hz
Exposure Time:	1 ms
<b>PC:</b>	
Hardware:	ITX mini PC
OS:	Ubuntu 12.0

Table 6.1: FASS Specifications.

### EMCCD Considerations

**Binning & Region of interest:** The CCD image was binned in order to increase the SNR value. For a 9.25 inch telescope, 4 by 4 binning results in a pupil image with sampling of 5 mm/pixel. The pixel size is an important parameter since it limits the minimum altitude that the speckles can be reliably detected. The Fresnel radius for a turbulent layer at altitude 200 m and wavelength 500 nm is 10 mm. Therefore, for a turbulent layer at an altitude below 200 m the speckles will not be resolved by the detector. The analysis is unable to distinguish intensity fluctuations due to these low layers from shot noise of the detector. However, since turbulence at 200 m only produces very weak scintillation their contributions are typically negligible. Much of the imaging area of the EMCCD was unused. Under 4 by 4 binning the size of the EMCCD was 164 x 124 pixels, and the pupil image had a diameter of  $\sim 46$  pixels. Therefore, a region of interest was defined to minimize the data size in disc storage.

**Frame Rate & Sample Duration:** For 4 by 4 binning and this region of interest, the camera achieved a maximum frame rate of 153 Hz at an exposure time of 1 ms. A fast frame rate allows a large sample of independent images to be acquired quickly. In addition, a fast frame rate makes it possible to track the motion of the speckles as it traverses the telescope aperture, assuming frozen flow. With a frame rate of 153 Hz and telescope aperture of 9.25 inches, in principle wind speeds of turbulent layers up to  $\sim 35$  m/s can be measured.

**Exposure Time:** A maximum exposure time of 1 ms was used to avoid smearing of the speckle pattern during the exposure.

### Setup & Alignment

The setup for the SHIMM was the same as described in chapter 4, however there were some additional steps for the FASS.

**Pupil Image:** At the beginning of the night the shape of the pupil image was checked. Accurate collimation of the telescope optics was necessary in order to deliver a circularly symmetric pupil image. This was required to give an accurate mapping of the concentric rings onto the pupil image in the FASS analysis. This was achieved by cross-correlating the pupil image with a predefined software mask of the required dimensions.

**Autoguiding:** Autoguiding was implemented in the same way as described in section 4.2.3. However, to ensure that the FASS was not taking data during autoguiding corrections, messages were sent over an internal network to command the FASS camera to stop acquiring data. Accurate autoguiding was required for the FASS instrument in order to avoid any vignetting of the pupil image within the relay optics. Autoguiding was carried out in the SHIMM instrument as described in section 4.2.3. However, the FASS instrument was also checked for vignetting using the software mask method. Figure 6.23 shows an example of an unvignetted (a) and vignetted (b) pupil image.

### Target Acquisition

The use of the beam splitter and short exposure times meant the light to the FASS instrument was reduced and therefore a bright target star of less than approximately first magnitude was required. This meant that there was not always a visible target at high elevation suitable for the FASS. For this reason a larger telescope aperture of 11 inches is being explored. As long as the pupil image projected onto the EMCCD is the same size in pixels, for the increased telescope aperture, this will counteract the problem. This will also change the sampling of the pupil image and therefore the minimum detectable altitude. However, for an 11 inch telescope

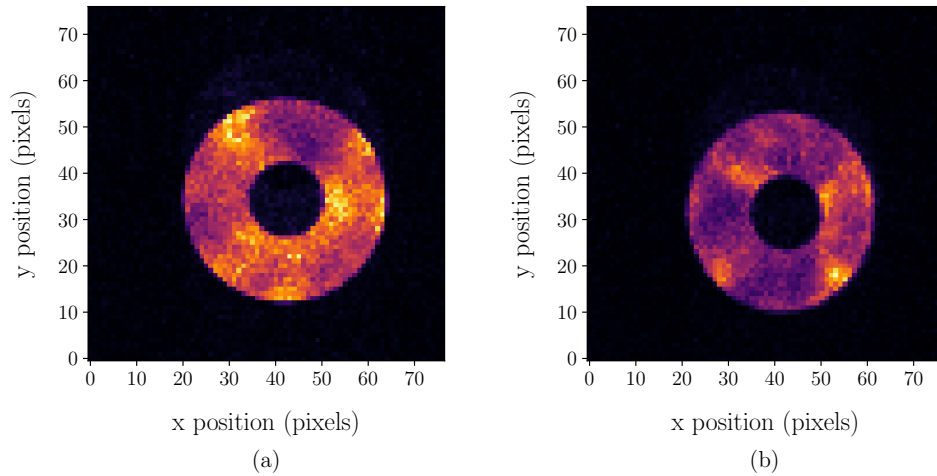


Figure 6.23: Examples of non-vignetted (a) and slightly vignetted (b) pupil images taken by the 9.25 inch FASS.

with a projected pupil image of the same size, the sampling will be 6 mm/pixel, which will not significantly increase the minimum altitude.

Given that the use of a dichroic results in red light passing to the FASS, it is possible to observe a fainter star ( $V > 1.0$ ) with a redder spectrum when first magnitude target stars are not available. Although this means less light is available for the SHIMM, the SHIMM was able to operate with fainter target stars.

### Data Acquisition

In the prototype FASS-SHIMM instrument, analysis of the SHIMM data was carried out in real time as described previously. The FASS data was stored on disc for off-line processing. Real-time analysis for the FASS is envisaged for future operations.

### 6.7.3 On-Sky Results

In this section preliminary results of the FASS mounted on a 9.25 inch telescope will be presented. Observations were made at the Very Large Telescope (VLT) site in Paranal over four nights in April 2016. The data analysis of these observations was conducted by Andrés Guesalaga and presented in Guesalaga et al. (2016).

Figure 6.24 shows examples of turbulence profiles with concurrent measurements from the Stereo-SCIDAR instrument mounted on an AT at of the VLT at Paranal. It can be seen that some profiles are in good agreement with Stereo-SCIDAR. These correlate to times when the zenith angle is similar to that of Stereo-SCIDAR. To reduce this effect, only targets of small zenith angles should be used. By cross-checking stars of second magnitude or brighter, for zenith angles less than  $35^\circ$  between 20:00h to 06:00 UTC over the whole year, it was found that 100% observing time is possible for target stars of brighter than magnitude  $V = 2.05$ . The catalogue of stars used to determine this included stars of a range of spectral types. When the FASS is used in conjunction with the SHIMM, only red light is directed to the FASS. This will reduce the number of target stars that can be observed.

The results presented in figure 6.24 are based on models assuming monochromatic light. However, scintillation is different for different wavelengths. Atmospheric chromatic dispersion results in speckle broadening, such that the flying shadows observed at the pupil plane is stretched into a ‘flying spectra’ (Dravins et al., 1997). When observing at small zenith angles the scintillation index is proportional to  $\lambda^{-7/6}$ . For larger zenith angles, this wavelength dependence prediction becomes weaker. Speckle broadening must be considered in the calculation of the reference functions (Guesalaga et al., 2016). Therefore, a good model of the target star spectrum and the dichroic spectral response is required.

In addition to estimating a turbulence profile, the FASS has the potential to estimate wind profiles. Figure 6.25 shows how the spatio-temporal auto-covariance map of the pupil image can be used to identify the wind velocity of different turbulent

layers. At temporal offsets of  $\delta t = 0$  ms, all turbulent layers are superimposed at the centre of the map. As  $\delta t$  increases these layers move forming individual peaks corresponding to a particular turbulent layer. The width of the peaks indicate the altitude of the layer, with smaller widths corresponding to lower altitudes. Figure 6.25 shows two turbulent layers at wind speeds of 14 m/s travelling in different directions. Further investigation is required to develop an algorithm to measure the movement of these peaks to extract wind velocity information.

#### **6.7.4 Future Work & Conclusions**

The FASS is a new turbulence profiler that employs an EMCCD detector to image the full aperture pupil. By extracting speckle size and intensity information from these images, an optical atmospheric turbulence profile can be estimated. This method rivals the current MASS concept by producing a higher resolution profile. The combined FASS-SHIMM instrument employs the SHIMM to measure the total integrated seeing which is used to estimate the unsensed turbulence close to the ground which the FASS is insensitive to.

Preliminary results were presented showing comparisons between profiles obtained by the FASS and Stereo-SCIDAR. Qualitatively it can be seen that the FASS results are in agreement with Stereo-SCIDAR, this was generally the case for target stars of similar zenith angles.

In 2017/2018 a campaign is scheduled at Paranal observatory to further develop the FASS. The FASS will be mounted onto the C11-SHIMM with the help of a beamsplitter to direct light to the two instruments. This FASS-SHIMM will be operated contemporaneously with the Stereo-SCIDAR. This will allow for comparisons of the FASS-SHIMM with a higher vertical resolution turbulence profiler. Real time analysis of the FASS data and extraction of wind velocity measurements will also be developed.

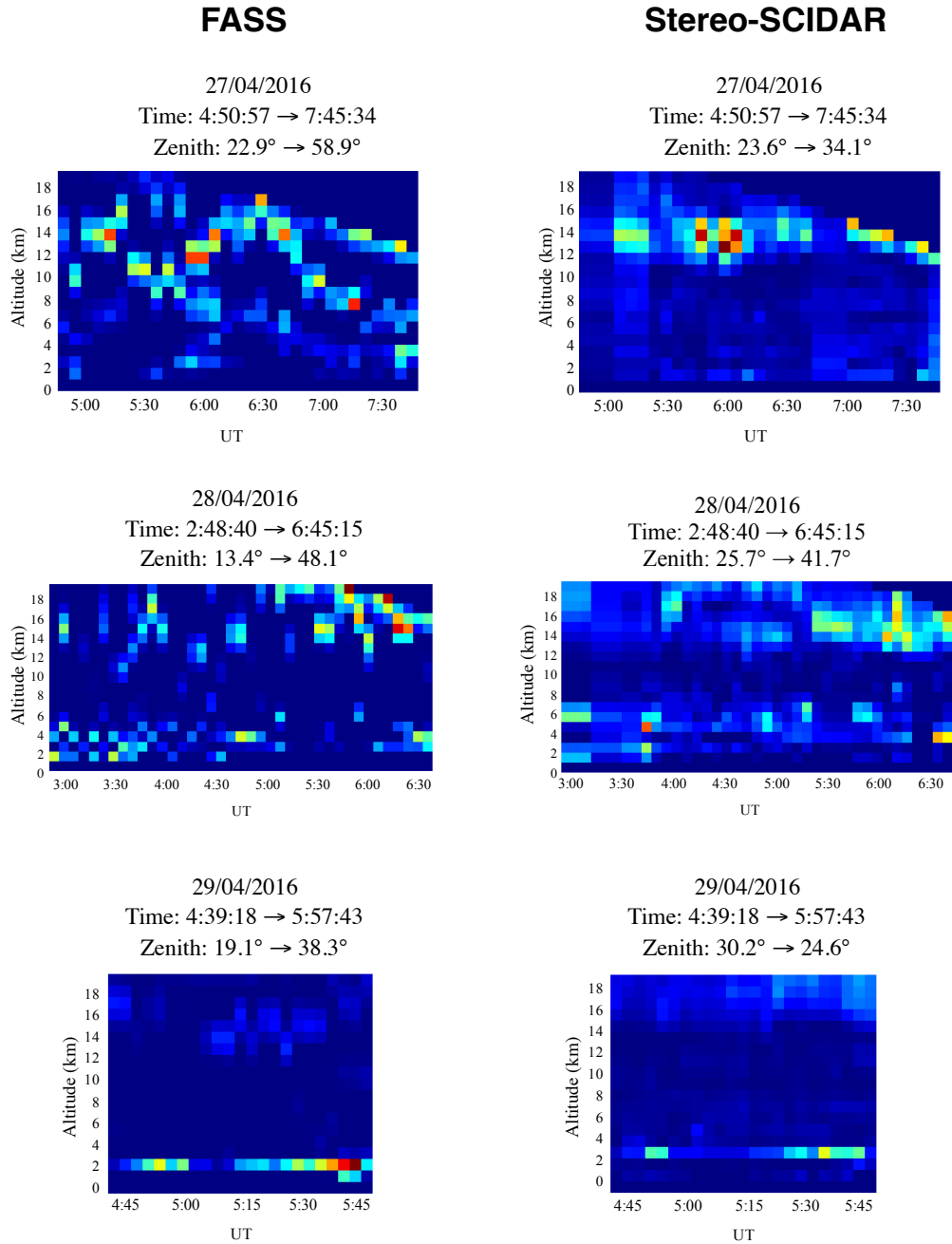


Figure 6.24: Example turbulence profile sequences taken with the FASS mounted on a 9.25 inch telescope and the Stereo-SCIDAR mounted on an AT at Paranal. Profiles were given courtesy of Andrés Guesalaga (Guesalaga et al., 2016).

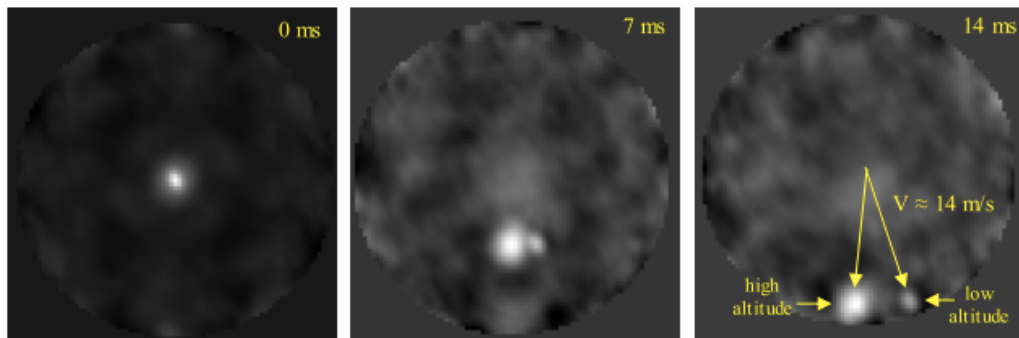


Figure 6.25: An example spatio-temporal auto-covariance map for time steps of 7 ms, from on-sky data taken by the FASS mounted on a 9.25 inch telescope at Paranal. Two peaks corresponding to two turbulent layers become visible each of velocity 14 m/s, each travelling in different directions. The smaller peak corresponds to a lower altitude layer compared to the larger peak (Guesalaga et al., 2016).

---

## Summary of Conclusions

The subject of this thesis was the SHIMM, a low-cost portable seeing monitor. The instrument was built from entirely off-the-shelf components making it easy to duplicate, and therefore ideal for investigating differences in the seeing around a larger observing site. The improvements provided by the SHIMM over the traditional DIMM seeing monitor were presented in each chapter with simulated and on-sky results. The key conclusions of each chapter and the scheduled future investigations are summarised below.

### 7.1 Atmospheric Theory

In chapter 2 the key principles of the origin and effects of atmospheric turbulence was presented. Key parameters ( $C_n^2$ ,  $r_0$ ,  $\tau_0$  and  $\theta_0$ ) used to characterise the atmosphere were introduced and discussed. In addition, the simulation method for modelling optical atmospheric turbulence and its effects were discussed.

### 7.2 Profiler Theory

In chapter 6 four key atmospheric turbulence profilers and seeing monitors, the DIMM, MASS, SLODAR and SCIDAR, were discussed. The basic concept as well

as the pros and cons of each instrument were described. A table was presented summarising the key features of each instrument, as well as the SHIMM and FASS.

### 7.3 Estimating $r_0$

In chapter 4 the optical design configuration, the software for data acquisition and on-sky results of the SHIMM instrument were presented. Simulations showed that this optical configuration could provide an accurate, unbiased measurement of  $r_0$  by employing the SLODAR method of analysis. On-sky results taken at La Palma with two identical SHIMMs demonstrated that the instrument was repeatable, and illustrated that target stars of third magnitude and brighter could be observed for a 9.25 inch telescope aperture. Comparisons were made with Stereo-SCIDAR (mounted on the INT) and the ING RoboDIMM at La Palma. Results indicated a good correlation with Stereo-SCIDAR. However, there was a general underestimation of the seeing measured by the SHIMM compared to both the Stereo-SCIDAR and the RoboDIMM. This is possibly due to an image scale calibration error, which requires further investigation.

### 7.4 Estimating $\tau_0$

In chapter 5 two methods for estimating  $\tau_0$  were presented. It was found, through simulation, that using the power spectrum of the defocus Zernike term, obtained from the centroids of the WFS spots, provided an accurate method for measuring  $\tau_0$ . On-sky results taken by the SHIMM at La Palma were presented. Concurrent measurements of  $\tau_0$  from the SHIMM and another profiling instrument were not possible. However, a histogram of the  $\tau_0$  values obtained was similar to that obtained by Stereo-SCIDAR over a number of different nights.

## 7.5 Estimating a Profile

Optical propagation of strong high altitude turbulence can result in the over-estimation of the value of  $r_0$ . Chapter 6 showed, in simulation, that a reference look-up table based on a turbulence profile of three layers at 0, 5 and 15 km can be used to correct the effects of scintillation on the measurement of  $r_0$ . In addition, it can be used to estimate a fixed three layer turbulence profile. On-sky comparisons with concurrent Stereo-SCIDAR measurements were presented. Results showed that there was agreement with the estimation of the ground turbulence strength, and a lot of scatter in the correlation between the estimated turbulence strength at 5 and 15 km. However, the total integrated seeing showed a good agreement.

## 7.6 Future Work

In chapter 6, the FASS was also presented. The FASS is a new turbulence profiler that employs an EMCCD detector to image the aperture pupil. This instrument is capable of producing a turbulence profile with up to 17 layers when mounted on a 9.25 inch telescope. The FASS-SHIMM is a combination instrument designed to use both the FASS and SHIMM techniques. A campaign is scheduled at the Paranal observatory to further develop and characterise the FASS-SHIMM, in 2017/2018. Concurrent measurements of the FASS-SHIMM and the Stereo-SCIDAR will allow for many comparisons between all three techniques. This will also provide further testing and development of the SHIMM and the features described above.

---

## Noise Analysis of SHIMM

The main instrumental noise contributions that affect centroid measurements are shot noise, sky background and readout noise. Since short exposures are used for observing bright target stars, sky background and readout noise are negligible. Shot noise is statistically independent for different subapertures, therefore an auto-covariance of the centroids would not be biased by shot noise. However, the SHIMM requires subtracting common motion caused by wind shake and telescope guiding errors. Subtracting the mean tip/tilt adds a constant bias to the auto-covariance (Butterley et al., 2006). The effects are described below.

In the case of no mean subtraction each slope (centroid) of each subaperture will have a gradient and noise component

$$S_i = g_i + \epsilon_i, \quad (\text{A.1})$$

$$S_j = g_j + \epsilon_j, \quad (\text{A.2})$$

where  $i$  and  $j$  refer to the subaperture separation in x and y directions respectively.

This expands to

$$\langle S_i S_j \rangle = \langle \epsilon_i \epsilon_j + g_i g_j + g_i \epsilon_j + g_j \epsilon_i \rangle. \quad (\text{A.3})$$

Since cross terms are uncorrelated they can be set to zero such that

$$\langle S_i S_j \rangle = \langle g_i g_j \rangle + \langle \epsilon_i \epsilon_j \rangle. \quad (\text{A.4})$$

This shows that in the case of no mean subtraction the slopes are not biased by shot noise.

When common motion is subtracted the slope will now have an additional mean slope component,

$$S'_i = g_i + \epsilon_i - \sum_{k=1}^n \frac{S_k}{n}, \quad (\text{A.5})$$

$$= g_i + \epsilon_i - \sum_{k=1}^n \frac{g_k + \epsilon_k}{n}, \quad (\text{A.6})$$

$$= g_i + \epsilon_i - \sum_{k=1}^n \frac{g_k}{n} - \sum_{k=1}^n \frac{\epsilon_k}{n}, \quad (\text{A.7})$$

The auto-covariance of the WFS slopes for each separation is given as

$$\begin{aligned} \langle S'_i S'_j \rangle &= \left\langle g_i g_j + g_i \epsilon_j - g_i \sum_{k=1}^n \frac{g_k}{n} - g_i \sum_{k=1}^n \frac{\epsilon_k}{n} \right\rangle + \\ &\quad \left\langle g_j \epsilon_i + \epsilon_i \epsilon_j - \epsilon_i \sum_{k=1}^n \frac{g_k}{n} - \epsilon_i \sum_{k=1}^n \frac{\epsilon_k}{n} \right\rangle + \\ &\quad \left\langle -g_j \sum_{k=1}^n \frac{g_k}{n} - g_j \sum_{k=1}^n \frac{\epsilon_k}{n} + \left( \sum_{k=1}^n \frac{g_k}{n} \right)^2 + \sum_{k=1}^n \frac{g_k}{n} \sum_{k=1}^n \frac{\epsilon_k}{n} \right\rangle + \\ &\quad \left\langle -g_j \sum_{k=1}^n \frac{\epsilon_k}{n} - \epsilon_j \sum_{k=1}^n \frac{\epsilon_k}{n} + \left( \sum_{k=1}^n \frac{\epsilon_k}{n} \right)^2 + \sum_{k=1}^n \frac{g_k}{n} \sum_{k=1}^n \frac{\epsilon_k}{n} \right\rangle. \end{aligned} \quad (\text{A.8})$$

As all cross terms are uncorrelated they can be set to zero giving

$$\begin{aligned} \langle S'_i S'_j \rangle &= \left\langle g_i g_j - g_i \sum_{k=1}^n \frac{g_k}{n} + \epsilon_i \epsilon_j - \epsilon_i \sum_{k=1}^n \frac{\epsilon_k}{n} \right\rangle + \\ &\quad \left\langle -g_j \sum_{k=1}^n \frac{g_k}{n} + \left( \sum_{k=1}^n \frac{g_k}{n} \right)^2 - \epsilon_j \sum_{k=1}^n \frac{\epsilon_k}{n} + \left( \sum_{k=1}^n \frac{\epsilon_k}{n} \right)^2 \right\rangle. \end{aligned} \quad (\text{A.9})$$

The noise terms can be separated and expressed as

$$\begin{aligned} \langle \epsilon'_i \epsilon'_j \rangle &= \left\langle \epsilon_i \epsilon_j - \epsilon_i \sum_{k=1}^n \frac{\epsilon_k}{n} - \epsilon_j \sum_{k=1}^n \frac{\epsilon_k}{n} + \left( \sum_{k=1}^n \frac{\epsilon_k}{n} \right)^2 \right\rangle, \\ &= \left\langle \epsilon_i \epsilon_j - 2 \frac{\epsilon_i^2}{n} + \left( \sum_{k=1}^n \frac{\epsilon_k}{n} \right)^2 \right\rangle, \\ &= \langle \epsilon_i \epsilon_j \rangle - \frac{1}{n} \langle \epsilon_i^2 \rangle, \end{aligned} \quad (\text{A.10})$$

$$\langle \epsilon'_i \epsilon'_j \rangle = \begin{cases} \left(1 - \frac{1}{n}\right) \langle \epsilon_i^2 \rangle & \text{if } i = j \\ -\frac{1}{n} \langle \epsilon_i^2 \rangle & \text{if } i \neq j \end{cases} \quad (\text{A.11})$$

---

## Bibliography

- Aristidi, E., Fantei-Caujolle, Y., Ziad, A., Dimur, C., Chabé, J., and Roland, B. A new generalized differential image motion monitor. volume 9145 of *Proc. SPIE*, pages 91453G–91453G–9, 2014. doi: 10.1117/12.2056201. URL <http://dx.doi.org/10.1117/12.2056201>.
- Avila, R., Avilés, J. L., Wilson, R. W., Chun, M., Butterley, T., and Carrasco, E. LOLAS: An optical turbulence profiler in the atmospheric boundary layer with extreme altitude resolution. *MNRAS*, 387(4):1511–1516, 2008. ISSN 00358711. doi: 10.1111/j.1365-2966.2008.13386.x.
- Baker, K. L. and Moallem, M. M. Iteratively weighted centroiding for shack-hartmann wave-front sensors. *Opt. Express*, 15(8):5147–5159, Apr 2007. doi: 10.1364/OE.15.005147. URL <http://www.opticsexpress.org/abstract.cfm?URI=oe-15-8-5147>.
- Bally, J., Theil, D., Billawalla, Y., Potter, D., Loewenstein, R., Mrozek, F., and Lloyd, J. P. A Hartmann Differential Image Motion Monitor (H-DIMM) for Atmospheric Turbulence Characterisation. *PASA*, 13:22–27, 1996.
- Barry, R. G. and Chorley, R. J. *Atmosphere, Weather and Climate*. Routledge, London, 1968.

- Basden, A. G. Analysis of electron multiplying charge coupled device and scientific cmos readout noise models for shack–hartmann wavefront sensor accuracy. *Journal of Astronomical Telescopes, Instruments, and Systems*, 1:1 – 1 – 10, 2015. doi: 10.1117/1.JATIS.1.3.039002. URL <http://dx.doi.org/10.1117/1.JATIS.1.3.039002>.
- Basden, A. G., Myers, R. M., and Gendron, E. Wavefront sensing with a brightest pixel selection algorithm. *Monthly Notices of the Royal Astronomical Society*, 419(2):1628–1636, 2012. doi: 10.1111/j.1365-2966.2011.19825.x. URL <http://dx.doi.org/10.1111/j.1365-2966.2011.19825.x>.
- Basden, A., Butterley, T., Myers, R., and Wilson, R. Durham extremely large telescope adaptive optics simulation platform. *Appl. Opt.*, 46(7):1089–1098, Mar 2007. doi: 10.1364/AO.46.001089. URL <http://ao.osa.org/abstract.cfm?URI=ao-46-7-1089>.
- Buscher, D. F. *Practical Optical Interferometry*. Cambridge University Press, Cambridge, 2015.
- Butterley, T., Wilson, R. W., and Sarazin, M. Determination of the Profile of Atmospheric Optical Turbulence Strength from SLODAR Data. *MNRAS*, 369: 835–845, 2006.
- Conan, J.-M., Rousset, G., and Madec, P.-Y. Wave-front temporal spectra in high-resolution imaging through turbulence. *J. Opt. Soc. Am. A*, 12(7):1559–1570, Jul 1995. doi: 10.1364/JOSAA.12.001559. URL <http://josaa.osa.org/abstract.cfm?URI=josaa-12-7-1559>.
- Dravins, D., Lindegren, L., and Mezey, E. Atmospheric Intensity Scintillation of Stars. II. Dependence on Optical Wavelength. *PASP*, 109:725–737, 1997.
- Ellerbroek, B. L. First-order performance evaluation of adaptive-optics systems for atmospheric-turbulence compensation in extended-field-of-view astronomical telescopes. *JOSA A*, 11(2):783–805, 1994.

- Fohring, D. *The Effect of Scintillation on Ground-Based Exoplanet Transit Photometry*. Phd thesis, University of Durham, 2014.
- Fried, D. L. Statistics of a geometric representation of wavefront distortion. *J. Opt. Soc. Am.*, 55(11):1427–1435, Nov 1965. doi: 10.1364/JOSA.55.001427. URL <http://www.osapublishing.org/abstract.cfm?URI=josa-55-11-1427>.
- Goodman, J. W. *Introduction to Fourier Optics*. McGraw-Hill Book Company, 1968.
- Goodwin, M., Jenkins, C., and Lambert, A. Generalized slope detection and ranging turbulence profiling at las campanas observatory. *Monthly Notices of the Royal Astronomical Society*, 461(2):1701–1717, 2016. doi: 10.1093/mnras/stw1417. URL <http://dx.doi.org/10.1093/mnras/stw1417>.
- Goodwin, M., Jenkins, C., and Lambert, A. Improved detection of atmospheric turbulence with slodar. *Opt. Express*, 15(22):14844–14860, Oct 2007. doi: 10.1364/OE.15.014844. URL <http://www.opticsexpress.org/abstract.cfm?URI=oe-15-22-14844>.
- Guesalaga, A., Perera, S., Osborn, J., Sarazin, M., Neichel, B., and Wilson, R. W. FASS: The Full Aperture Seeing Sensor. In *Astronomical Telescopes and Instrumentation*, volume 9909 of *Proc. SPIE*, 2016. doi: 10.1117/12.2232012. URL <http://dx.doi.org/10.1117/12.2232012>.
- Hardy, J. W. *Adaptive Optics for Astronomical Telescopes*. Oxford University Press, New York, 1998.
- Higgins, C. W., Froidevaux, M., Simeonov, V., Vercauteren, N., Barry, C., and Parlange, M. B. The effect of scale on the applicability of taylor’s frozen turbulence hypothesis in the atmospheric boundary layer. *Boundary-layer meteorology*, 143(2):379–391, 2012.

- Hogge, C. B. and Butts, R. R. Frequency spectra for the geometric representation of wavefront distortions due to atmospheric turbulence. *IEEE Trans. Antennas Propag.*, 24:144–154, 1976.
- Hunter, J. D. Matplotlib: A 2d graphics environment. *Computing in Science & Engineering*, 9(3):90–95, 2007. doi: 10.1109/MCSE.2007.55. URL <http://aip.scitation.org/doi/abs/10.1109/MCSE.2007.55>.
- Kellerer, A. and Tokovinin, A. Atmospheric Coherence Times in Interferometry: Definition and Measurement. *A&A*, 461:775–781, 2007.
- Kornilov, V., Tokovinin, A. A., Vozyakova, O., Zaitsev, A., Shatsky, N., Potanin, S. F., and Sarazin, M. S. MASS: A Monitor of the Vertical Turbulence Distribution. *Proc. SPIE*, 4839:837–845, 2003. doi: 10.1117/12.457982. URL <http://dx.doi.org/10.1117/12.457982>.
- Labeyrie, A., Lipson, S. G., and Nisenson, P. *An Introduction to Optical Stellar Interferometry*. Cambridge University Press, Cambridge, 2006.
- NASA. Wikipedia: Electromagnetic Radiation, 2008. URL [https://commons.wikimedia.org/wiki/File:Atmospheric\\_electromagnetic\\_opacity.svg](https://commons.wikimedia.org/wiki/File:Atmospheric_electromagnetic_opacity.svg). visited on 2017-07-24.
- Nightingale, N. S. and Buscher, D. F. Interferometric seeing measurements at the La Palma Observatory. *MNRAS*, 251:155–166, 1991.
- Noll, R. J. Zernike polynomials and atmospheric turbulence. *J. Opt. Soc. Am.*, 66(3):207–211, Mar 1976. doi: 10.1364/JOSA.66.000207. URL <http://www.osapublishing.org/abstract.cfm?URI=josa-66-3-207>.
- O’Donovan, B., Young, J. S., Warner, P. J., Buscher, D. F., Wilson, D. M. A., Boysen, R. C., Seneta, E. B., and Keen, J. DIMMWIT: comparing atmospheric seeing values measured by a differential image motion monitor, which is transportable, and COAST. volume 4838, pages 794–802, 2003. doi: 10.1117/12.459761. URL <http://dx.doi.org/10.1117/12.459761>.

- O’Grady, A. A comparison of EMCCD, CCD and emerging technologies optimized for low-light spectroscopy applications. volume 6093, pages 6093 – 6093 – 9, 2006. doi: 10.1117/12.644752. URL <http://dx.doi.org/10.1117/12.644752>.
- O’Mahony, N. RoboDIMM — The ING’s New Seeing Monitor. *The ING Newsletter*, 7:22–24, 2003a.
- O’Mahony, N. Isaac Newton Group of Telescopes: RoboDIMM Data Access [Online], 2003b. URL <http://catserver.ing.iac.es/robodimm/>. visited on 2017-08-01.
- Osborn, J. *Profiling the Turbulent Atmosphere and Novel Correction Techniques for Imaging and Photometry in Astronomy*. Phd thesis, University of Durham, 2010.
- Osborn, J., Wilson, R. W., Butterley, T., Sheperd, H., and Sarazin, M. Profiling the surface layer of optical turbulence with SLODAR. *MNRAS*, 406:1405–1408, 2010.
- Osborn, J., Wilson, R. W., Dhillon, V. S., Avila, R., and Love, G. D. Conjugate-plane photometry: reducing scintillation in ground-based photometry. *MNRAS*, 411:1223–1230, 2011.
- Osborn, J., Föhrling, D., Dhillon, V. S., and Wilson, R. W. Atmospheric Scintillation in Astronomical Photometry. *MNRAS*, 452:1707–1716, 2015.
- Platt, B. C. and Shack, R. History and Principles of Shack-Hartmann Wavefront Sensing. *J Refract Surg.*, 17:573–577, 2003.
- Prieur, J.-L., Daigne, G., and Avila, R. Scidar measurements at pic du midi\*. *A&A*, 371(1):366–377, 2001. doi: 10.1051/0004-6361:20010279. URL <https://doi.org/10.1051/0004-6361:20010279>.
- Robert, C., Vérdenne, N., Michau, V., and Conan, J.-M. Cn2 profile from shack-hartmann data: First steps for co-slidar data processing. In Masciadri, E. and

- Sarazin, M., editors, *Optical Trubulence Astronomy Meets Meterorology*, Proc. Optical Tubulence Characterization for Astronomical Applications, pages 74–81, 2008.
- Robert, C., Voyez, J., Védrenne, N., and Mugnier, L. Cn2 profile from Shack-Hartmann data with CO-SLIDAR data processing. *Observatory*, 2011. URL <http://arxiv.org/abs/1101.3924>.
- Robitaille, T. P., Tollerud, E. J., Greenfield, P., Droettboom, M., Bray, E., Aldcroft, T., Davis, M., Ginsburg, A., Price-Whelan, A. M., Kerzendorf, W. E., Conley, A., Crighton, N., Barbary, K., Muna, D., Ferguson, H., Grollier, F., Parikh, M. M., Nair, P. H., Günther, H. M., Deil, C., Woillez, J., Conseil, S., Kramer, R., Turner, J. E. H., Singer, L., Fox, R., Weaver, B. A., Zabalza, V., Edwards, Z. I., Azalee Bostroem, K., Burke, D. J., Casey, A. R., Crawford, S. M., Dencheva, N., Ely, J., Jenness, T., Labrie, K., Lim, P. L., Pierfederici, F., Pontzen, A., Ptak, A., Refsdal, B., Servillat, M., and Streicher, O. Astropy: A community Python package for astronomy. *Astronomy & Astrophysics*, 558:A33, 2013. ISSN 0004-6361. doi: 10.1051/0004-6361/201322068. URL <http://adsabs.harvard.edu/abs/2013A%7B%7D26A...558A..33A>.
- Roddier, F. *The Effects of Atmospheric Turbulence in Optical Astronomy*. Progress in optics. North-Holland Publishing Company, 1981. URL [https://books.google.co.uk/books?id=a\\_BKGwAACAAJ](https://books.google.co.uk/books?id=a_BKGwAACAAJ).
- Roddier, F. *Adaptive Optics in Astronomy*. Cambridge University Press, 1999. doi: 10.1017/CBO9780511525179.
- Roddier, F., Northcott, M. J., Graves, J. E., , and McKenna, D. L. One-dimensional sepectra of turbulence-induced Zernike aberrations: time-delay and isoplanicity error in partial adaptive compensation. *J. Opt. Soc. Am. A*, 10:957–965, 1993.
- Russell, R. Windows to the Universe: The Stratosphere [Online], 2009. URL

- <https://www.windows2universe.org/earth/Atmosphere/stratosphere.html>. visited on 2017-07-24.
- Saint-Jacques, D. *Astronomical Seeing in Space and Time*. Phd thesis, University of Cambridge, 1998.
- Sarazin, M. and Roddier, F. The ESO Differential Image Motion Monitor. *Astron. & Astrop.*, 227:294–300, 1989.
- Shepherd, H. W., Osborn, J., Wilson, R. W., Butterley, T., Avila, R., Dhillon, V. S., and Morris, T. J. Stereo-SCIDAR: Optical Turbulence Profiling with High Sensitivity Using a Modified SCIDAR Instrument. *MNRAS*, 437:3568–3577, 2013.
- Sorensen, P. and Mendez, J. Isaac Newton Group of Telescopes: Weather and Observing Conditions [Online], 2002. URL <http://catserver.ing.iac.es/weather/archive/index.php>. visited on 2017-08-01.
- Tokovinin, A. From differential image motion to seeing. *PASP*, 114:1156–1166, 2002.
- Tokovinin, A. Turbulence Profiles From the Scintillation of Stars, Planets, and Moon. *Proc. RevMexAA*, 31:61–70, 2007.
- Tokovinin, A. and Kornilov, V. Accurate Seeing Measurements with MASS and DIMM. *MNRAS*, 381:1179–1189, 2007.
- Tokovinin, A., Kellerer, A., and Foresto, V. C. D. FADE, an instrument to measure the atmospheric coherence time. *A&A*, 477:671–680, 2008.
- Townson, M. J., Reeves, A. P., Osborn, J., Bitenc, U., Laidlaw, D. J., and Farley, O. AOTools. *In Prep*, 2017.
- van der Walt, S., Colbert, S. C., and Varoquaux, G. The numpy array: A structure for efficient numerical computation. *Computing in Science & Engineering*, 13(2):

- 22–30, 2011. doi: 10.1109/MCSE.2011.37. URL <http://aip.scitation.org/doi/abs/10.1109/MCSE.2011.37>.
- Vernin, J. Mechanism of formation of optical turbulence. volume 266 of *ASP Conference Series*, pages 2–17, 2002.
- Vernin, J. and Roddier, F. Experimental determination of two-dimensional spatiotemporal power spectra of stellar light scintillation evidence for a multilayer structure of the air turbulence in the upper troposphere. *J. Opt. Soc. Am.*, 63(3):270–273, Mar 1973. doi: 10.1364/JOSA.63.000270. URL <http://www.osapublishing.org/abstract.cfm?URI=josa-63-3-270>.
- Vidal, F., Gendron, E., and Rousset, G. Tomography approach for multi-object adaptive optics. *J. Opt. Soc. Am. A*, 27(11):A253–A264, Nov 2010. doi: 10.1364/JOSAA.27.00A253. URL <http://josaa.osa.org/abstract.cfm?URI=josaa-27-11-A253>.
- Wilson, R. W. SLODAR: measuring optical turbulence altitude with a Shack-Hartmann wavefront sensor. *MNRAS*, 337:103–108, 2002.
- Wilson, R. W., O’Mahony, N., Packham, C., and Azzaro, M. The Seeing at the William Herschel Telescope. *MNRAS*, 309:379–389, 1999.
- Ziad, A., Conan, R., Tokovinin, A., Martin, F., and Borgnino, J. From the grating scale monitor to the generalized seeing monitor. *Appl. Opt.*, 39(30):5415–5425, Oct 2000. doi: 10.1364/AO.39.005415. URL <http://ao.osa.org/abstract.cfm?URI=ao-39-30-5415>.

## Colophon

This thesis was typeset with L<sup>A</sup>T<sub>E</sub>X 2<sub>ε</sub>. It was created using the *memoir* package, maintained by Lars Madsen, with the *madsen* chapter style. The font used is Latin Modern, derived from fonts designed by Donald E. Kunith.